

DISSERTATION

DEVELOPMENT OF A VERY COMPACT HIGH REPETITION RATE SOFT
X-RAY LASER

Submitted by

Federico Juan Antonio Furch

Department of Physics

In partial fulfillment of the requirements

for the degree of Doctor of Philosophy

Colorado State University

Fort Collins, Colorado

Summer 2010

UMI Number: 3534989

All rights reserved

INFORMATION TO ALL USERS

The quality of this reproduction is dependent upon the quality of the copy submitted.

In the unlikely event that the author did not send a complete manuscript and there are missing pages, these will be noted. Also, if material had to be removed, a note will indicate the deletion.

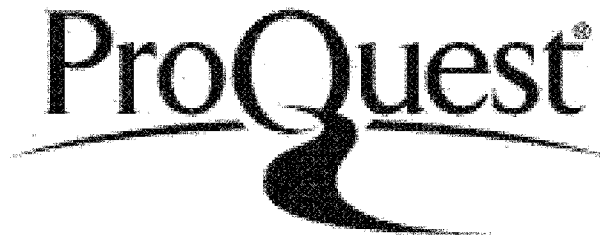


UMI 3534989

Published by ProQuest LLC 2013. Copyright in the Dissertation held by the Author.

Microform Edition © ProQuest LLC.

All rights reserved. This work is protected against unauthorized copying under Title 17, United States Code.



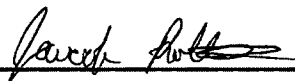
ProQuest LLC
789 East Eisenhower Parkway
P.O. Box 1346
Ann Arbor, MI 48106-1346

COLORADO STATE UNIVERSITY

June 17 2010

WE HEREBY RECOMMEND THAT THE DISSERTATION PREPARED UNDER OUR SUPERVISION BY FEDERICO JUAN ANTONIO FURCH ENTITLED "DEVELOPMENT OF A VERY COMPACT HIGH REPETITION RATE SOFT X-RAY LASER" BE ACCEPTED AS FULFILLING IN PART REQUIREMENTS FOR THE DEGREE OF DOCTOR OF PHILOSOPHY.

Committee on Graduate Work



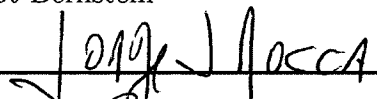
Jacob Roberts



Siu Au Lee



Elliot Bernstein



Adviser: Jorge J. Rocca



Co-Adviser: Mario Marconi



Department Chair: Hans D. Hochheimer

ABSTRACT OF DISSERTATION

DEVELOPMENT OF A VERY COMPACT HIGH REPETITION RATE SOFT X-RAY LASER

Over the last 25 years, the field of soft x-ray lasers has evolved from facility size devices delivering a few shots per day, to table-top lasers operating at several shots per second. In these lasers the gain medium is a highly ionized, hot and dense plasma created by a sequence of short, high energy pulses from an optical laser. Current table-top soft x-ray lasers have enabled numerous applications such as nano-scale imaging, nano-fabrication and dense plasma diagnosis among others. However these lasers are still limited in repetition rate, and therefore average power, owing to thermal effects originated in the flash lamp pumped amplifiers of the optical driver laser.

Direct diode-pumping of the driver laser opens the possibility of developing more compact, higher repetition rate optical laser systems to pump soft x-ray lasers. Directly pumping small quantum defect materials such as Yb:YAG with a narrow bandwidth source of the optimum wavelength allows to significantly increase the efficiency and then reduce the thermal load in the gain materials. In

addition, cryogenic cooling of the laser materials significantly improves their thermal performance. This approach will allow for soft x-ray laser operation at much higher repetition rates.

In this work I present the results of the demonstration of an all diode-pumped soft x-ray laser that constitutes the first of a new generation of more compact, higher repetition rate soft x-ray lasers in the spectral region between 10 and 20 nm. To pump these lasers we developed an all diode-pumped chirped pulse amplification laser system based on cryogenically cooled Yb:YAG. This optical laser generates pulses of 1 J of energy in 8.5 ps pulses at 10 Hz, the highest energy per pulse for sub-10 ps pulses from a diode-pumped system at the present time. This soft x-ray laser has the potential to operate at unsurpassed repetition rates in a reduced footprint.

Federico Juan Antonio Furch
Department of Physics
Colorado State University
Fort Collins, CO 80523
Summer 2010

ACKNOWLEDGEMENTS

I would like to thank the committee members, Prof. Elliot Bernstein, Prof. Siu Au Lee, Prof. Jacob Roberts and in particular to my advisors Prof. Jorge Rocca and Prof. Mario Marconi for their guidance during my time as a graduate student. I would also like to thank Prof. Carmen Menoni.

Thanks to all the team at the ERC. I am glad to say that the list of people to thank is really long, so I prefer to express my gratitude to all of them, for their collaboration, support and friendship.

Special thanks to the rest of the crew in the diode-pumped project, my co-workers and friends: Brendan Reagan, Brad Luther and Alden Curtis.

I also want to thank my friends outside the ERC for six years of support and good times.

Finally, I want to thank my family, in particular to my parents, my sister and Nayra... For everything.

TABLE OF CONTENTS

1	Introduction	1
1.1	Basic physical concepts involved in soft x-ray lasers	6
1.1.1	Equations governing the plasma behavior	8
1.1.2	Transitions, population levels and gain	13
1.1.3	ASE lasers and refraction effects	17
1.2	Population inversion mechanism: Electron impact excitation	21
1.2.1	Ne-like collisional lasers pumped by a single, long laser pulse	22
1.2.2	Extension to the Ni-like isoelectronic series	27
1.2.3	Pre-pulse technique	30
1.2.4	Transient collisional excitation	33
1.2.5	Grazing incidence pumping: Table-top soft x-ray lasers	36
1.3	State of the art of driver lasers for pumping soft x-ray lasers	42
1.3.1	Chirped pulse amplification systems	43
1.3.2	Amplifiers pumped by flash lamps	47
1.3.3	The promise of laser diode pumping	50
2	Description and performance of the CPA laser system	71
2.1	Diode-pumped chirped pulse amplification systems	72

2.1.1	Advantages of direct diode-pumping	73
2.1.2	Yb-doped gain materials	75
2.1.3	General characteristics of Yb:YAG	77
2.1.4	Cryogenically cooled Yb:YAG	80
2.1.5	State of the art on Yb:YAG lasers	88
2.2	Description of the all diode-pumped CPA laser system	93
2.2.1	Oscillator	94
2.2.2	Grating stretchers	98
2.2.3	First amplification stage: Regenerative amplifier	104
2.2.4	Second amplification stage: Multipass amplifier	110
2.2.5	Compressor chamber	116
2.3	CPA laser system output characteristics	119
3	Demonstration of an all diode-pumped soft x-ray laser	140
3.1	Set up for soft x-ray laser: Focusing chamber and target chamber .	141
3.2	Simulations	147
3.3	Demonstration of soft x-ray amplification with an all diode-pumped system	153
4	Photoelectron spectroscopy for dielectric thin film characteriza- tion: a proposed experiment	159
4.1	Motivations for photoelectron spectroscopy	160

4.2	Experimental considerations	164
4.3	Proposed experiment	171
5	Summary	181

Chapter 1

INTRODUCTION

Extreme Ultra Violet (EUV) and soft x-ray radiation occupy the electromagnetic spectrum range between the far ultraviolet and the hard x-rays. In this spectral region, the radiation exhibits a typical penetration depth of less than 1 μm and the reflectivity of optical surfaces at normal incidence is very small. On top of that, the wavelength is still too large to use Bragg reflection, as it is possible with hard x-rays. Moreover, the physical conditions for the generation of coherent EUV and soft x-rays are extreme. As a direct consequence of these characteristics, science and technology related to EUV and soft x-rays are still in an early development stage compared to mature technologies in other ranges of the electromagnetic spectrum such as the visible, infrared or radio frequencies, for instance.

There is no complete agreement in which are the limits of EUV and soft x-rays. In ref. [1] Attwood calls EUV to photon energies between 30 eV and 250 eV (40 nm to 5 nm) and soft x-rays to photon energies ranging from 250 to several keV (5 nm to approximately 0.3 nm). In fig. 1.1 this region of the electromagnetic spectrum is illustrated as it appears in ref. [1]. According to Elton in ref. [2], EUV

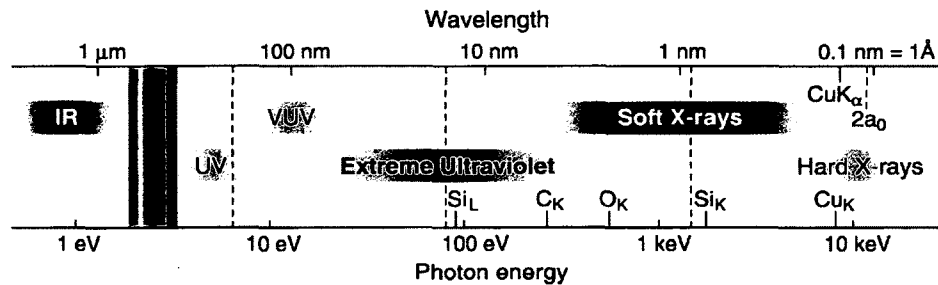


Figure 1.1: EUV and soft x-rays in the electromagnetic spectrum (Ref. [1])

radiation extends from 100 nm to 30 nm and soft x-rays from 30 nm to 0.2 nm. The latter is the convention that will be followed in the rest of this work.

As pointed out by Attwood, the existence of numerous atomic resonances in this region provides unique mechanisms for basic research in surface science, chemistry and physics. Moreover, the short wavelengths characteristic of EUV and soft x-rays allow for imaging of small structures with nanometer resolution, or printing very small features. This in particular has brought the attention of the semiconductor industry towards the field. Advances in sources, diffractive optics, multilayer coating of Mo/Si pairs providing good reflectivity around 13.5 nm, nano-fabrication techniques, high resolution inspection tools and other enabling technologies, will make possible, in the near future, the fabrication of computer microprocessors with significantly smaller features and consequently faster performance than what the current technology can provide.

Coherent soft x-ray sources can be divided into two categories: facility size sources and compact sources. Synchrotrons and Free Electron Lasers (FEL) constitute sources of soft x-ray radiation that occupy entire facilities and are of course very expensive to operate. Synchrotron radiation is generated when ultra relativistic charged particles move in a circular path. Typically electrons with energies in the GeV range are forced to move in a storage ring, and the emission of radiation is enhanced by the introduction of undulators or wigglers. The radiation emitted is not coherent. To obtain coherent radiation from a synchrotron the broad spectrum

emitted has to be filtered. In this indirect way the source is highly tunable. FELs use a linear particle accelerator to accelerate an electron beam that afterwards is made to oscillate as it passes through a wiggler. The photons emitted while the electrons oscillate between the magnets of the wiggler are in phase with the oscillating electrons and the emitted radiation is coherent. FELs can be widely tuned. Synchrotrons and FELs are excellent sources of soft x-ray radiation, but they are expensive and not very accessible.

High harmonic generation from optical laser pulses and soft x-ray plasma-based lasers are two compact sources of coherent radiation that occupy at the most, a few optical tables and therefore provide, in many cases, a laboratory size alternative to synchrotrons and FELs. High harmonic generation is a nonlinear interaction between an intense laser field and atoms or molecules that generates radiation with frequencies that are multiple integers of the frequency of the laser field driving the process. It can provide coherent, tunable, ultrafast pulses of soft x-ray radiation in a table-top device. Another table-top approach, the one in which this work will concentrate on, is plasma based soft x-ray lasers, and in particular, laser pumped soft x-ray lasers in which the plasma is produced by high power optical laser pulses. Although the first plasma based soft x-ray laser occupied an entire facility, the field has evolved towards table-top devices. Soft x-ray lasers are significantly more monochromatic than radiation emitted by high harmonic generation, with orders of magnitude higher energy per pulse but at a

lower repetition rate. The emission wavelength of soft x-ray lasers is fixed by the material from which the plasma is created.

All the mentioned sources have been extensively used already in numerous applications. Some examples are nanoscale imaging [3–8], nano-patterning [9–12], chemical studies enabled by single photon ionization [13–16], surface science [17–19], dense plasma diagnosis [20–23], and others. In particular, the table-top devices, enabling laboratory size experiments, are contributing towards a better understanding of the physics underlying these disciplines and keep enabling new technological applications. However present table-top sources are limited in average power. In the case of soft x-ray lasers, a limitation in the repetition rate of the sources imposes a limitation to the average power. The intention of this work is to develop a novel, improved source of coherent soft x-ray radiation that can provide increased average power in a more compact footprint. The advantages of such a device are immediate since many applications would benefit from the increased average power. Nevertheless, the full potential of this new laser may still be unforeseen and the number of applications exploiting the advantages of the source may very well grow in the future with new advances in the field of soft x-ray radiation.

The rest of this chapter is devoted to plasma based soft x-ray lasers. First a general introduction to the physical concepts involved is given. Then, different ways of producing a population inversion are described, with special attention to

electron impact excitation. Later, the historical evolution of collisional soft x-ray lasers is briefly described and finally, the state of the art of optical laser systems that serve as drivers for soft x-ray lasers is addressed with special attention to the current limitations of the sources and how these limitations could be overcome.

1.1 Basic physical concepts involved in soft x-ray lasers

Since the invention of the laser in the early 1960s [24] there has been interest in extending its range of operation towards other regions of the electromagnetic spectrum. It was soon recognized that extending lasers towards shorter wavelengths presented many challenges, in particular to soft x-ray wavelengths: an unfavorable scaling of gain with wavelength and a short gain lifetime were predicted, no cavity reflectors were available, and it was expected that extremely large pumping powers would be required [2]. Moreover, it was also understood that for this range of wavelengths a plasma would be the gain material.

Visible and infrared lasers operate based on the creation of a population inversion between two energy levels of atomic or molecular transitions. To extrapolate this to soft x-ray wavelengths, the energy difference between the levels in the transition has to be much larger, and it turns out that highly ionized atoms present the required energy level structure. This can be illustrated with the simple and well known energy levels of the hydrogen atom, or more generally, an ion with a

single bound electron. In this case, the energy is approximately proportional to the square of the nuclear charge:

$$E_n \simeq -13.6eV \frac{Z^2}{n^2} \quad (1.1)$$

From this expression it is clear that the energy difference between two levels with different principal quantum number n grows quadratically with the nuclear charge Z . The scaling with Z is slower for systems with more than one electron because the inner electrons act as a shield between the nucleus and the outermost electron. Nevertheless, it is still clear that multiply ionized atoms can provide the required transitions for soft x-rays wavelengths.

For soft x-ray wavelengths, an energy difference of several tens to hundreds of eV is needed, and the energy required to excite an ion from its ground state to an excited state is in the order of several hundreds of eV to some keV. A highly ionized plasma must be created, containing ions whose energy level structure presents transitions with the mentioned photon energy. On top of that, if the excitation from the ground state to the excited levels is to be by collisions with free electrons in the plasma, the mean value of the kinetic energy of the electrons, and therefore the electron temperature has to be high enough such that a considerable number of electrons within the velocity distribution function reach an energy equal or higher to the energy difference between the excited level to be populated and the ground state. This suggests the need for a hot plasma as gain medium. In addition, for

the emitted radiation to be intense, it must come from a large number of emitters in a small volume. Therefore, soft x-ray wavelengths require, in principle, a hot and dense plasma.

1.1.1 Equations governing the plasma behavior

Since plasmas are the gain media for the wavelength range of interest, it seems reasonable to describe the basic concepts involved in plasma physics. A plasma may be described basically as a fluid of charged particles, with different particle species: ions with different charges (atoms in different stages of ionization) and free electrons. This collective behavior description avoids the difficulty of describing each particle in the system. The charged particles in this fluid constitute a source for electromagnetic fields that must be taken into account in the description. Therefore, the most general time evolution description of the fluid is given by a set of hydrodynamic equations for charged particles in which the equations describing the time evolution of the fluid are coupled to Maxwell's equations through the electromagnetic sources, since the charged particles moving in the plasma give rise to electromagnetic fields. The collective behavior description is valid for length scales bigger than the Debye length λ_D :

$$\lambda_D = \left(\frac{\epsilon_0 k T_e}{e^2 n_e} \right)^{1/2} \quad (1.2)$$

where ϵ_0 is the permittivity of vacuum, k is the Boltzmann constant, T_e is the electron temperature, e is the electron charge and n_e is the electron density. This is a characteristic length of the plasma that indicates the distance beyond which the influence of a charged particle will be screened by the presence of a cloud of other charged particles. In particular, it indicates that the fluid-like description is valid over length scales bigger than λ_D .

In laser created plasmas like the ones of interest for this work, the charge density can be considered equal to zero because the plasma is quasi-neutral. Likewise, the net current density can be neglected and the self generated electromagnetic field eliminated from the hydrodynamic equations. In this way only the hydrodynamic equations have to be solved [25]. The time evolution of the plasma is described then by three conservation equations (conservation of mass, momentum and energy) and an equation of state. Using a convective or total derivative the conservation of mass can be written as

$$\frac{d\rho_j}{dt} + \rho_j(\nabla \cdot \mathbf{v}_j) = m_j \dot{n}_j \quad (1.3)$$

where ρ_j is the mass density of species j , \mathbf{v}_j its field of velocities, and $m_j \dot{n}_j$ indicates a rate of creation/destruction of mass for that species. Let's recall that this is possible since the number of free electrons and different ions is changing constantly owing to ionization and recombination in the plasma. A global continuity equation can be written if we assume that there is a field of velocities (\mathbf{v}) that describes

the motion of the whole plasma, this is, ions and free electrons drift with the same velocity. This is not contradictory with the existence of more than one temperature in the plasma, since the temperature is given by the random motion. The global continuity equation is then:

$$\frac{d\rho}{dt} + \rho(\nabla \cdot \mathbf{v}) = 0 \quad (1.4)$$

The equation doesn't have a creation/destruction term. This reflects the fact that the total number of electrons and ions remains constant.

The conservation of momentum can be expressed as follows

$$\rho_j \frac{d\mathbf{v}_j}{dt} + \mathbf{v}_j m_j \dot{n}_j = -\nabla p_j + \nabla \cdot \bar{\tau}_{vis} + \mathbf{F}_{ext} \quad (1.5)$$

Here p_j is the partial pressure of species j , $\bar{\tau}_{vis}$ is the viscous tensor and \mathbf{F}_{ext} represents all the external forces exerted on the plasma. Again a global equation can be derived and the creation/destruction term disappears because the total number of electrons and ions is constant.

The last conservation law is the conservation of energy. In this case a more rigorous description is required in general, separating ions and electrons characterized by different temperatures. For each species j the conservation of energy yields:

$$\frac{\partial \varepsilon_j}{\partial t} + \nabla \cdot [(\varepsilon_j + p_j)\mathbf{v}] = \nabla \cdot (\bar{\tau}_{vis} \cdot \mathbf{v}) + \nabla \cdot (\kappa_j \nabla T_j) + \dot{q}_j \quad (1.6)$$

where ε_j is the sum of the internal energy and the kinetic energy of species j , T_j its temperature, κ_j the thermal conductivity and \dot{q}_j the heat sources. The equation

of state relating the temperature, the pressure and the density completes the fluid-like description of the plasma. In general the equation of state used to describe a high density, high-Z plasma created from a solid target by laser irradiation, is a composite model in which different descriptions are utilized for different plasma conditions [26].

Once all the heat sources/losses are accounted for, equations for the ion temperature and the electron temperature may be obtained. To describe the heat sources and losses it is necessary to account for ion-electron collisions, atomic losses, radiation and absorption of incident energy. Atomic losses refer to processes where the electron transfer part of its kinetic energy to an ion/atom to ionize it or excite it to a different energy state, for instance, electron impact excitation. Radiation is divided into processes involving two bound states (atomic transition), a bound state and a free electron (electron impact de-excitation), or free electrons (Bremsstrahlung¹). Between these three types of processes the characteristic emission spectrum of a plasma is formed, presenting spectral lines mixed with a background of continuous radiation (see fig. 1.2). Radiation trapping can be a mechanism of heat transport under certain conditions. This is, radiation emitted in a region of the plasma is reabsorbed in another region with different conditions (different temperature for instance).

¹Although the process involves an ion, it changes the energy of the free electron only and it is the accelerated electron who emits radiation

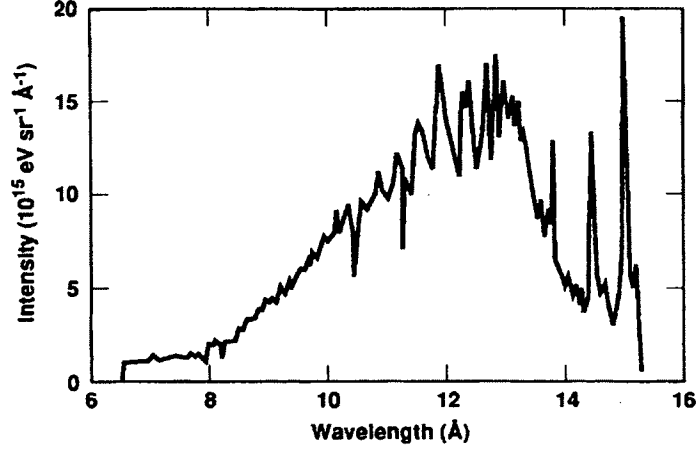


Figure 1.2: Typical plasma spectral emission with spectral lines superimposed with a continuum spectrum (From ref. [27])

Finally, for the free electrons the absorption of incident energy must be considered. Inverse Bremsstrahlung is often the dominant heating mechanism in laser created plasmas. Bremsstrahlung, or braking radiation is a process in which a free electron is deflected by an ion through Coulomb interaction, and in the deceleration process it emits a photon. Inverse Bremsstrahlung is the 3-body inverse process in which a photon is absorbed and a free electron interacting with an ion is accelerated. In a plasma dominated by free-free absorption (inverse Bremsstrahlung) the absorption coefficient in cm^{-1} is given by [28]:

$$\alpha \approx 2.44 \times 10^{-37} \frac{\langle Z^2 \rangle n_e n_i}{\sqrt{kT_e} (h\nu)^3} [1 - \exp(\frac{-h\nu}{kT_e})] \quad (1.7)$$

from which it can be seen that the absorption is stronger for longer wavelengths and increases quadratically with the electron density, since the ion density can be

written as $n_e/\langle Z \rangle$ with $\langle Z \rangle$ the mean degree of ionization. In equation 1.7 $h\nu$ and kT_e are in eV and n_e and n_i in cm^{-3} .

1.1.2 Transitions, population levels and gain

In order to predict population inversion and gain for a given transition in a plasma, it is necessary to calculate the population of many energy levels by solving rate equations in which the different levels are coupled through many different atomic processes. These processes are described by transition probabilities or cross sections, which in turn depend on plasma parameters such as the temperature or the density. Moreover, as it was mentioned in the previous subsection, the atomic processes affect the time evolution of the plasma, therefore the rate equations are coupled with the hydrodynamic equations. The most relevant atomic processes include:

- Electron impact ionization (or collisional ionization) where an electron collision ionizes an atom. Also its inverse, 3 body recombination.
- Photo ionization and the inverse process, radiative recombination. In the latter an electron binds to an ion and a photon is emitted carrying the excess in energy. In this way the emitted spectrum may result in a combination of continuous radiation mixed with spectral lines, since the bound electron may

be left in an excited state and undergo several radiative transitions in order to reach equilibrium.

- Dielectronic recombination. This is like radiative recombination, but instead of emitting a photon, the excess of energy is taken by a second bound electron, that goes to an excited state. After this the system may undergo auto-ionization to recover the initial ionic state plus a free electron, or decay through radiative cascades.
- Electron impact excitation (or collisional excitation). A free electron collides with an ion and transfer part of its kinetic energy, exciting the ion into a higher energy state. By the inverse process the ion decays to a lower energy state and the free electron gains kinetic energy
- Spontaneous emission
- Stimulated emission
- Stimulated absorption

Electron impact excitation is of particular interest for this work, since it is the main mechanism by which the upper laser level of a collisional soft x-ray laser is populated. It can occur between any two energy states within the ion, but the cross section is bigger for transitions in which the angular momentum is conserved. As an example, fig. 1.3 shows the rate coefficient as a function of electron temperature in

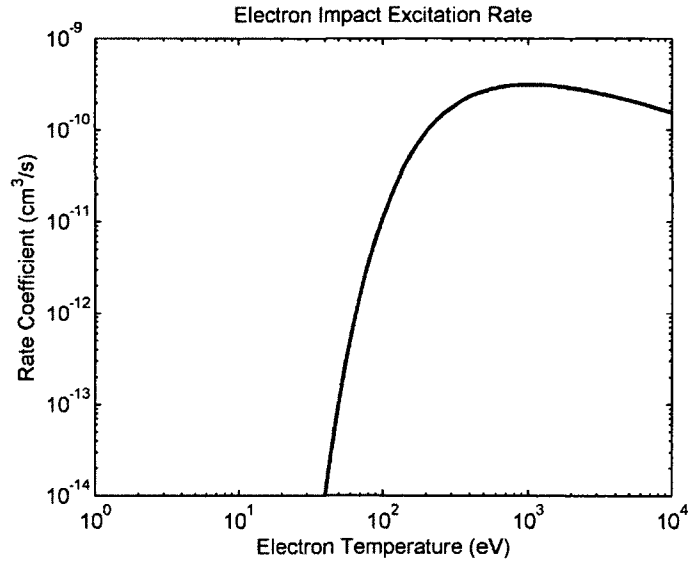


Figure 1.3: rate coefficient as a function of electron temperature in the transition $3d^{10} \ ^1S_0 \rightarrow 3d^9 4p \ ^1S_0$ of Ni-like Ag ions. (From ref. [25])

the transition $3d^{10} \ ^1S_0 \rightarrow 3d^9 4p \ ^1S_0$ of Ni-like Ag ions (from ref. [25]). The energy of the transition is ~ 500 eV. From Fig. 1.3 we can see that the rate coefficient peaks for electron temperatures slightly over the transition energy. On the other hand, it goes rapidly to zero for $T_e < 100$ eV, because for a plasma with such an electron temperature, only very few electrons have enough kinetic energy to excite the transition.

With all the transition rates coupling the energy levels the rate equations can be solved to obtain the population levels and from this, the population inversion between the upper and lower laser levels (ΔN_{21}). Once the population inversion

is solved, the small signal gain coefficient can be computed as:

$$g = \sigma_{21} \Delta N_{21} \simeq \frac{A_{21} \lambda^2 \Delta N_{21}}{8\pi \Delta\nu} \quad (1.8)$$

where σ_{21} is the stimulated emission cross section, λ the central wavelength of the transition, A_{21} is the spontaneous emission rate coefficient and $\Delta\nu$ is the width of the transition.

From equation 1.8 it is clear that another important parameter to calculate the gain is the line width of the transition. Since the excited levels have a finite lifetime, any given transition will have a certain width (in frequency or energy) determined by the uncertainty principle. The resulting line shape is Lorentzian and the corresponding broadening mechanism is referred to as natural broadening. Collisions will shorten the lifetime and hence, increase the line width, but they won't change the functional shape. Another important broadening mechanism in a hot and dense plasma is Doppler broadening. Since the emitting ions have different velocities, a Doppler shift is observed in their emissions. Assuming that the velocity distribution is a Maxwellian one, it can be shown [29] that the line shape has the same functional form, this is a Gaussian shape. The Full Width at Half Maximum (FWHM) of the line is given by:

$$\Delta\nu = \nu_0 \left(\frac{8kT_i \ln(2)}{mc^2} \right)^{1/2} \quad (1.9)$$

where T_i is the ion temperature, k the Boltzmann constant, c the speed of light and m is the mass of the emitting ions. In general, the line shape is a convolution

of the different line shapes involved due to the different broadening mechanisms.

1.1.3 ASE lasers and refraction effects

As it was mentioned in section 1.1, the short gain lifetime combined with the lack of cavity mirrors for soft x-ray wavelengths presented a challenge for the development of lasers in this spectral region. It was recognized that lasing would have to be achieved in a single or double pass through the gain medium. In this configuration without feedback, lasing is achieved through amplified spontaneous emission (ASE). For efficient operation gain saturation has to be reached in a single or double pass, imposing a demanding requirement on the gain-length product (gL).

An expression of the total intensity coming out of a gain medium due to ASE can be calculated analytically if some approximations are made. The total intensity (spectrally integrated) can be expressed as [30]:

$$I = \frac{A (e^{gL} - 1)^{3/2}}{g (gL e^{gL})^{1/2}} \quad (1.10)$$

In this expression g is the small signal gain coefficient, L the length of the gain medium, and A is a constant related to the number of spontaneous photons emitted per unit time. Although some more general relations have been developed [31], the Linford formula (formula 1.10) is generally accepted in the field and widely used to calculate the gain-length product from experimental data.

Another difficulty to achieve lasing is the effects of refraction, or refraction losses. Since amplification of x-ray photons must be achieved through propagation of these photons through a plasma column, the gradients of index of refraction within the plasma may bend the optical path of the emitted radiation, and in the worst case, eject the photons out of the gain region. Therefore, this represents a source of losses and even imposes a restriction in the maximum length for the plasma column. The effects of refraction in a plasma column were summarized in a paper by London [32]. The index of refraction in a plasma is given by (see for example ref. [33])

$$\eta = \sqrt{1 - \frac{n_e}{n_c}} \quad (1.11)$$

where n_e is the electron density and the critical density n_c is given by:

$$n_c = \frac{4\pi^2 \epsilon_0 m_e c^2}{e^2 \lambda^2} \quad (1.12)$$

For a given wavelength, the critical density marks the limit beyond which electromagnetic waves will not propagate into the plasma. So, in order to model the optical path followed by the emitted radiation (ray tracing) within the plasma, the electron density profile must be known. For the sake of simplicity, London assumed a parabolic profile in the direction perpendicular to the target of a laser created plasma (x direction in Fig. 1.4) and constant in other directions, which reproduces qualitatively the measured and calculated profiles. According to his calculations, beyond a typical length L_r called refraction length, the effects of refraction are

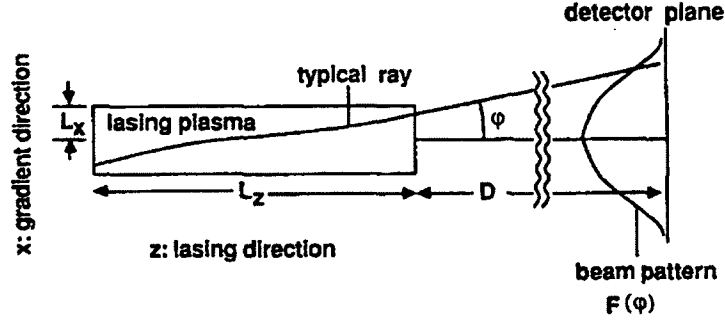


Figure 1.4: Schematic of an x-ray laser gain medium and the beam profile (from ref. [32])

too big, and the trajectories bend out of the plasma. The refraction length can be written as

$$L_r = L_x \left(\frac{n_c}{n_m} \right)^{1/2} \quad (1.13)$$

where n_m is the maximum electron density. For a given wavelength (and hence, critical density), the refraction length will be smaller for higher electron densities.

The divergence of the beam exiting the plasma column is given by the refraction angle:

$$\phi_r = \left(\frac{n_m}{n_c} \right)^{1/2} \quad (1.14)$$

From equation 1.14 it is clear that the divergence increases with the electron density.

In a plasma with a population inversion characterized by an unsaturated gain coefficient g_0 , the gain-length product may show different behaviors depending on the value of the product $G_r = g_0 L_r$. If $G_r < 1$ the refraction is dominant and the

power on-axis coming out of the gain medium reaches a constant value for large L_z . If $G_r > 1$ two cases may be identified: for $L_z < L_r$ the power grows according to an effective gain coefficient $g_{eff} = g_0 - 1/(2L_z)$ before saturation effects take over. On the other hand, if $L_z > L_r$ the gain coefficient reaches a limiting value $g_{eff} = g_0 - 1/(L_r)$, with the effects of refraction losses represented clearly by the term $-1/(L_r)$. The different cases are illustrated in fig. 1.5

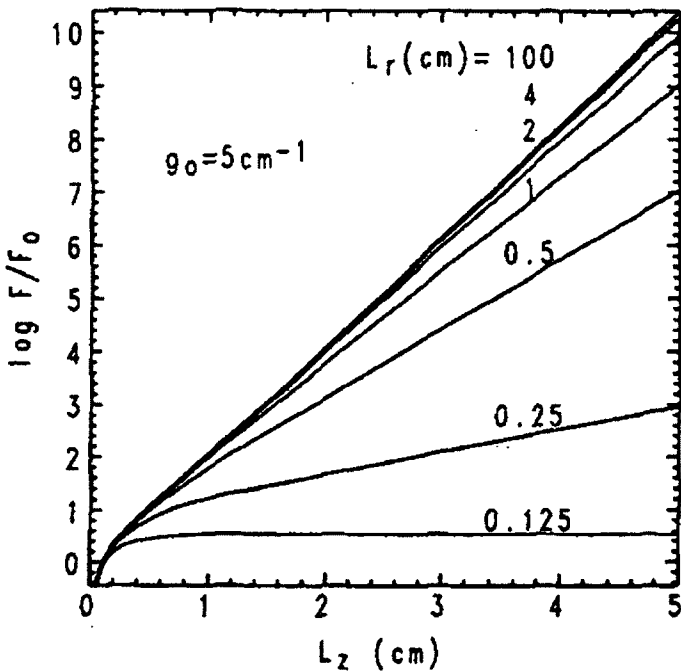


Figure 1.5: On-axis flux as a function of plasma column length. Cases with different values of G_r are illustrated. From ref. [32]

1.2 Population inversion mechanism: Electron impact excitation

There are different pumping mechanisms for producing a population inversion in transitions emitting soft x-ray photons: electron impact excitation, collisional recombination, photoionization and resonant photopumping. The photoionization pumping scheme has been demonstrated for lasers with emission wavelengths down to the vacuum ultra violet (VUV) [34–37]. However, up to date, no gain has been observed for lasers based on photoionization at wavelengths in the soft x-ray region of the spectrum. Several attempts have been made to construct a laser based on resonant photopumping [38–43], and even though in some of these experiments gain was reported, strong amplification has not been demonstrated up to date. In the case of collisional recombination, strong amplification has been demonstrated with different configurations [44–46], but it has not been possible so far to operate any of these lasers in saturation regime. In contrast, soft x-ray lasers based on electron impact excitation have been successfully operated under many different experimental conditions and it is the pumping mechanism of interest for this work.

Electron impact excitation is a very well known mechanism for generating a population inversion in gas lasers such as the visible Argon laser [29]. In this scheme, the atoms of the gain medium are ionized to a certain level (ionized once in the case of the Argon laser) and excited to upper energy levels directly from the ground state through collisions with free electrons. A quasi-cw population inversion can be created when the radiative lifetime of the upper level is much

larger than that of the lower laser level. The main difference between the well known ion-argon laser and a soft x-ray laser is the required level of ionization. A practical example of this is the Ni-like molybdenum laser at 18.9 nm that requires ionizing the molybdenum atom 14 times to obtain the required ion species.

As it was mentioned in section 1.1, in order to produce the required population inversion, a very hot, very dense plasma must be created. To generate a population inversion in transitions with wavelengths smaller than 20 nm, typically the electron density is $n_e \gtrsim 10^{20} \text{ cm}^{-3}$ and the electron temperature $T_e \gtrsim 100 \text{ eV}$. Let's note here that 1 keV corresponds to a temperature of $1.16 \times 10^7 \text{ K}$.

The ion species most widely explored experimentally and theoretically correspond to the neon-like and the nickel-like series. In these ion species, the ground state has a closed shell: $2p^6$ for neon-like and $3d^{10}$ for nickel-like ions. The closed shell configuration makes these ions more stable than other species (because of higher ionization potentials) and consequently, it is possible to create plasmas with large populations of the mentioned species.

In the following subsections the historical evolution of soft x-ray lasers pumped by electron impact excitation in laser created plasmas will be reviewed.

1.2.1 Ne-like collisional lasers pumped by a single, long laser pulse

The idea of using a high-power optical laser to heat a plasma and produce a population inversion between the energy levels $2p^53p$ and $2p^53s$ of Ne-like ions,

has been studied since 1976 [47, 48]. The $3p$ upper levels are populated mostly by direct impact excitation from the ground state of the Ne-like ions. A small fraction of the population may also come from recombination from F-like ions, cascades from higher energy levels and possibly, inner shell ionization of Na-like ions. A quasi-cw population inversion was predicted to occur based on the upper laser levels being metastable with respect to dipole allowed transitions to the ground state, while the lower laser levels are strongly coupled to the ground state through radiative decay (dipole allowed transitions). Under these conditions, the plasma has to be optically thin with respect to the transitions from $3s$ levels to the ground state and therefore, the maximum plasma column diameter is restricted, although this restriction is relaxed by Doppler shift in the lines caused by radial velocity gradients. In fig. 1.6 the simplified Grotrian diagram of the Ne-like ion scheme is presented for the case of Ne-like Germanium.

The $J = 0 \rightarrow 1$ transition had been predicted to have higher gain than the $J = 2 \rightarrow 1$ transition because of a higher collisional excitation rate towards the $3p$ $J = 0$ level. Experimentally however, higher gain was observed for $J = 2 \rightarrow 1$ lines, except for experiments in which the ion species had low Z . In the next few paragraphs some of the early experiments concerning Ne-like collisional lasers will be summarized.

It was not until 1984 that a conclusive demonstration of gain in this type of lasers was achieved experimentally. The work by Matthews *et al.* [50] at Lawrence

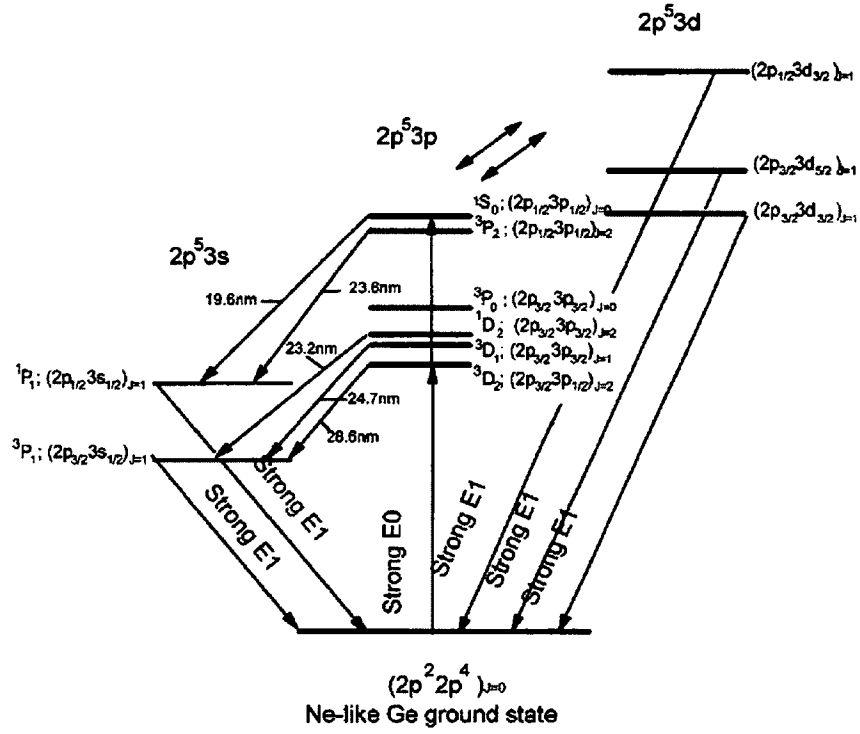


Figure 1.6: Simplified Grotrian diagram of Ne-like Ge showing the laser transitions and the dominant excitation and deexcitation processes. E_0 and E_1 refer to monopole and dipole allowed transitions respectively. (From ref. [49])

Livermore National Laboratory showed undisputed evidence of gain in Ne-like selenium. This is considered, together with a recombination laser demonstrated by Suckewer [44], to be the first demonstration of a soft x-ray laser.

To produce the required plasma, two beams of the Novette laser-target irradiation facility were focused with a line shape of $0.02 \text{ cm} \times 1.12 \text{ cm}$ on an exploding-foil target. A schematic of the beams irradiating the target can be seen in fig. 1.7. The target was made depositing a 75 nm layer of Selenium on a $1.5 \mu\text{m}$

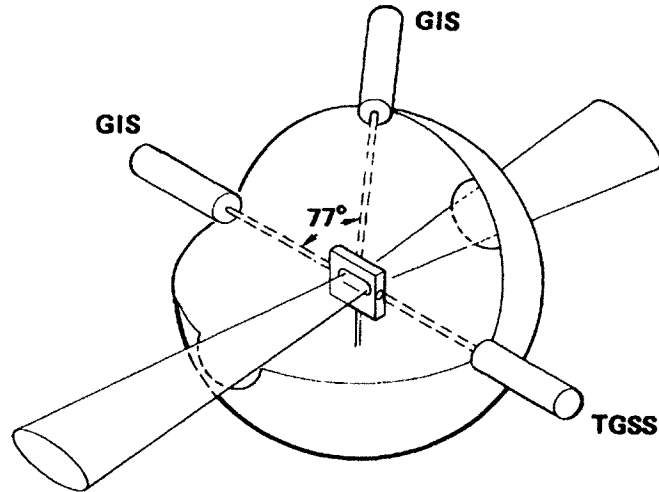


Figure 1.7: Target configuration for the first demonstration of amplification of spontaneous emission of soft x-ray photons

thick formvar² substrate. The laser pulses had a nominal duration of 450 ps and the intensity was 5×10^{13} W/cm². The pump laser wavelength was 532 nm. In another configuration they focused both beams one next to the other on the same side of the target to obtain a line focus of 0.02 cm \times 2.2 cm.

The on axis and off axis spectra from the plasma emission were taken with two grazing incidence spectrographs and one transmission grating spectrograph. In fig. 1.8 the spectrally resolved plasma emission showing the observed laser lines is plotted. As it was mentioned before, the maximum spectral line amplification was observed in $J = 2 \rightarrow 1$ transitions at 20.63 nm and 20.96 nm. The maximum

²Formvar is polyvinyl Formal, a polymer used to coat copper wire

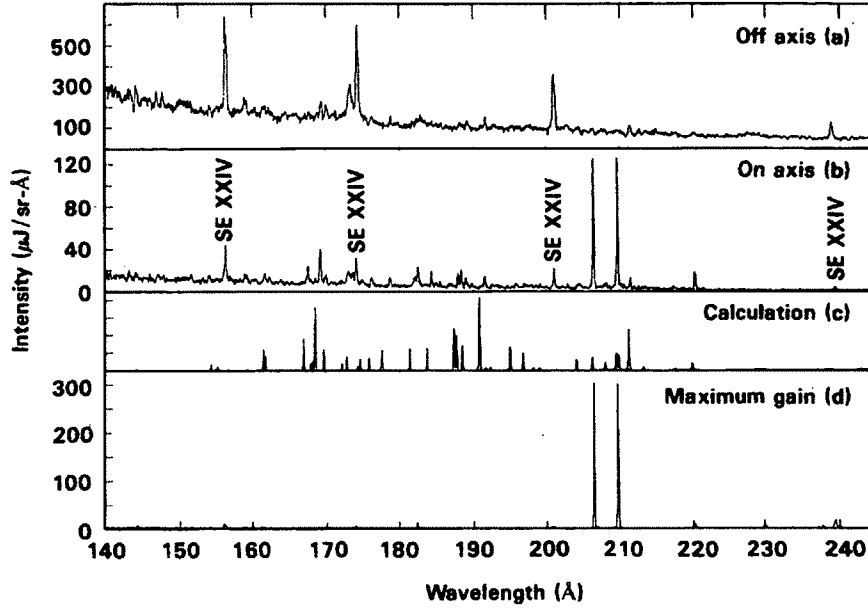


Figure 1.8: (a) Grazing incidence spectrograph (GIS) data from off-axis line of sight. Data taken from beginning of radiative output until 500 ps after peak of pump pulse. (b) On-axis GIS data from same interval as (a). (c) Calculated spontaneous spectrum on Ne-like Se. (d) On-axis GIS data from maximum gain target. Figure from ref. [50].

output power was observed using the 2.2 cm long line focus configuration. For that case a gain coefficient $\alpha = 5.5 \pm 1.0 \text{ cm}^{-1}$ was measured by fitting data of laser line intensity as a function of target length to the Linford formula 1.10. Also, by comparing the measured spectra with simulations, a plasma electron temperature of 1 keV and an electron density of 10^{21} cm^{-3} were estimated. They did not observe significant gain in the $J = 0 \rightarrow 1$ transition. The experiment was repeated with yttrium targets, yielding similar results: gain in $J = 2 \rightarrow 1$ transitions at 15.5 nm and 15.71 nm, but no gain observed in the $J = 0 \rightarrow 1$ line.

In 1987 T. N. Lee *et al.* [51], at the Naval Research Laboratory demonstrated for the first time, gain in transitions with $J = 0 \rightarrow 1$ by shooting germanium and copper slab targets, although stronger amplification was still observed in $J = 2 \rightarrow 1$ transitions.

Although lasing had been demonstrated in many transitions of different Ne-like ions down to 8 nm in Ne-like Ag [52], it was not until 1991 that saturation was demonstrated in a collisional soft x-ray laser. At the VULCAN laser facility in the United Kingdom, A. Carillon *et al.* demonstrated saturation in the $J = 2 \rightarrow 1$ line of Ne-like Ge at 23.6 nm [53]. In these experiments a two target configuration combined with a soft x-ray mirror to double-pass the double target configuration were implemented to reach saturation. The axial plasma emission showed for the first time saturation behavior (Fig. 1.9).

1.2.2 Extension to the Ni-like isoelectronic series

Nickel-like (Ni-like) ions had been studied theoretically as another possible lasing species for collisional x-ray lasers [54–56]. This was the selected new approach taken in order to reach shorter wavelengths. Ni-like ions offer a faster scaling to shorter wavelengths compared to Ne-like ions for a given ionization level, as can be seen from fig. 1.10, and in fig. 1.11 a simplified Grotrian diagram of a Ni-like system is presented.

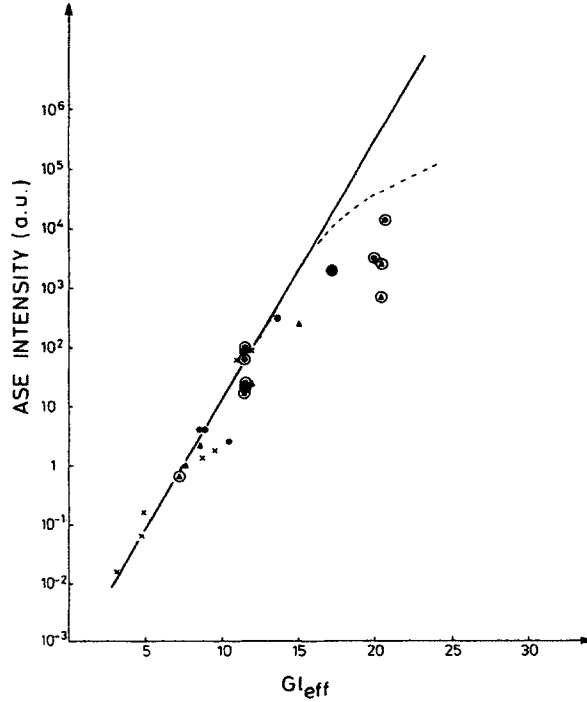


Figure 1.9: Amplified spontaneous emission intensity as a function of effective gain-length product in a Ne-like Ge plasma. Triangles correspond to angular distribution of the measured emission. The shots in which the mirror was used are circled. Crosses represent data from a previous experiment (no mirror). The dashed line shows departure from exponential growth. (from ref. [53])

The first observation of amplification in Ni-like ions was reported by MacGowan *et al.* in 1987 [57]. Amplification on $J = 0 \rightarrow 1$, $4p - 4d$ transitions of Ni-like Eu at 6.583 nm and 7.100 nm was reported, with a maximum gain coefficient of $(1.11 \pm 0.12) \text{cm}^{-1}$ for the latter. Two beams of the NOVA laser ($\lambda = 532$ nm) were focused into 200 μm wide line foci, in 1 ns pulses with a total intensity of $7 \times 10^{13} \text{W/cm}^2$. Exploding foil targets of EuF_2 were utilized in these experiments. Other transition lines were not observed to have exponential growth when

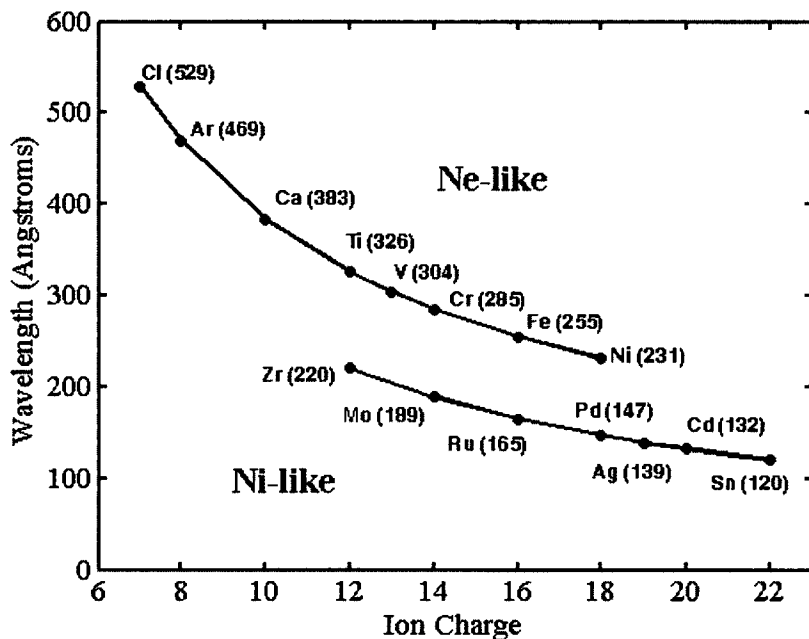


Figure 1.10: Laser wavelength as a function of ionization level for the Ne-like and Ni-like isoelectronic sequences

the length of the gain medium was increased. The authors also measured gain in Ni-like Yb at 5.026 nm utilizing again an exploding foil target configuration and a total intensity on target of $1.4 \times 10^{14} \text{ W/cm}^2$.

In the following years the Ni-like configuration was extended to wavelengths down to the water window, being Ni-like Au at 3.56 nm the shortest wavelength achieved [58, 59]. However, saturation was never demonstrated in this multi-kJ, single ns pump pulse configuration.

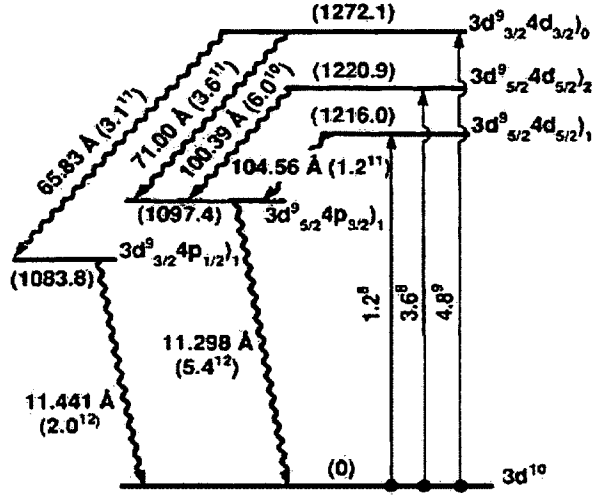


Figure 1.11: Simplified level diagram for Eu^{35+} . The collisional rates were calculated using $n_e = 2 \times 10^{20} \text{ cm}^{-3}$ and $T_e = 600 \text{ eV}$. The energies of the levels are given in eV and, in parentheses, the spontaneous emission rates are given. (From ref. [57])

1.2.3 Pre-pulse technique

The Ne-like and Ni-like isoelectronic sequences scale to very high electron density requirements with decreasing wavelength [49,60]. Not only shorter wavelengths require a plasma with higher electron density but in addition, the $J = 0 \rightarrow 1$ transition requires higher electron density compared to the $J = 2 \rightarrow 1$ transition for a given ion species [49]. This is the reason why the expected stronger transition was not observed in high Z ion species, as discussed in subsection 1.2.1. The population inversion for the $J = 0 \rightarrow 1$ transition takes place in a denser region of the plasma, where according to equation 1.13 the effects of density gradients and hence refraction, may cause the amplified spontaneous emission to get refracted

out of the plasma without the possibility of building up a large number of photons in the axis of the plasma.

Going back to equation 1.13, we see that the refraction length is proportional to the characteristic transverse dimension of the plasma L_x . Now, this parameter is changing with time as the plasma is expanding. In fact, the transverse dimension of the plasma L_x can be written as [1]

$$L_x = v_{exp}t = \sqrt{\frac{\gamma\langle Z \rangle kT_e t}{m_i}} \quad (1.15)$$

where t is the duration of the plasma expansion and γ is the thermodynamic ratio of specific heats. Since a bigger refraction length is desired to achieve a larger gain-length product, L_x and so t need to be increased.

Dividing the excitation process into a plasma creation and a plasma heating process allows the refraction problem to be addressed. The first pulse creates the plasma, which is then allowed to expand and cool. This has the advantages of creating a bigger gain region through increasing expansion time and relaxing density gradients, reducing then the gradients in the index of refraction, the source of refraction losses. Of course during expansion the plasma cools down, so the main effect of the second pulse is to heat the plasma to an electron temperature high enough to produce a population inversion. Although the multi-pulse excitation is the key here, the two pulse configuration given as an example is not crucial and, in fact, many other multi-pulse schemes have been successfully demonstrated.

The first experimental demonstration of the pre-pulse technique was done in 1993 by Nielsen *et al.* [61]. They observed strong amplification in low Z ($Z = 22, 24, 26$) Ne-like ions, where very weak amplification (for Ti^{12+}) or no amplification at all (for Cr^{14+} and Fe^{16+}) had been observed before. On top of that, the dominant transition was the $J = 0 \rightarrow 1$ as it had been predicted initially. Fig. 1.12 shows spectra with the lasing transitions observed. The driver laser consisted of a pre-pulse of 6 J and 600 ps and a main pulse of 1100 J also in 600 ps. The pre-pulse preceded the main pulse by 4-7 ns.

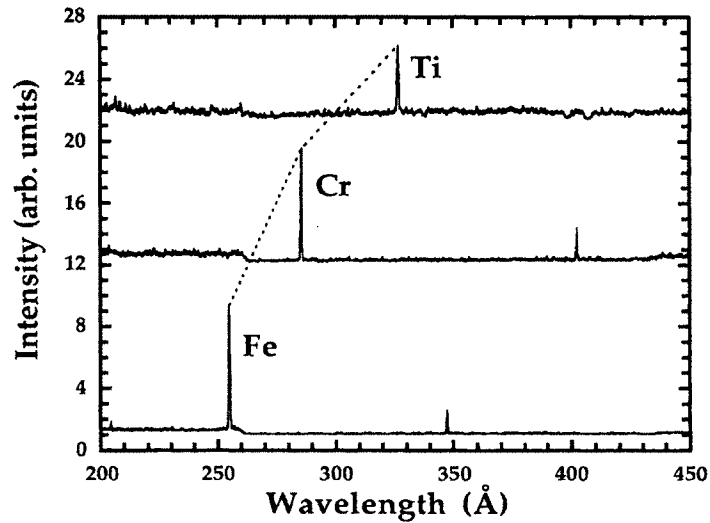


Figure 1.12: On-axis spectra from 3.8 cm long targets of Ti, Cr and Fe. The dotted line connects $J = 0 \rightarrow 1$ laser lines. (From ref. [61])

As another example of the multi-pulse excitation technique, it is worth mentioning ref. [62], where three pulses of 100 ps duration were used to create and excite the plasma. With this experimental set up (the rest is very similar to ref. [61])

they observed lasing in Ne-like Se, Ge, Zn and Ni with the $J = 0 \rightarrow 1$ transition being dominant by an order of magnitude.

In 1995 Li *et al.* [63] extended these results to the EUV region by demonstrating lasing in Sc, Ca, K and Cl with wavelengths ranging between 35.3 nm to 52.9 nm, using the ASTERIX IV iodine laser in Germany. Moreover, saturation was achieved in Ne-like Ge [64] and Ne-like Zn [65] with similar experimental configurations. Shortly after, the pre-pulse technique was applied to Ni-like lasers [66–68] and saturation was achieved in Ni-like Sm at 7.3 nm [69]. Something in common to all these experiments is that the required energy to drive the x-ray lasers was in the order of 100 J - 300 J.

Although the pre-pulse technique provided a better understanding of the physics involved, to reach saturation at many different wavelengths and decrease the required energy of the driving laser by almost an order of magnitude in some cases, these devices were still far from being compact laboratory devices suitable for applications.

1.2.4 Transient collisional excitation

In 1987 Afanas'ev and Shlyaptsev [70] studied different cases for population inversion and gain in Ne-like ions, exploring different time scales for the problem of electron impact excitation in laser created plasmas. As a conclusion to their numerical analysis, they indicated that in a plasma heated by a fast excitation,

in a transient approximation scheme (ionization times and relaxation of excited states times are smaller or in the same order than characteristic time of change of plasma parameters), very high values of gain, with $g \sim 10^2 \text{ cm}^{-1}$, may be produced. The analysis also applies to other isoelectronic sequences, as Ni-like ions for instance. In the transient case the population inversion arises because electron impact excitation populates preferentially the upper laser level, and not because of strong depopulation of the lower level as in the quasi steady state case. This high population inversion last only a few picoseconds before the lower level gets also populated. To effectively excite the plasma the heating process must be fast compared to the relaxation time of the upper level, demanding then high energy ultra-short laser pulses. The idea behind the excitation process is the creation of a plasma with a pre-pulse and, after relaxation of electron density gradients, the rapid heating of the plasma with a short pulse, without significant modification of the electron density.

The first demonstration of lasing by transient collisional excitation was accomplished in 1997 by Nickles *et al.* at the Max Born Institute, in Berlin [71]. Lasing was observed in the $3p - 3s, J = 0 \rightarrow 1$ line of Ne-like Ti at 32.6 nm. The driver laser consisted of a chirped pulse amplification (CPA) system [72, 73] based on a Ti:sapphire oscillator and a linear glass amplifier chain, producing a pre-pulse of 7 J in 1.5 ns and a short pulse of 4 J in 700 fs delayed 1.5 ns with respect to the pre-pulse. These pulses were focused on Ti slabs targets into a line focus of 1-5

mm by $30\ \mu\text{m}$. With only a short pulse, or two long pulses, no amplification was observed. A minimum of 4-6 J in the pre-pulse and 1.5 J in the short pulse were necessary to achieve amplification. Gain measurements revealed a small signal gain coefficient of $19\ \text{cm}^{-1}$, 7 times higher than in preceding experiments run with more than 200 J of pump energy. However, this laser was not saturated. According to the authors, the gain region had a very small lateral extension with steep density gradients, therefore, although the plasma length is an order of magnitude smaller than previous configurations, the refraction losses may be very important. On top of that, the short duration of the gain (less than 20 ps) is on the order of the transit time of the photon through the gain medium. As a consequence of that, by the time the photons emitted at one end of the plasma column reach the other end, the population inversion might not exist any longer, or it might have been dramatically reduced. Hence, the need for a traveling wave excitation (TWE) scheme in which different portions of the plasma are heated at different times, somehow matching the traveling soft x-ray photons.

There are many ways to implement a TWE scheme. These include dividing the wavefront in beamlets utilizing a stepped mirror where the delay between the wavelets is given by the depth of the steps [74] and tilting the wavefront by means of a diffraction grating as shown in fig. 1.13 [75].

In subsequent years other laser lines were demonstrated utilizing the transient excitation scheme and incorporating the TWE configuration. These include satu-

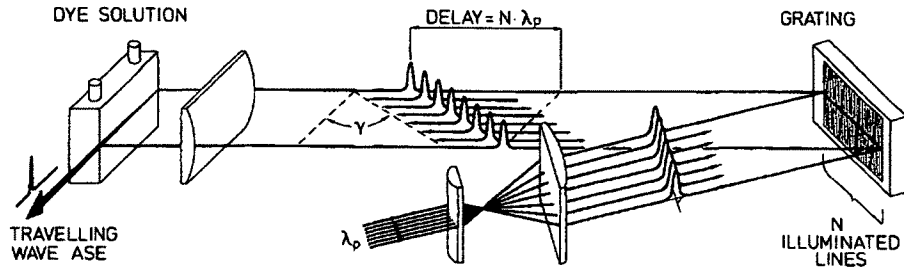


Figure 1.13: Example of a traveling wave excitation configuration. (From ref. [75])

ration of Ne-like Ti [76] and observation of high gain in Ne-like Ge at 19.6 nm [77]. Also Dunn *et al.* reported gain saturation of several Ni-like ions between 13.9 nm and 20.3 nm [78] (Fig. 1.14). In these experiments the energy of the driving lasers ranged between 5 J and 40 J and the output energies for saturated operation were in the order of 10 μ J.

1.2.5 Grazing incidence pumping: Table-top soft x-ray lasers

The transient collisional excitation (TCE) scheme utilizing an ultrashort heating pulse signified a great advance in the field of laser-pumped soft x-ray lasers, bringing down the energy necessary to excite the plasma down to ~ 10 J. However, the driver lasers in these experiments were not table-top devices yet, and the repetition rate was typically limited to a shot every several minutes.

To increase the repetition rate and reduce the size it was necessary to further reduce the required energy to pump soft x-ray lasers. Although amplification was

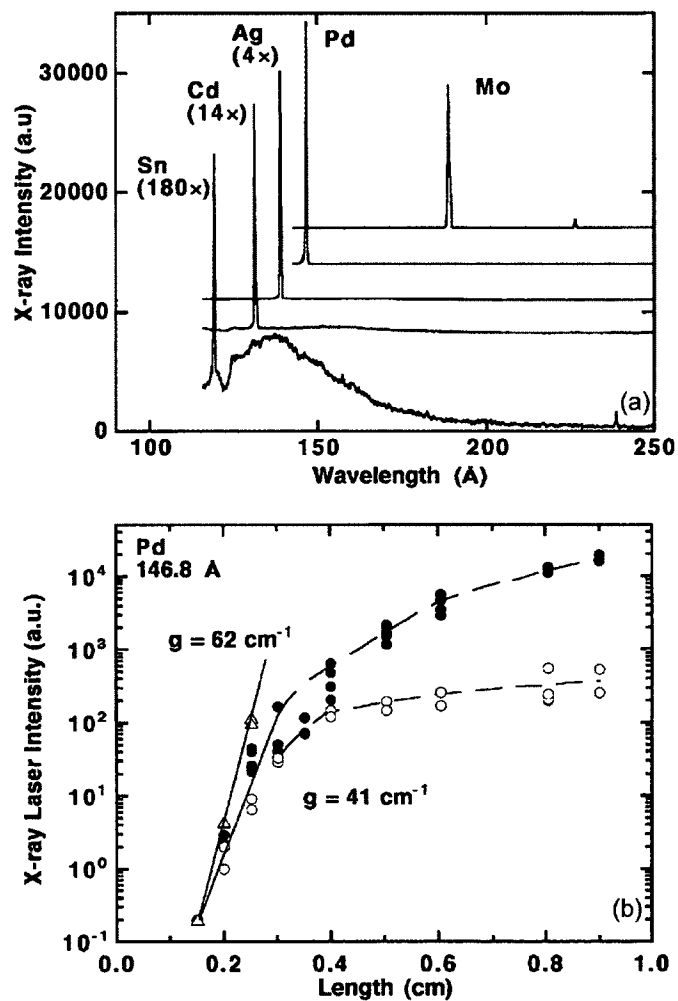


Figure 1.14: (a) Several spectra showing lasing in different Ni-like ions. (b) Intensity versus length for Ni-like Pd laser line evidencing saturation. Open circles are for data taken without TWE and full circles with TWE. Triangles are for data taken with less energy in the short pulse and a TWE configuration. (From ref. [78])

demonstrated in Ni-like Mo and Ne-like Ti using hundreds of mJ of pump energy in fs pulses, saturation could not be achieved [79–81]. Two of these experiments implemented a longitudinal pumping configuration [79, 80]. The limitation here is given by the fact that the pump energy is not homogeneously absorbed along the plasma column formed by a pre-pulse at normal incidence, and hence only small gain-length products can be achieved. On the other hand, with both pulses at normal incidence, the limitation comes again due to refraction losses. Most of the energy in the short pulse gets absorbed in a region of the plasma very close to the critical density, where refraction strongly reduces the gain-length product (see again equation 1.13). Only about 10% of the energy is absorbed in a region of the plasma where efficient amplification can be achieved.

A more efficient technique to deposit the energy of the short pulse in the region of the plasma where amplification takes place was investigated around 2003 [82, 83]. The grazing incidence pumping technique (GRIP) makes use of refraction of the pumping pulse in the plasma to deposit between 30% and 50% of its energy in the region with the proper electron density. Fig. 1.15 is a schematic of the referred configuration. The grazing incidence angle can be expressed as

$$\theta = \left(\frac{n_{em}}{n_{cp}}\right)^{1/2} \quad (1.16)$$

where n_{cp} is the critical electron density for the pump wavelength and n_{em} is the maximum electron density in the amplification region. From this expression it

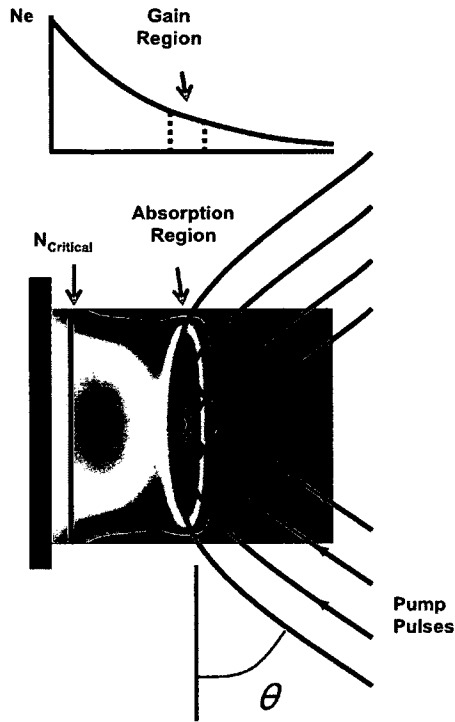


Figure 1.15: Illustration of the grazing incidence pumping (GRIP) configuration. θ is the grazing incidence angle

is evident that by scanning different angles of incidence one can scan different regions of the electron density profile where the pump energy is deposited. In this way, an optimum angle of incidence can be found. Furthermore, the GRIP configuration is intrinsically a TWE configuration. From Fig.1.15 it is easy to estimate the mismatch between photon transit time and TWE transit time as $\Delta \sim (L/c)(1 - \cos(\theta))$. This mismatch can be kept small compared to the duration of the gain if the length of the plasma column or the angles of incidence are kept small.

The GRIP configuration made it possible to develop table-top soft x-ray lasers with wavelengths between 10.9 nm and 32.6 nm in Ni-like and Ne-like ions. This technique was implemented for the first time to demonstrate amplification in Ni-like Mo at 18.9 nm, at repetition rates between 5 Hz and 10 Hz [84–86]. Experiments at Colorado State University utilized a Ti:sapphire CPA system with a total energy of 2 J to achieve saturation of many laser lines including the 13.2 nm line of Ni-like Cd, of great interest for the semiconductor industry [85–91]. In these experiments the pre-pulse, having a duration of 120 ps was incident at normal incidence on the solid target, and the short pulse (typically 6 ps - 12 ps) impinged at grazing incidence focused by a toroidal mirror. The line focus had dimensions of 30 μm by 4 mm and the targets were either solid slabs or helicoidal targets to allow for many hours of operation. The average power of these soft x-ray lasers was in the order of 2 μW . For the first time a table-top soft x-ray laser with sufficient average power for applications became available at sub-20 nm wavelengths. The measured gain coefficient in the case of the Ni-like Cd laser was 69 cm^{-1} and the gain-length product was 17.6. These soft x-ray lasers were also characterized by measurements of the pulsewidth, spatial coherence and effects of the short pulse duration and time delay between the pre-pulse and the short pulse [92–94]. It was also discovered that the introduction of a very low energy pulse ($\sim 10 \text{ mJ}$) preceding the pre-pulse by several ns may enhance the soft x-ray laser performance.

Fig. 1.16 shows some of the lasing lines and a gain measurement of the saturated Ni-like Cd laser.

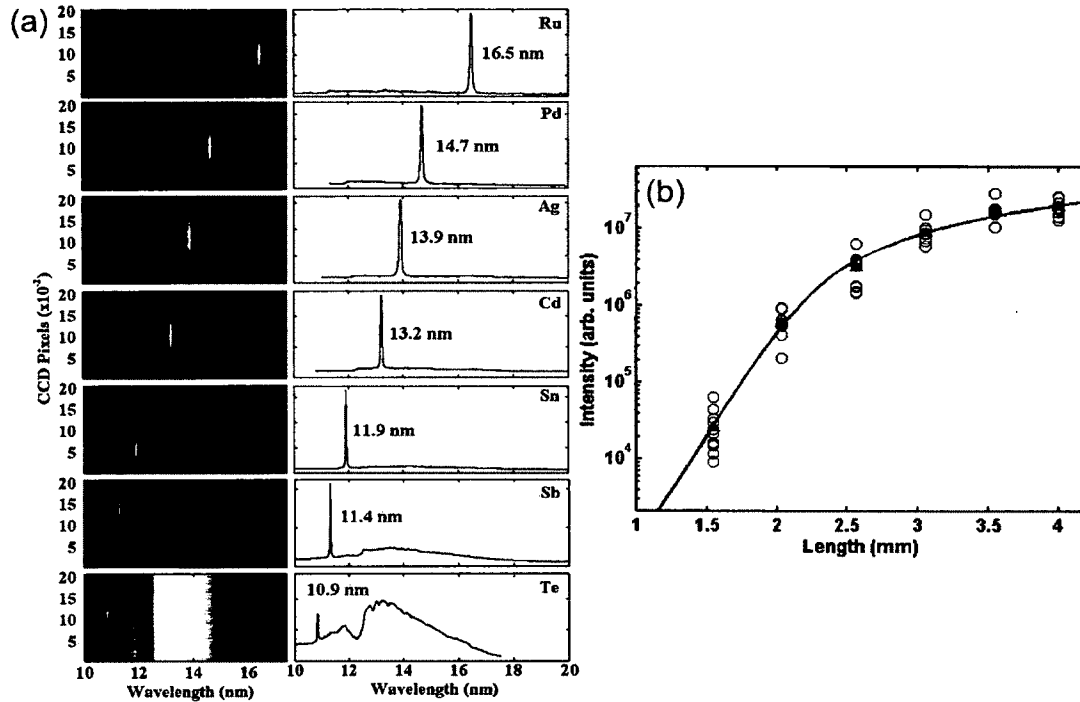


Figure 1.16: (a) Several laser lines between 16.5 nm and 10.9 nm. (a) Gain measurement for the Ni-like Cd laser at 13.2 nm where it can be seen that the laser is operating under saturation conditions (From ref. [87, 88])

The spatial and temporal coherence of the soft x-ray laser at CSU was greatly improved by seeding the gain medium with short pulses at soft x-ray wavelengths generated from high harmonics of the 800 nm laser [95, 96]. The population inversion and gain are produced in the same way, but the amplified seed intensity overcomes the ASE and a fully phase coherent output is obtained. In this way, the created plasma is used as an amplifier for the harmonics. The seeded soft x-ray

laser has a divergence approximately 10 times smaller than the unseeded laser. A Young's double slit interference experiment shows that the seeded soft x-ray laser has practically full spatial coherence. Fig. 1.17 shows a sketch of the experimental setup and fig. 1.18 shows spectra taken in three different conditions: unseeded soft x-ray laser, unamplified high harmonics, and amplified high harmonics, for 13.9 nm. With this setup it has been possible to generate fully coherent soft x-ray laser pulses with a duration of 1 ps.

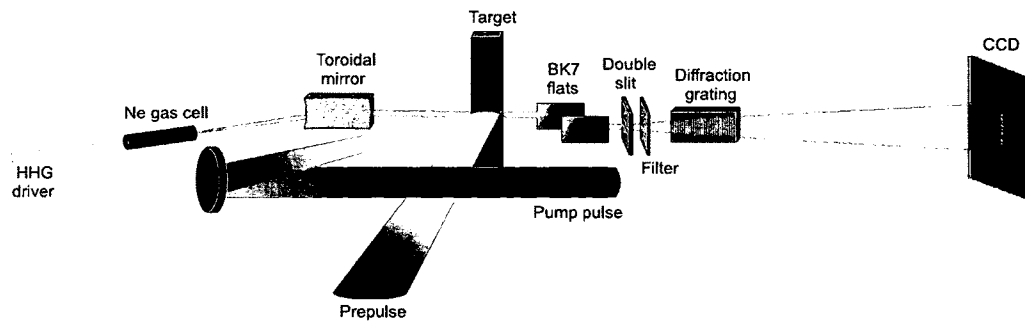


Figure 1.17: Experimental setup for the seeded soft x-ray laser (From ref. [95])

1.3 State of the art of driver lasers for pumping soft x-ray lasers

The TCE-GRIP configuration has been successfully employed in several facilities around the world to generate soft x-ray lasers [84, 88, 89, 97–100]. A common characteristic to all of them is that the driver laser is a chirped pulse amplification (CPA) system based on flash lamp pumping of the amplification stages, delivering typically pulses of several hundred millijoules to a few Joules with durations of less

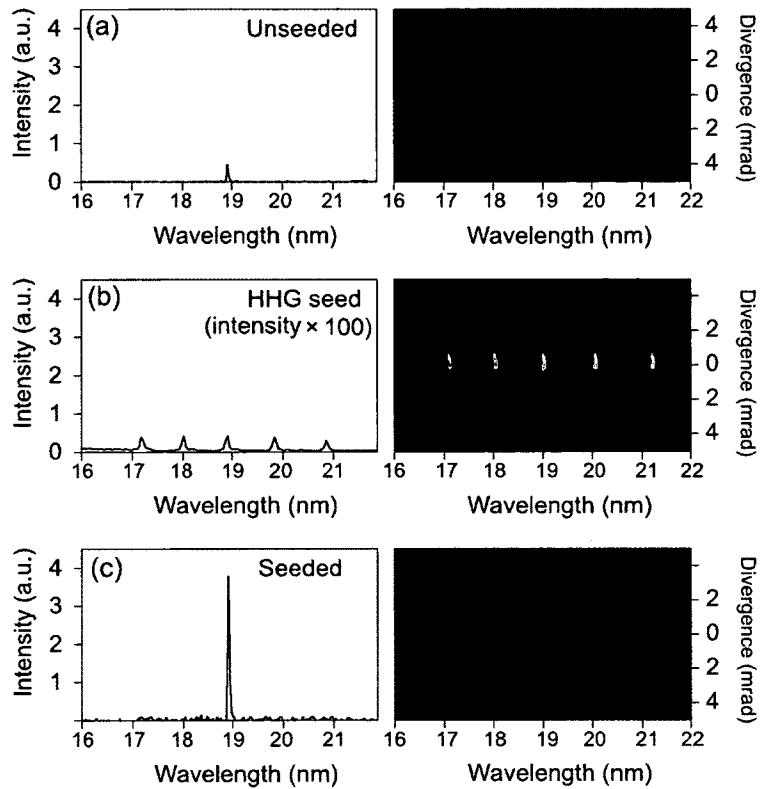


Figure 1.18: Spectra illustrating the relative intensity and beam divergence of a 13.9 nm laser for different setups: unseeded soft x-ray laser (a); High Harmonics seed (b); seeded soft x-ray laser (c). (From ref. [95])

than 10 ps. In the following subsections the main characteristics of these systems are going to be reviewed.

1.3.1 Chirped pulse amplification systems

Amplification of high energy ultrashort laser pulses has been a topic of research for more than twenty years. From an experimental point of view it is challenging to generate ultrashort laser pulses of several picosecond or femtosecond duration and

whose energies exceed the millijoule range. The problem when amplifying short pulses is that the intensity of the short pulses reaches quickly values high enough for non-linear interactions to take place between the electric field of the laser pulses and the optical components of the system. The non-linear interactions are usually deleterious during the amplification process. They can generate unpredictable wavefront distortions leading to self-focusing effects that, in turn, may produce damage of optical components. At the same time, they can produce undesired distortions to the temporal profile of the pulse. An estimation of the nonlinear effects accumulated through the amplification process can be calculated through the so called B -integral, given by:

$$B = \frac{2\pi}{\lambda} \int n_2 I(z) dz \quad (1.17)$$

where n_2 is the nonlinear index of a given material, $I(z)$ is the intensity of the laser in that material and the integration is over the length of the material. The integral must be calculated by adding all the non-negligible contributions in the amplifiers, which typically come from the gain medium, windows, lenses and other components such as Pockell's cells or Faraday rotators. The value of the B -integral is the total nonlinear phase shift and as a rule of thumb, it is desirable to keep it below 1, although many amplifiers work with higher B -integral values.

In order to avoid these detrimental effects during the amplification process, the intensity of the pulses must be kept small so that the non-linear effects are negligible. The first approach to reduce the intensity is obviously increasing the beam

size. However this approach presents two limitations: First, energy extraction in an amplifier is more efficiently accomplished if the amplifying pulses reach the saturation fluence of the gain material, and increasing the size of the beam reduces not only the intensity but the fluence as well. The second limitation is more of a technological one. If the size of the beam had to be increased over and over, very large area optics would be necessary in order to build amplifiers. Keeping a good wavefront across a big area is not easily accomplished and furthermore, there is a limitation on how big a crystal can be grown for many laser crystals. Therefore, solely increasing the beam size is not a viable strategy for ultrashort laser pulse amplification.

The problem is solved using dispersive delay lines that can stretch and compress the duration of the pulses in a controlled fashion. In 1969 Treacy [101] showed how an optical arrangement based on a pair of gratings can introduce a delay that is wavelength dependent. In this way, when an ultrashort pulse comprising many wavelength components goes through the grating pair, the different spectral components of the short pulse are spread out in time and therefore the duration of the pulse is stretched. This concept by itself is not shocking at all, material dispersion itself produces the same effect. The interesting phenomena to highlight here is that material dispersion produces a positive chirp in the pulse, meaning that lower frequencies travel at the front of the pulse while higher frequencies lie at the end of the pulse. But Treacy's grating pair produces the opposite effect, a negative chirp.

Strickland and Morou proposed in 1985 [72] to use this idea to amplify ultrashort pulses. An optical fiber introduces a large amount of positive chirp in the pulses and stretches the duration to the nanosecond range. Subsequently the pulses are amplified to the required energy level without reaching high intensities. Finally, the pulses are compressed in time by compensating the positive chirp utilizing a grating pair. The idea was further improved by Martinez [73], who designed a better way to introduce a controlled positive chirp, based on the combination of a grating pair and a telescope with a magnification $M = -1$. This setup is known as chirped pulse amplification (CPA) and is the standard technique to amplify ultrashort pulses. A sketch of a typical CPA system is shown in fig. 1.19.

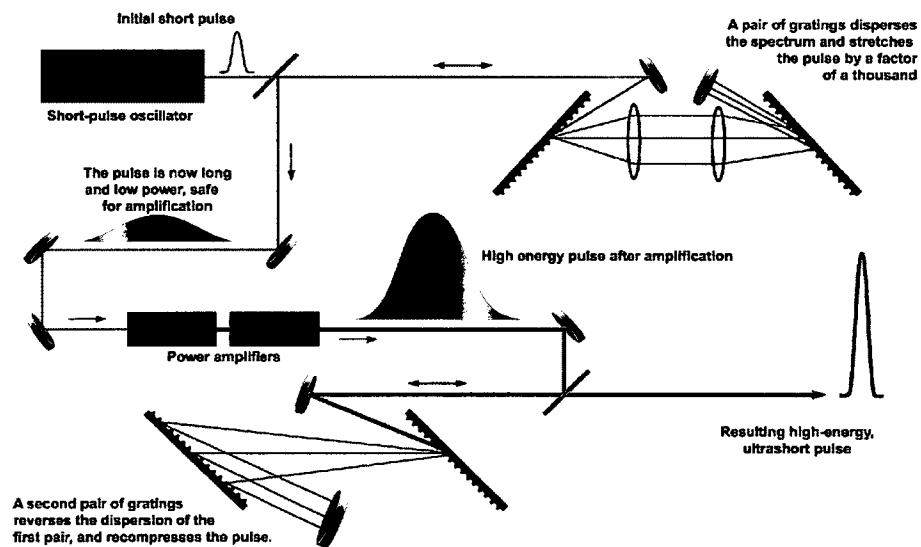


Figure 1.19: Sketch of a chirped pulse amplification system (from ref. [102])

1.3.2 Amplifiers pumped by flash lamps

For many years now, ultrafast high power laser amplifiers have been based on solid state laser crystals such as Nd:glass or Ti:Sapphire. These materials have the attractive characteristics for high energy, ultra short pulse amplification of a relatively long upper level lifetime (hundreds of μs to ms), high saturation fluence ($\sim 1 \text{ J}/\text{cm}^2$), broad bandwidth to support fs-ps pulses and high damage threshold. In fig. 1.20 diagrams of a Nd:glass CPA system and a Ti:Sapphire CPA system, both used as driver lasers for laser driven soft x-ray lasers, are shown.

It is common to both systems the use of flash lamps to pump the power amplifiers. In particular, in Ti:Sapphire systems, flash lamps are used to pump Nd-doped Q-switch laser systems that, after frequency doubling in a non-linear crystal (typically KDP), are used to pump the Ti:Sapphire crystals. This inefficiency in the pumping process makes the system complex and costly. But on top of that, it is intrinsic to flash lamp pumping, that a large amount of heat is generated in the gain materials. Consequently, this sets a limit to the repetition rate due to thermal problems such as thermal lensing, thermal stress inducing birefringence and depolarization and eventually, thermal shock breaking the materials. The thermal problem in flash lamp pumped systems arises because flash lamps emit a very broad spectrum of light (Fig. 1.21), therefore during the pumping process not only the upper laser level is populated but also a whole set of other levels that relax mostly through non-radiative transitions that generate heat in the material.

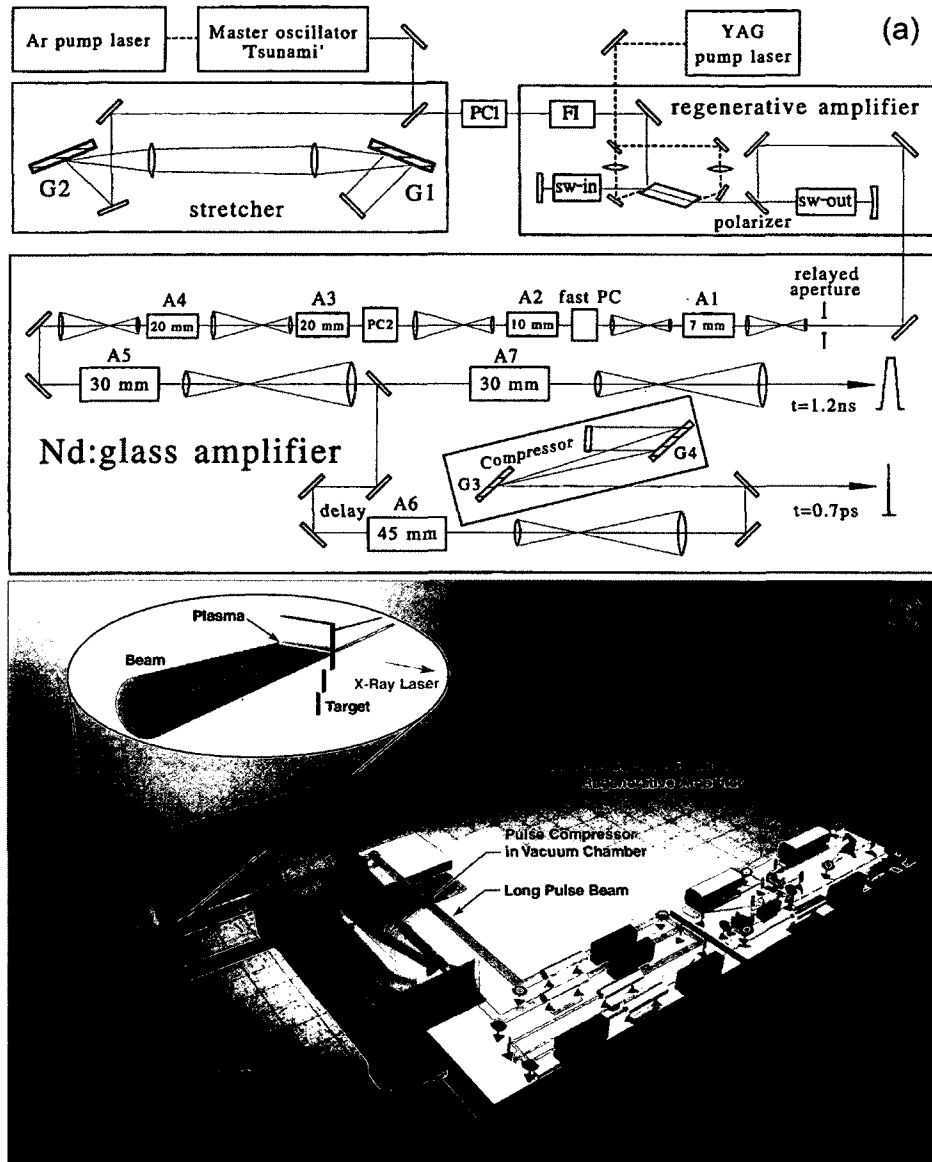


Figure 1.20: (a) Block diagram of a CPA system developed at the Max Born Institute to pump transient collisional excitation lasers (from ref. [49]) (b) 3D illustration of the CPA and target chamber developed at Lawrence Livermore National Laboratory (from ref. [49])

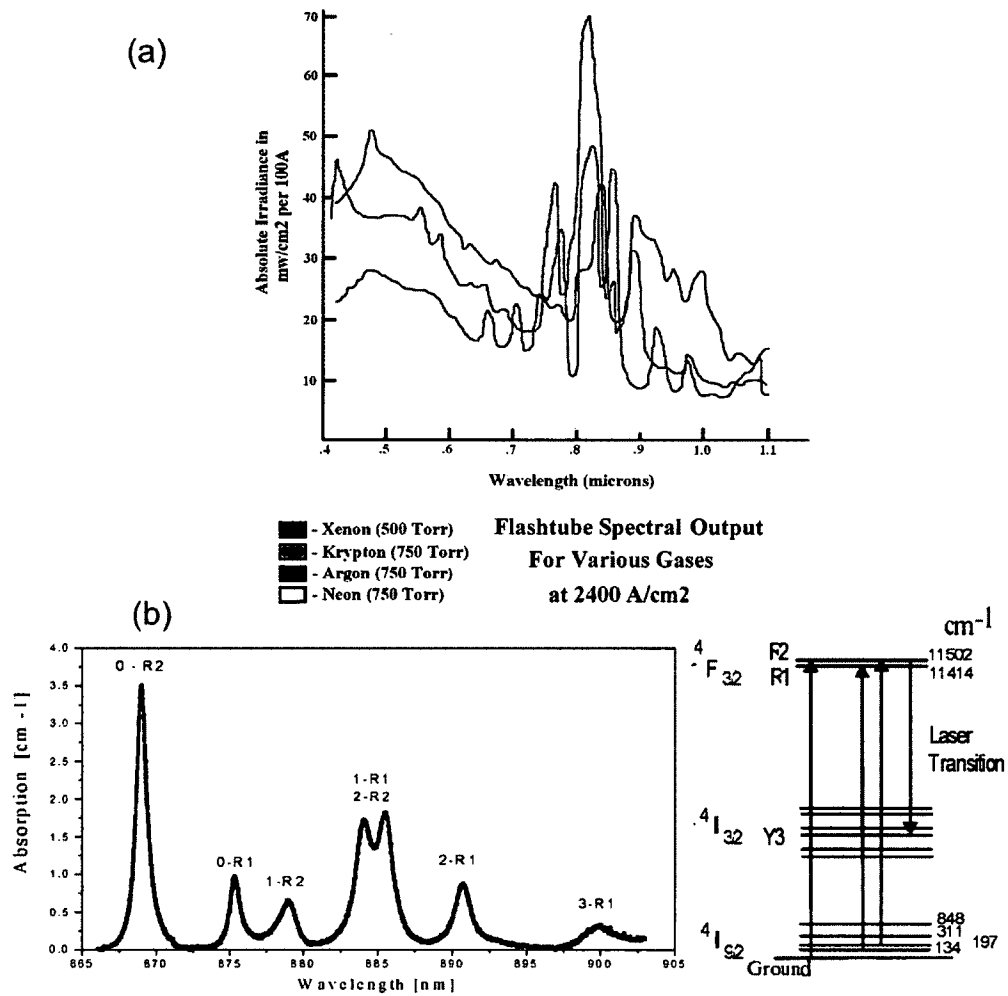


Figure 1.21: (a) Emission spectra of flash lamps with different gases (from ref. [103]). (b) Absorption spectra and energy levels of Nd:YAG (from ref. [104])

The amount of generated heat is directly proportional to the average pump power and this to the repetition rate at which the flash lamps are working, hence the limitation to the repetition rate.

State of the art chirped pulsed amplification systems to pump soft x-ray lasers are Ti:Sapphire systems delivering less than 10 J of energy per pulse, occupying a few standard optical tables and are limited in repetition rate to about 5-10 Hz. In fig. 1.22 a picture of the Ti:Sapphire system developed at Colorado State University may be seen.

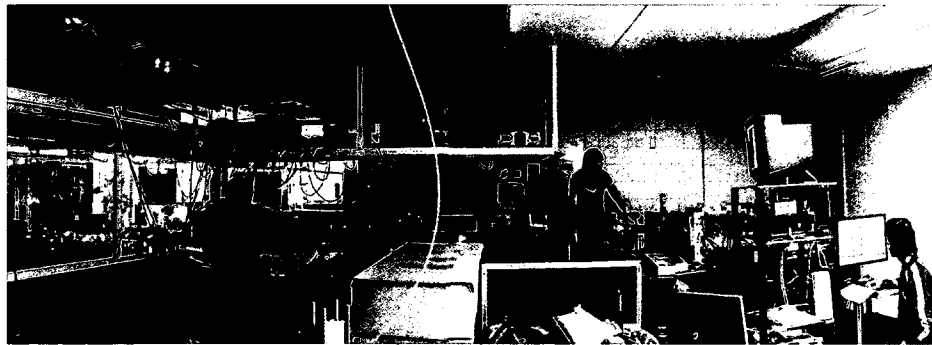


Figure 1.22: Picture of the Ti:Sapphire CPA system and target chamber developed at Colorado State University

1.3.3 The promise of laser diode pumping

To overcome these limitations in repetition rate we undertook the development of an all diode-pumped chirped pulse amplification system designed to serve as a driver laser for soft x-ray lasers. This is the main objective of this work. Pumping

small quantum defect materials such as Yb:YAG, with a narrow bandwidth source of the optimum wavelength will allow for soft x-ray laser operation at unsurpassed repetition rates. Our approach includes cryogenic cooling of the gain materials which, in combination with direct diode-pumping results in the design of CPA laser systems that are much more efficient and compact than currently used driver lasers. These characteristics make a diode-pumped system a very attractive candidate for a new generation of more compact, higher repetition rate soft x-ray lasers that will have a great impact in most of the current applications, and will probably enable new applications that require higher average power. In the following chapters an extended introduction to the advantages of diode-pumped CPA systems will be given. Also, a complete description of the system developed for this dissertation will be presented and the results obtained will be discussed, including the first demonstration of an all-diode pumped soft x-ray laser.

Bibliography

- [1] David Attwood. *Soft x-rays and extreme ultraviolet radiation*. Cambridge University Press, 2000.
- [2] Raymond C. Elton. *X-Ray Lasers*. Academic Press Inc., 1990.
- [3] F. Brizuela, G. Vaschenko, C. Brewer, M. Grisham, C. Menoni, M. Marconi, J. Rocca, W. Chao, J. Liddle, E. Anderson, D. Attwood, A. Vinogradov, I. Artioukov, Y. Pershyn, and V. Kondratenko. Reflection mode imaging with nanoscale resolution using a compact extreme ultraviolet laser. *Opt. Express*, 13(11):3983–3988, 2005.
- [4] Courtney A. Brewer, Fernando Brizuela, Przemyslaw Wachulak, Dale H. Martz, Weilun Chao, Erik H. Anderson, David T. Attwood, Alexander V. Vinogradov, Igor A. Artyukov, Alexander G. Ponomareko, Valeriy V. Kondratenko, Mario C. Marconi, Jorge J. Rocca, and Carmen S. Menoni. Single-shot extreme ultraviolet laser imaging of nanostructures with wavelength resolution. *Opt. Lett.*, 33(5):518–520, 2008.

- [5] F. Brizuela, Y. Wang, C. A. Brewer, F. Pedaci, W. Chao, E. H. Anderson, Y. Liu, K. A. Goldberg, P. Naulleau, P. Wachulak, M. C. Marconi, D. T. Attwood, J. J. Rocca, and C. S. Menoni. Microscopy of extreme ultraviolet lithography masks with 13.2 nm tabletop laser illumination. *Opt. Lett.*, 34(3):271–273, 2009.
- [6] G. Vaschenko, C. Brewer, F. Brizuela, Y. Wang, M. A. Larotonda, B. M. Luther, M. C. Marconi, J. J. Rocca, C. S. Menoni, E. H. Anderson, W. Chao, B. D. Harteneck, J. A. Liddle, Y. Liu, and D. T. Attwood. Sub-38 nm resolution tabletop microscopy with 13 nm wavelength laser light. *Opt. Lett.*, 31(9):1214–1216, 2006.
- [7] W. Chao, B. D. Harteneck, J. A. Liddle, E. H. Anderson, and D. T. Attwood. Soft x-ray microscopy at a spatial resolution better than 15 nm. *Nature*, 435:1210–1213, 2005.
- [8] M. Berglund, L. Rymell, M. Peuker, T. Wilhein, and H. M. Hertz. Compact water-window transmission x-ray microscopy. *Journal of Microscopy*, 197:268–273, 2000.
- [9] P. W. Wachulak, M. G. Capeluto, C. S. Menoni, J. J. Rocca, and M. C. Marconi. Nanopatterning in a compact setup using table top extreme ultraviolet lasers. *Opto-Electronics Review*, 16(4):444–450, 2008.

- [10] Przemyslaw W. Wachulak, Lukasz Urbanski, Maria G. Capeluto, David Hill, Willie S. Rockward, Claudio Iemmi, Erik H. Anderson, Carmen S. Menoni, Jorge J. Rocca, and Mario C. Marconi. New opportunities in interferometric lithography using extreme ultraviolet tabletop lasers. *Journal of Micro/Nanolithography, MEMS and MOEMS*, 8(2):021206, 2009.
- [11] A. Isoyan, F. Jiang, Y.-C. Cheng, P. Wachulak, L. Urbanski, J. Rocca, C. Menoni, M. Marconi, and F. Cerrina. Extreme ultraviolet holographic lithography with a table-top laser. volume 7271, page 72713O. SPIE, 2009.
- [12] H. H. Solak. Nanolithography with coherent extreme ultraviolet light. *J. Phys. D: Applied Physics*, 39:R171–R188, 2006.
- [13] F. Dong, S. Heinbuch, J. J. Rocca, and E. R. Bernstein. Dynamics and fragmentation of van der Waals clusters: $(\text{H}_2\text{O})_n$, $(\text{CH}_3\text{OH})_n$, and $(\text{NH}_3)_n$ upon ionization by a 26.5 eV soft x-ray laser. *The Journal of Chemical Physics*, 124(22):224319, 2006.
- [14] F. Dong, S. Heinbuch, S. G. He, Y. Xie, J. J. Rocca, and E. R. Bernstein. Formation and distribution of neutral vanadium, niobium, and tantalum oxide clusters: Single photon ionization at 26.5 eV. *The Journal of Chemical Physics*, 125(16):164318, 2006.
- [15] S. Heinbuch, F. Dong, J. J. Rocca, and E. R. Bernstein. Single photon ionization of hydrogen bonded clusters with a soft x-ray laser: $(\text{HCOOH})_x$

- and $(\text{HCOOH})_y(\text{H}_2\text{O})_z$. *The Journal of Chemical Physics*, 126(24):244301, 2007.
- [16] F. Dong, S. Heinbuch, J. J. Rocca, and E. R. Bernstein. Studies of neutral Al_mC_n clusters employing a table-top soft x-ray laser. volume 7451, page 74510Q. SPIE, 2009.
- [17] Mark E. Siemens, Qing Li, Margaret M. Murnane, Henry C. Kapteyn, Ronggui Yang, Erik H. Anderson, and Keith A. Nelson. High-frequency surface acoustic wave propagation in nanostructures characterized by coherent extreme ultraviolet beams. *Applied Physics Letters*, 94(9):093103, 2009.
- [18] L. Miaja-Avila, J. Yin, S. Backus, G. Saathoff, M. Aeschlimann, M. M. Murnane, and H. C. Kapteyn. Ultrafast studies of electronic processes at surfaces using the laser-assisted photoelectric effect with long-wavelength dressing light. *Physical Review A (Atomic, Molecular, and Optical Physics)*, 79(3):030901, 2009.
- [19] L. Miaja-Avila, C. Lei, M. Aeschlimann, J. L. Gland, M. M. Murnane, H. C. Kapteyn, and G. Saathoff. Laser-assisted photoelectric effect from surfaces. *Physical Review Letters*, 97(11):113604, 2006.
- [20] J. J. Rocca, E. C. Hammarsten, E. Jankowska, J. Filevich, M. C. Marconi, S. Moon, and V. N. Shlyaptsev. Application of extremely compact capil-

lary discharge soft x-ray laser to dense plasma diagnostics. *Phys. Plasmas*, 10(5):2031–2038, 2003.

[21] Jorge Filevich, Jorge J. Rocca, Mario C. Marconi, Raymond F. Smith, James Dunn, Roisin Keenan, James R. Hunter, Stephen J. Moon, Joseph Nilsen, Andrew Ng, and Vyacheslav N. Shlyaptsev. Picosecond-resolution soft-x-ray laser plasma interferometry. *Appl. Opt.*, 43(19):3938–3946, 2004.

[22] J. Filevich, J. J. Rocca, M. C. Marconi, S. J. Moon, J. Nilsen, J. H. Scofield, J. Dunn, R. F. Smith, R. Keenan, J. R. Hunter, and V. N. Shlyaptsev. Observation of a multiply ionized plasma with index of refraction greater than one. *Phys. Rev. Lett.*, 94(3):035005, Jan 2005.

[23] Jorge Filevich, Jonathan Grava, Mike Purvis, Mario C. Marconi, Jorge J. Rocca, Joseph Nilsen, James Dunn, and Walter R. Johnson. Prediction and observation of tin and silver plasmas with index of refraction greater than one in the soft x-ray range. *Physical Review E (Statistical, Nonlinear, and Soft Matter Physics)*, 74(1):016404, 2006.

[24] T. Maiman. Stimulated optical radiation in ruby. *Nature*, 187:493–494, 1960.

[25] M. Berrill. A computer model to simulate laser created plasmas used for the generation of extreme ultraviolet lasers. Master’s thesis, Colorado State University, 2006.

- [26] R. M. More. *Atomic physics of laser-produced plasmas*. North-Holland, 1991.
- [27] W. H. Goldstein, A. Zigler, P. G. Burkhalter, D. J. Nagel, A. Bar-Shalom, J. Oreg, T. S. Luk, A. McPherson, and C. K. Rhodes. X-ray emission from a 650-fs laser-produced barium plasma. *Phys. Rev. E*, 47(6):4349–4353, Jun 1993.
- [28] C. W. Allen. *Astrophysical Quantities*. Oxford University Press, 1963.
- [29] A. E. Siegman. *Lasers*. Springer, 1990.
- [30] Gary J. Linford, Eugene R. Peressini, Walter R. Sooy, and Mary L. Spaeth. Very long lasers. *Appl. Opt.*, 13(2):379–390, 1974.
- [31] Riccardo Tommasini and Ernst E. Fill. Generalized Linford formula. *J. Opt. Soc. Am. B*, 17(10):1665–1670, 2000.
- [32] Richard A. London. Beam optics of exploding foil plasma x-ray lasers. *Physics of Fluids*, 31(1):184–192, 1988.
- [33] J. D. Jackson. *Classical Electrodynamics, Third Edition*. John Wiley & Sons Inc., 1999.
- [34] William T. Silfvast, John J. Macklin, and Obert R. Wood II. High-gain inner-shell photoionization laser in Cd vapor pumped by soft-x-ray radiation from a laser-produced plasma source. *Opt. Lett.*, 8(11):551–553, 1983.

- [35] H. C. Kapteyn, R. W. Lee, and R. W. Falcone. Observation of a short-wavelength laser pumped by Auger decay. *Phys. Rev. Lett.*, 57(23):2939–2942, Dec 1986.
- [36] H. C. Kapteyn and R. W. Falcone. Auger-pumped short-wavelength lasers in xenon and krypton. *Phys. Rev. A*, 37(6):2033–2038, Mar 1988.
- [37] D. J. Walker, C. P. J. Barty, G. Y. Yin, J. F. Young, and S. E. Harris. Observation of super Coster–Kronig-pumped gain in Zn III. *Opt. Lett.*, 12(11):894–896, 1987.
- [38] S. J. Stephanakis, J. P. Apruzese, P. G. Burkhalter, G. Cooperstein, J. Davis, D. D. Hinshelwood, G. Mehlman, D. Mosher, P. F. Ottinger, V. E. Scherrer, J. W. Thornhill, B. L. Welch, and F. C. Young. Development of a sodium-pump/neon laser photopumped soft x-ray laser. *IEEE Trans. Plasma Sci.*, 16:472–481, 1988.
- [39] C. Deeney, T. Nash, R. R. Prasad, L. Warren, and J. P. Apruzese. K-shell x-ray emission from sodium wire array implosions as the pump for the sodium-neon x-ray laser scheme. *Appl. Phys. Lett.*, 58:1021–1023, 1991.
- [40] J. L. Porter, R. B. Spielman, M. K. Matzen, E. J. McGuire, L. E. Ruggles, M. F. Vargas, J. P. Apruzese, R. W. Clark, and J. Davis. Demonstration of population inversion by resonant photopumping in a neon gas cell irradiated by a sodium Z pinch. *Phys. Rev. Lett.*, 68(6):796–799, Feb 1992.

- [41] E. E. Fill, C. Bergmann, A. Lyras, and T. Schlegel. Photo-pumped gain in lithium-like magnesium. In E. E. Fill, editor, *X-Ray Lasers 1992, Proceedings of the 3rd Int. Colloquium on X-ray Lasers*, pages 147–150, 1992.
- [42] K. J. Ilcsin, F. Aumayr, J. L Schwob, and S. Suckewer. Demonstration of resonant fluorescence in Mo VII induced by Mo XII for possible lasing near 600 Å. *J. Opt. Soc. Am. B*, 58:1436–1444, 1991.
- [43] N. Qi, D. A. Hammer, D. H. Kalantar, and K. C. Mittal. Fluorescence in Mg IX emission at 48.340 Å from Mg pinch plasmas photopumped by Al XI line radiation at 48.338 Å. *Phys. Rev. A*, 47(3):2253–2263, Mar 1993.
- [44] S. Suckewer, C. H. Skinner, H. Milchberg, C. Keane, and D. Voorhees. Amplification of stimulated soft-x-ray emission in a confined plasma column. *Phys. Rev. Lett.*, 55:1753–1756, Oct 1985.
- [45] Y. Nagata, K. Midorikawa, S. Kubodera, M. Obara, H. Tashiro, and K. Toyoda. Soft-x-ray amplification of the Lyman- α transition by optical-field-induced ionization. *Phys. Rev. Lett.*, 71:3774–3777, 1993.
- [46] D. V. Korobkin, C. H. Nam, and S. Suckewer. Demonstration of soft-x-ray lasing to ground state in Li III. *Phys. Rev. Lett.*, 77:5206–5209, 1996.

- [47] A. N. Zherikhin, K. N. Koshelev, and V. S. Letokhov. Gain in the far vacuum ultraviolet region due to transitions in multiply charged ions. *Soviet Journal of Quantum Electronics*, 6(1):82–84, 1976.
- [48] A. V. Vinogradov and V. N. Shlyaptsev. Calculations of population inversion due to transitions in multiply charged neon-like ions in the 200-2000 Å range. *Soviet Journal of Quantum Electronics*, 10(6):754–756, 1980.
- [49] J. J. Rocca. Table-top soft x-ray lasers. *Rev. of Sci. Inst.*, 70:3799–3827, 1999.
- [50] D. L. Matthews, P. L. Hagelstein, M. D. Rosen, M. J. Eckart, N. M. Ceglio, A. U. Hazi, H. Medeck, B. J. MacGowan, J. E. Trebes, B. L. Whitten, E. M. Campbell, C. W. Hatcher, A. M. Hawryluk, R. L. Kauffman, L. D. Pleasance, G. Rambach, J. H. Scofield, G. Stone, and T. A. Weaver. Demonstration of a soft x-ray amplifier. *Phys. Rev. Lett.*, 54(2):110–113, Jan 1985.
- [51] T. N. Lee, E. A. McLean, and R. C. Elton. Soft x-ray lasing in neonlike germanium and copper plasmas. *Phys. Rev. Lett.*, 59(11):1185–1188, Sep 1987.
- [52] D. J. Fields, R. S. Walling, G. M. Shimkaveg, B. J. MacGowan, L. B. Da Silva, J. H. Scofield, A. L. Osterheld, T. W. Phillips, M. D. Rosen, D. L. Matthews, W. H. Goldstein, and R. E. Stewart. Observation of high gain in Ne-like Ag lasers. *Phys. Rev. A*, 46(3):1606–1609, Aug 1992.

- [53] A. Carillon, H. Z. Chen, P. Dhez, L. Dwivedi, J. Jacoby, P. Jaeglé, G. Jamelot, Jie Zhang, M. H. Key, A. Kidd, A. Klisnick, R. Kodama, J. Krishnan, C. L. s. Lewis, D. Neely, P. Norreys, D. O'Neill, G. J. Pert, S. A. Ramsden, J. P. Raucourt, G. J. Tallents, and J. Uhomoibhi. Saturated and near-diffraction-limited operation of an XUV laser at 23.6 nm. *Phys. Rev. Lett.*, 68(19):2917–2920, May 1992.
- [54] S. Maxon, P. Hagelstein, J. Scofield, and Y. Lee. Estimated gains for a Ni-like exploding foil target. *Journal of Applied Physics*, 59(1):293–295, 1986.
- [55] S. Maxon, P. Hagelstein, K. Reed, and J. Scofield. A gas puff soft x-ray laser target design. *Journal of Applied Physics*, 57(3):971–972, 1985.
- [56] Peter L. Hagelstein. Relativistic distorted-wave results for nickel-like gadolinium. *Phys. Rev. A*, 34(2):874–884, 1986.
- [57] B. J. MacGowan, S. Maxon, P. L. Hagelstein, C. J. Keane, R. A. London, D. L. Matthews, M. D. Rosen, J. H. Scofield, and D. A. Whelan. Demonstration of soft-x-ray amplification in nickel-like ions. *Phys. Rev. Lett.*, 59(19):2157–2160, 1987.
- [58] B. J. MacGowan, S. Maxon, L. B Da Silva, C. J. Keane D.J. Fields, D. L. Matthews, A. L. Osterheld, J. H. Scofield, G. Shimkaveg, and G. F. Stone. Demonstration of x-ray amplifiers near the Carbon K-edge. *Phys. Rev. Lett.*, 65(4):420–423, 1990.

- [59] B. J. MacGowan, L. B. DaSilva, D. J. Fields, C. J. Keane, J. A. Koch, R. A. London, D. L. Matthews, S. Maxon, Mrowka S, A. L. Osterheld, J. H. Scofield, G. Shimkaveg, J. E. Trebes, and R. S. Walling. Short wavelength x-ray laser research at the Lawrence Livermore National Laboratory. *Phys. Fluids B*, 4(7):2326–2337, 1992.
- [60] Pierre Jaeglé. *Coherent sources of XUV radiation*. Springer, 2006.
- [61] Joseph Nilsen, Brian J. MacGowan, Luiz B. Da Silva, and Juan C. Moreno. Prepulse technique for producing low-Z Ne-like x-ray lasers. *Phys. Rev. A*, 48(6):4682–4685, Dec 1993.
- [62] Joseph Nilsen and Juan C. Moreno. Nearly monochromatic lasing at 182 Å in neonlike selenium. *Phys. Rev. Lett.*, 74(17):3376–3379, Apr 1995.
- [63] Yuelin Li, Georg Pretzler, and Ernst E. Fill. Ne-like ion lasers in the extreme ultraviolet region. *Phys. Rev. A*, 52(5):R3433–R3435, Nov 1995.
- [64] J. Zhang, P. J. Warwick, E. Wolfrum, M. H. Key, C. Danson, A. Demir, S. Healy, D. H. Kalantar, N. S. Kim, C. L. S. Lewis, J. Lin, A. G. MacPhee, D. Neely, J. Nilsen, G. J. Pert, R. Smith, G. J. Tallents, and J. S. Wark. Saturated output of a GeXXIII x-ray laser at 19.6 nm. *Phys. Rev. A*, 54(6):R4653–R4656, Dec 1996.

- [65] P. Jaeglé, A. Carillon, P. Dhez, P. Goedkindt, G. Jamelot, A. Klisnick, B. Rus, P. Zeitoun, S. Jacquemot, D. Mazataud, A. Mens, and C. Chauvineau. In D. C. Elder and D. L. Matthews, editors, *X-Ray Lasers 1994, Fourth International Colloquium*, page 25, 1994.
- [66] H. Daido, Y. Kato, K. Murai, S. Ninomiya, R. Kodama, G. Yuan, Y. Os hikane, M. Takagi, H. Takabe, and F. Koike. Efficient soft x-ray lasing at 6 to 8 nm with nickel-like lanthanide ions. *Phys. Rev. Lett.*, 75(6):1074–1077, Aug 1995.
- [67] Joseph Nilsen and Juan C. Moreno. Lasing at 7.9 nm in nickellike neodymium. *Opt. Lett.*, 20(12):1386–1388, 1995.
- [68] Yuelin Li, Georg Pretzler, Peixiang Lu, and Ernst E. Fill. Demonstration of x-ray lasing in nickel-like tin. *Phys. Rev. A*, 53(2):R652–R654, Feb 1996.
- [69] J. Zhang, A. G. MacPhee, J. Lin, E. Wolfrum, R. Smith, C. Danson, M. H. Key, C. L. S. Lewis, D. Neely, J. Nilsen, G. J. Pert, G. J. Tallents, and J. S. Wark. A Saturated X-ray Laser Beam at 7 nm. *Science*, 276(5315):1097–1100, 1997.
- [70] Y. V Afanas'ev and V. N. Shlyaptsev. Formation of a population inversion of transitions in Ne-like ions in steady-state and transient plasmas. *Sov. J. Quantum Electron*, 19(12):1606–1612, 1989.

- [71] P. V. Nickles, V. N. Shlyaptsev, M. Kalachnikov, M. Schnürer, I. Will, and W. Sandner. Short pulse x-ray laser at 32.6 nm based on transient gain in Ne-like titanium. *Phys. Rev. Lett.*, 78(14):2748–2751, Apr 1997.
- [72] D. Strickland and G. Mourou. Compression of amplified chirped optical pulses. *Optics Communications*, 55:447–449, 1985.
- [73] O. Martinez. Design of high-power ultrashort pulse amplifiers by expansion and recompression. *Quantum Electronics, IEEE Journal of*, 23(8):1385–1387, Aug 1987.
- [74] J. R. Crespo Lopez-Urrutia and E. E. Fill. Traveling wave excitation of an x-ray laser medium. In S. Suckewer, editor, *Ultrashort Wavelength Lasers II, Proc, SPIE 2012*, pages 258–264, 1993.
- [75] Z. Bor, S. Szatmri, and A. Müller. Picosecond pulse shortening by traveling wave amplified spontaneous emission. *Appl. Phys. B*, 32:101–104, 1983.
- [76] M. P. Kalachnikov, P. V. Nickles, M. Schnürer, W. Sandner, V. N. Shlyaptsev, C. Danson, D. Neely, E. Wolfrum, J. Zhang, A. Behjat, A. Demir, G. J. Tallents, P. J. Warwick, and C. L. S. Lewis. Saturated operation of a transient collisional x-ray laser. *Phys. Rev. A*, 57(6):4778–4783, Jun 1998.
- [77] P. J. Warwick, C. L. S. Lewis, M. P. Kalachnikov, P. V. Nickles, M. Schnürer, A. Behjat, A. Demir, G. J. Tallents, D. Neely, E. Wolfrum, J. Zhang, and

- G. J. Pert. Observation of high transient gain in the germanium x-ray laser at 19.6 nm. *J. Opt. Soc. Am. B*, 15(6):1808–1814, 1998.
- [78] J. Dunn, Y. Li, A. L. Osterheld, J. Nilsen, J. R. Hunter, and V. N. Shlyaptsev. Gain saturation regime for laser-driven tabletop, transient Ni-like ion x-ray lasers. *Phys. Rev. Lett.*, 84(21):4834–4837, May 2000.
- [79] T. Ozaki, R. A. Ganeev, A. Ishizawa, T. Kanai, and H. Kuroda. Highly directive 18.9 nm nickel-like molybdenum x-ray laser operating at 150 mJ pump energy. *Phys. Rev. Lett.*, 89(25):253902, Nov 2002.
- [80] R. Li and Z. Z. Xu. Highly efficient transient collisional excitation x-ray laser in Ni-like Mo ions. In G. Jamelot, C. Müller, and A. Klishnick, editors, *X-Ray Lasers 2001, Proceedings of the 7th International Conference*, pages 27–34, 2001.
- [81] R. Tommasini, J. Nilsen, and E. E. Fill. Investigations on 10-Hz sub-Joule fs-laser pumped neon- and nickel-like x-ray lasers. In *Proc. SPIE, Soft x-ray lasers and applications IV*, pages 85–92, 2001.
- [82] V. N. Shlyaptsev, James Dunn, S. Moon, R. Smith, Roisin Keenan, Joseph Nilsen, Kevin B. Fournier, Jaroslav Kuba, A. L. Osterheld, J. J. G. Rocca, Bradley M. Luther, Yong Wang, and Mario C. Marconi. Numerical studies of transient and capillary x-ray lasers and their applications. volume 5197, pages 221–228. SPIE, 2003.

- [83] Roisin Keenan, James Dunn, Vyacheslav N. Shlyaptsev, Raymond F. Smith, Pravesh K. Patel, and Dwight F. Price. Efficient pumping schemes for high average brightness collisional x-ray lasers. volume 5197, pages 213–220. SPIE, 2003.
- [84] R. Keenan, J. Dunn, P. K. Patel, D. F. Price, R. F. Smith, and V. N. Shlyaptsev. High-repetition-rate grazing-incidence pumped x-ray laser operating at 18.9 nm. *Phys. Rev. Lett.*, 94(10):103901, Mar 2005.
- [85] B. M. Luther, Y. Wang, M. A. Larotonda, D. Alessi, M. Berrill, M. C. Marconi, J. J. Rocca, and V. N. Shlyaptsev. Saturated high-repetition-rate 18.9-nm tabletop laser in nickellike molybdenum. *Opt. Lett.*, 30(2):165–167, 2005.
- [86] M. A. Larotonda, B. M. Luther, Y. Wang, Y. Liu, D. Alessi, M. Berrill, A. Dummer, F. Brizuela, C. S. Menoni, M. C. Marconi, V. N. Shlyaptsev, J. Dunn, and J. J. Rocca. Characteristics of a saturated 18.9 nm tabletop laser operating at 5-Hz repetition rate. *IEEE J. Sel. Topics Quantum Electron.*, 10(6):1363–1367, 2004.
- [87] J. J. Rocca, Y. Wang, M. A. Larotonda, B. M. Luther, M. Berrill, and D. Alessi. Saturated 13.2 nm high-repetition-rate laser in nickellike cadmium. *Opt. Lett.*, 30(19):2581–2583, 2005.

- [88] Y. Wang, M. A. Larotonda, B. M. Luther, D. Alessi, M. Berrill, V. N. Shlyaptsev, and J. J. Rocca. Demonstration of high-repetition-rate tabletop soft-x-ray lasers with saturated output at wavelengths down to 13.9 nm and gain down to 10.9 nm. *Phys. Rev. A*, 72(5):053807, Nov 2005.
- [89] D. Alessi, B. Luther, Y. Wang, M. Larotonda, M. Berrill, and J. Rocca. High repetition rate operation of saturated tabletop soft x-ray lasers in transitions of neon-like ions near 30 nm. *Opt. Express*, 13(6):2093–2098, 2005.
- [90] B. M. Luther, Y. Wang, M. A. Larotonda, D. Alessi, M. Berrill, J. J. Rocca, J. Dunn, R. Keenan, and V. N. Shlyaptsev. High repetition rate collisional soft x-ray lasers based on grazing incidence pumping. *IEEE J. of Quantum Electron.*, 42(1):4–12, 2006.
- [91] A. Weith, M. A. Larotonda, Y. Wang, B. M. Luther, D. Alessi, M. C. Marconi, J. J. Rocca, and J. Dunn. Continuous high-repetition-rate operation of collisional soft-x-ray lasers with solid targets. *Opt. Lett.*, 31(13):1994–1996, 2006.
- [92] M. A. Larotonda, Y. Wang, M. Berrill, B. M. Luther, J. J. Rocca, Mahendra Man Shakya, S. Gilbertson, and Zenghu Chang. Pulse duration measurements of grazing-incidence-pumped high repetition rate Ni-like Ag and Cd transient soft x-ray lasers. *Opt. Lett.*, 31(20):3043–3045, 2006.

- [93] Y. Liu, Y. Wang, M. A. Larotonda, B. M. Luther, J. J. Rocca, and D. T. Attwood. Spatial coherence measurements of a 13.2 nm transient nickel-like cadmium soft x-ray laser pumped at grazing incidence. *Opt. Express*, 14(26):12872–12879, 2006.
- [94] M. Berrill, Y. Wang, M. A. Larotonda, B. M. Luther, V. N. Shlyaptsev, and J. J. Rocca. Pump pulse-width dependence of grazing-incidence pumped transient collisional soft-x-ray lasers. *Physical Review A (Atomic, Molecular, and Optical Physics)*, 75(6):063821, 2007.
- [95] Y. Wang, E. Granados, F. Pedaci, D. Alessi, B. Luther, M. Berrill, and J. J. Rocca. Phase-injection, injection-seeded, table-top soft-x-ray lasers at 18.9 nm and 13.9 nm. *Nature Photonics*, 2:94–98, 2008.
- [96] Y. Wang, E. Granados, M. A. Larotonda, M. Berrill, B. M. Luther, D. Patel, C. S. Menoni, and J. J. Rocca. High-brightness injection-seeded soft-x-ray-laser amplifier using a solid target. *Physical Review Letters*, 97(12):123901, 2006.
- [97] J. Tümmler, K. A. Janulewicz, G. Priebe, and P. V. Nickles. 10-Hz grazing incidence pumped Ni-like Mo x-ray laser. *Phys. Rev. E*, 72(3):037401, Sep 2005.
- [98] H. T. Kim, I. W. Choi, N. Hafz, J. H. Sung, T. J. Yu, K.-H. Hong, T. M. Jeong, Y.-C. Noh, D.-K. Ko, K. A. Janulewicz, J. Tümmler, P. V. Nickles,

- W. Sandner, and J. Lee. Demonstration of a saturated Ni-like Ag x-ray laser pumped by a single profiled laser pulse from a 10-Hz Ti:sapphire laser system. *Physical Review A (Atomic, Molecular, and Optical Physics)*, 77(2):023807, 2008.
- [99] A. Klisnick, D. Ros, G. Jamelot, S. Kazamias, M. Pitmann, K. Cassou, F. Plé, O. Guilbaud, I. R. Al'Miev, C. Möller, D. Benredjem, J. Dubau, D. Joyeux, C. G. Wahlström, T. Kühn, B. Rus, H. Bercegol, O. Larroche, J. P. Chambaret, P. Zeitoun, and P. Velarde. Recent progress in x-ray laser development and applications at LIXAM. In P. V. Nickles and K. A. Janulewicz, editors, *X-Ray Lasers 2006, Proceedings of the 10th International Conference*, pages 13–22, 2006.
- [100] J. E. Balmer, M. Grünig, C. Imesch, and F. Staub. X-ray lasing using the GRIP scheme. In P. V. Nickles and K. A. Janulewicz, editors, *X-Ray Lasers 2006, Proceedings of the 10th International Conference*, pages 37–43, 2006.
- [101] E. Treacy. Optical pulse compression with diffraction gratings. *IEEE Journal of Quantum Electronics*, 5:454–458, sep 1969.
- [102] Michael Perry. Multilayer dielectric gratings. *Science and Technology Review*, pages 24–33, 1995.
- [103] John R. Oliver and Frank S. Barnes. A comparison of rare-gas flashlamps. *IEEE Journal of Quantum Electronics*, QE-5(5):232–237, 1969.

- [104] Raphael Lavi, S. Jackel, Y. Tzuk, E. Lebiush, M. Winik, I. Paiss, and T. Arusi-Parpar. Enhanced performance of Nd:YAG by direct pumping from thermally excited ground state levels directly to the upper lasing level. In *Advanced Solid State Lasers*, page ME14. Optical Society of America, 2000.

Chapter 2

**DESCRIPTION AND PERFORMANCE OF
THE CPA LASER SYSTEM**

In chapter 1 a comprehensive review of laser driven transient collisional soft x-ray lasers was presented. The required plasma geometry and dynamics were discussed as well as the way to generate such a plasma using a combination of two or more very intense pulses from an optical laser driver. It was pointed out also that the state of the art of the driver lasers consists of flash lamp pumped chirped pulse amplification systems delivering sub-10 ps pulses with energies ranging from 1 J to ~ 10 J at repetition rates of 0.1 - 10 Hz. It was also brought to attention that the intrinsic thermal problems of flash lamp pumping is setting a limit to the repetition rate of the driver lasers and hence, to the repetition rate of soft x-ray lasers.

In this chapter the advantages of diode-pumping and cryogenic cooling for high average power laser systems are presented as well as the general characteristics of the all diode-pumped laser system developed for pumping soft x-ray lasers.

2.1 Diode-pumped chirped pulse amplification systems

To overcome the limitations of flash lamp pumped systems, we undertook a project to develop a compact infrared chirped pulse amplification (CPA) laser system, solely pumped by laser diodes with the goal of generating very intense pulses at repetition rates reaching 50-100 Hz. These laser pulses were used to create a plasma column with the appropriate geometry and dynamics discussed in chapter 1 to produce amplification of spontaneous emission within the plasma column.

The potential of direct diode-pumping for high repetition rate, high energy laser systems was briefly mentioned at the end of chapter 1 and will be explored in more detail now.

2.1.1 Advantages of direct diode-pumping

The advances in semiconductor lasers has turned direct diode-pumping of solid state lasers into a very attractive option for high energy CPA systems. The widespread use of laser diodes in many scientific and industrial applications has also allowed a reduction in the cost of these devices. High power laser diodes in particular, have become commercially available at several wavelengths, and in several different packages. It is possible for instance to find 2 kW laser diode stacks in a fiber coupled package or 4.5 kW stacks in a very compact vertical array of 72 mm by 10 mm (see fig. 2.1). Even the non fiber-coupled arrangements have a reasonably good beam quality to be used as pump sources in end-pumping systems. For instance, the laser diode stack in fig. 2.1 is formed by 45 arrays of 10 emitters each, delivering 100 W per array. Each array has a cylindrical microlens to collimate the fast axis of the emitters. The net result is that the output beam has a vertical divergence of less than 1 degree and a horizontal (slow axis of the emitters) full angle divergence of ~ 12.5 degrees.

Laser diodes are very efficient reaching typically electrical to optical efficiencies higher than 50 %. This is extremely attractive for high power applications since



Figure 2.1: Picture of a 4.5 kW InGaAs laser diode stack emitting at 940 nm commercially available from Coherent.

it means that a relatively compact cooling system will take care of heat removal. Again referring to the 4.5 kW stack of fig. 2.1, each array is cooled by water flowing through a set of microchannels. A 10 kW chiller of $\sim 1 \text{ m}^3$ running with deionized water is more than sufficient to cool down the system.

The main advantage of laser diodes as pump sources for high average power solid state lasers is the narrow spectral bandwidth. High power laser diodes present typical emission bandwidths of $\sim 3\text{-}5 \text{ nm}$. This is the key element that makes laser diode pumping preferable over flash lamp pumping for a high repetition rate, and hence high average power laser system. Pumping with a narrow bandwidth source of the optimum wavelength allows to pump directly the upper laser level or a level right above it, coupled to this through non-radiative transitions. In any case, the

net effect is that most of the pump energy ends up populating the laser upper level and therefore a large fraction of the energy can be extracted as laser light. On top of that, it is worth mentioning here that typical laser materials used in diode-pumped systems (such as Yb-doped materials) present a very high quantum efficiency or very low quantum defect. For example, the quantum defect in Yb:YAG pumped at 941 nm and emitting at 1030 nm is $\sim 9\%$, while in Yb:KYW it is $\sim 4\%$ (981 nm and 1025 nm). On the other hand, the quantum defect for Ti:Sapphire is $\sim 33\%$. Therefore, when pumping a small quantum defect material with a narrow bandwidth source such as a laser diode, the amount of heat dissipated in the laser material is minimized and so are the thermal effects such as thermal lensing and thermally induced depolarization that eventually limit the scaling up in repetition rate.

2.1.2 Yb-doped gain materials

Many Yb-doped materials have been proposed as gain material for high power amplifiers including Yb:YAG, Yb:YLF, Yb:S-FAP, Yb:GdCOB, Yb:KYW among others [1–8]. These materials share similar characteristics like the long upper level lifetime, the possibility of being pumped by laser diodes or the high quantum efficiency. However there are some differences that make one or another material more suitable for a particular application. From the Yb-doped materials the most

extensively used in diode-pumped systems to date is Yb:YAG. Table 2.1 shows a comparison between many Yb-doped materials used in high power amplifiers.

Host	λ_{abs} (nm)	λ_{em} (nm)	$\Delta\lambda_{em}$ (nm)	σ_{em} (10^{-20}cm^2)	κ ($\frac{W}{mK}$)	τ (ms)
YAG	941	1030	12	2.03	13	0.95
S-FAP	899	1047	4	7.3	2.0	1.14
YLF	960	1018	47	0.75	4.3	2
GdCOB	900	1030	44	0.35	2.4	2.3
KYW	981	1025	16	3.0	3.3	0.6
KGW	981	1023	20	2.8	3.3	0.6

Table 2.1: Comparison between some Yb-doped laser materials (from ref. [1–8])

All of these materials present a high quantum efficiency ($> 86\%$) and have absorption bands around 900-1000 nm. The emission wavelength for all of them is right above 1000 nm and the lifetime of the upper laser level is in the order of 1-2 ms. This is important for diode-pumping since laser diodes cannot provide high peak power and pulsed pumping is done running the diodes in quasi-cw mode, in other words, modulating the output of the diodes in time. From all the materials in table 2.1 Yb:YAG is the most attractive for a high energy, high repetition rate chirped pulse amplification laser system. First of all, the absorption band at 941 nm is suitable for pumping with commercially available high power laser diodes. The high emission cross section allows for the design of high gain, efficient amplifiers while providing at the same time a relatively broad bandwidth, which can support sub-ps pulses. In addition the thermal conductivity of YAG is much higher

than that of any other Yb-doped laser material and this characteristic makes it really attractive for high average power amplifiers. One of the most important characteristics of Yb:YAG is not represented in this table however, and this is the fact that crystal growing techniques are very mature for Yb:YAG and it is possible to get in the market large crystals, in a variety of shapes and dopings, with very high quality.

2.1.3 General characteristics of Yb:YAG

Yb:YAG is the acronym for Yttrium Aluminum Garnet ($Y_3Al_5O_{12}$) when doped with Ytterbium ionized three times (Yb^{3+}). The crystalline structure of the host (YAG) is cubic and therefore the material is not birefringent. The Yb^{3+} ion has a very simple 2-manifold energy level structure: the pump and laser transitions take place between sub-levels of the $^2F_{5/2}$ level and the $^2F_{7/2}$ level. In fig. 2.2 the 2-manifold structure of Yb:YAG is illustrated. When pumped at 941 nm the quantum defect is only 9 %, since the emission spectrum is centered at 1030 nm. At room temperature the bandwidth of the absorption band is 18.3 nm, which is sufficiently broad to be efficiently pumped by high power laser diodes.

In all Yb-doped materials the spectral properties are strongly influenced by the host material [9] since each level in the 2-manifold structure splits due to Stark effect produced by the electric field of the ions in the host. Yb:YAG is not an exception and even though the dopage level can go as high as 100 %, the

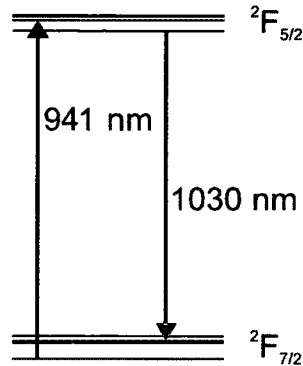


Figure 2.2: Energy level structure of Yb:YAG

characteristics of the laser material change with doping concentration since the electric field producing the Stark splitting is modified. For instance, fig. 2.3 shows measurements of the absorption cross section and the lifetime of the upper laser level changing with Yb concentration [2]

A drawback of the 2-manifold structure in Yb:YAG is the fact that the laser lower level and the ground state belong to the same manifold and, at room temperature, the lower laser level gets populated through thermal excitation. For example, for a temperature of 300 K, the population in the lower laser level due to thermal excitation from the ground state is according to Maxwell-Boltzmann statistics 5.3 % of the population in the ground state. Yb:YAG at room temperature is then a quasi-three level system. This means that a minimum level of pump power is needed to bleach the absorption of the laser wavelength produced by the fact that the lower laser level is populated.

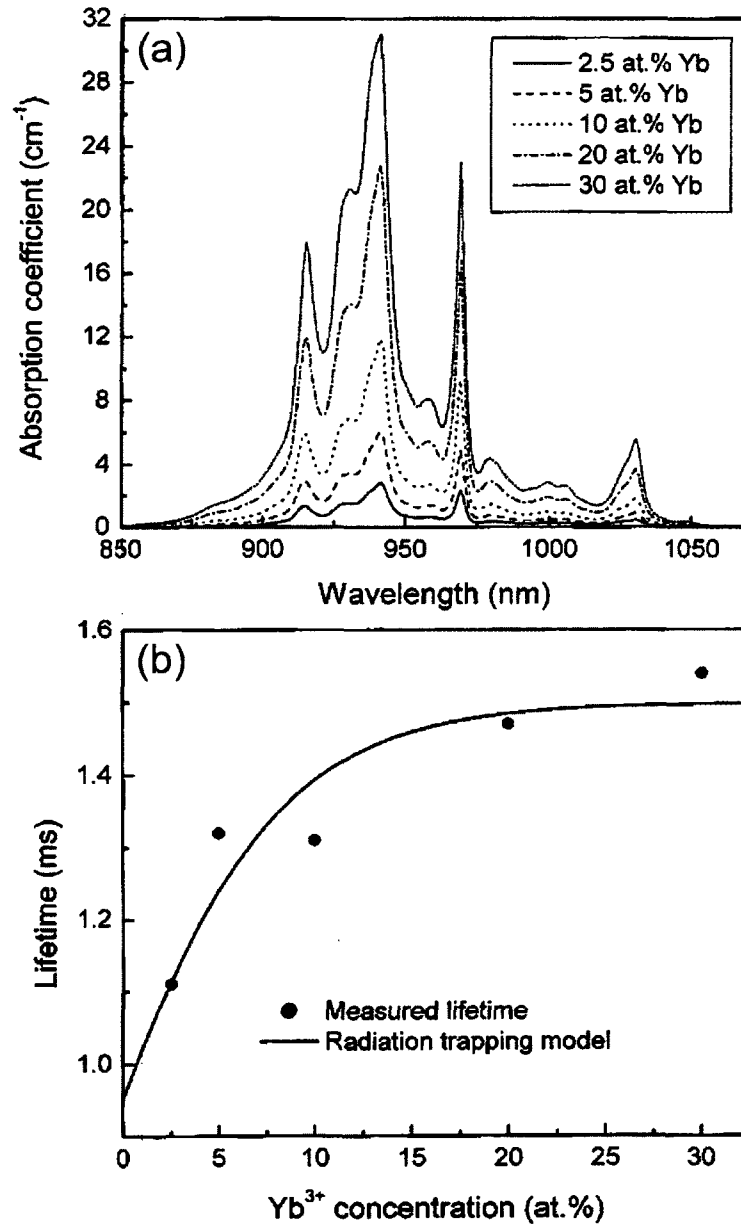


Figure 2.3: (a) Absorption coefficient as a function of wavelength for different concentration of the Yb^{3+} ion. (b) Upper level lifetime as a function of the Yb concentration (from ref. [2])

2.1.4 Cryogenically cooled Yb:YAG

Cryogenically cooled Yb:YAG is our choice for the gain material in the amplifiers of the chirped pulse amplification system. In this section the characteristics of cryo-cooled Yb:YAG will be reviewed pointing out the advantages over room temperature Yb:YAG for a high repetition rate system intended to pump soft x-ray lasers.

Cryogenic cooling of laser materials was proposed as a method to improve the thermal performance of lasers as early as in the 1960s in two patents by Bownes (filed in 1963) and McMahon (filed in 1969) [10, 11]. The advantages of cryogenic cooling in laser systems were demonstrated in Ti:Sapphire in several different works during the 1990s [12–15].

In the case of Yb:YAG cryogenic cooling presents several advantages over room temperature operation for high average power laser systems. All the thermal properties are improved almost an order of magnitude when cooling the material to liquid nitrogen temperature at 77 K. The thermo-optic coefficient (derivative of the index of refraction with respect to the temperature), which is crucial in thermal lensing formation is reduced by approximately a factor of 12, the coefficient of thermal expansion is reduced by a factor of 4, and the thermal conductivity is approximately 7 times higher at 77 K [16–21].

The nonlinear thermal distortions in a YAG amplifier have been theoretically studied by Brown [19] in the case of a YAG rod. In this geometry in which the

pump beam and then the heat source are in the axis of the cylinder and where the cooling is provided from the cylindrical faces of the rod, the heat flow and therefore the thermal gradient are radial. In the case of a constant thermal conductivity the radial thermal gradient is given by:

$$\frac{dT(r)}{dr} = -\frac{Q_0 r}{2\kappa} \quad (2.1)$$

where T is the temperature Q_0 is the heat density and κ the thermal conductivity. If the heat density is kept constant and the thermal conductivity is increased a factor of 7, then the temperature gradient is decreased by the same factor. Now, assuming that we can treat κ as constant, the index of refraction is given by:

$$n = n_0 + \Delta n_\alpha + \Delta n_\beta \quad (2.2)$$

where Δn_α and Δn_β are the contributions to the temperature dependent index of refraction from stress induced changes (α is the coefficient of thermal expansion) and the thermo-optic coefficient ($\beta = \frac{dn}{dT}$). The term arising from stress-induced changes in the index, which measures the thermally induced birefringence and causes depolarization losses [22], can be neglected for YAG at liquid nitrogen temperature. The term can be explicitly written (in this case) as:

$$\Delta n_\alpha = -\frac{n_0^3}{2} \frac{\alpha Q_0}{\kappa} C r^2 \quad (2.3)$$

where C is a constant given by the elasto-optical coefficients of the material. From equation 2.3 is clear that the stress-induced changes are proportional to the ratio

α/κ and, for YAG at liquid nitrogen temperature this ratio is ~ 28 times smaller than the room temperature case.

The term arising from the thermo-optic coefficient is

$$\Delta n_{\beta} = A - \beta \frac{Q_0}{4\kappa} r^2 \quad (2.4)$$

Here A is a constant that depends on the size of the laser rod, the thermal conductivity and the thermo-optic coefficient. This constant does not contribute to the thermal gradient but introduces an offset in the temperature. The change in the index is linearly reduced with the thermo-optic coefficient, but on top of that, the term varying with the radius in equation 2.4 is also reduced when the thermal conductivity is increased. For YAG the radially varying term is reduced ~ 70 times when the temperature is reduced from 300 K to 77 K [18].

Let's notice here that the changes in the index introduced by the terms exposed in equations 2.3 and 2.4 give as a result a parabolic change of the index of refraction as a function of the radius, or distance from the axis of the laser rod. And this in turn, has a lensing effect over any beam propagating through the rod, parallel to the axis of the rod. Therefore, the thermal lensing effect is dramatically reduced when cryocooling the material.

The phase distortion introduced in a laser beam due to the radial change of the index of refraction can be expressed as:

$$\Delta\varphi(r) = \frac{2\pi}{\lambda} [(n - n_0) + (n_0 - 1)\alpha(T(r) - T(r_0))] \quad (2.5)$$

Again, the distortions in the phase are dramatically reduced when cooling YAG to liquid nitrogen temperature since the thermal gradient and the changes in index of refraction are minimized. Although the analyzed geometry is a very particular example, it is a good illustration of the advantages of cryogenic cooling in Yb:YAG from the point of view of the thermal performance of the laser material.

The superior thermal performance is not the only advantage of cryo-cooling Yb:YAG. It was mentioned that a drawback of the 2-manifold energy level structure of Yb:YAG is the fact that about 5.3 % of the population of the ground state is thermally excited to the lower laser level. When the material is cooled to liquid nitrogen temperature this percentage is reduced to ~ 0.001 % and the material becomes a true 4-level system.

The change in lifetime and the spectral emission properties for different temperatures and Yb concentrations were studied by Dong *et al.* in ref. [2]. Fig. 2.4 shows their measurements of the stimulated emission cross section as a function of temperature for different Yb concentrations, and related to this change, the gain bandwidth as a function of temperature for each case. The stimulated emission cross section increases almost an order of magnitude as the temperature decreases from 300 K to 77 K. This is important for efficient energy extraction in laser amplifiers, since the small signal gain coefficient is proportional to the stimulated emission cross section. Besides, the saturation fluence is reduced by the same factor (it changes from ~ 7.7 J/cm² to ~ 1.7 J/cm²). The saturation fluence is given

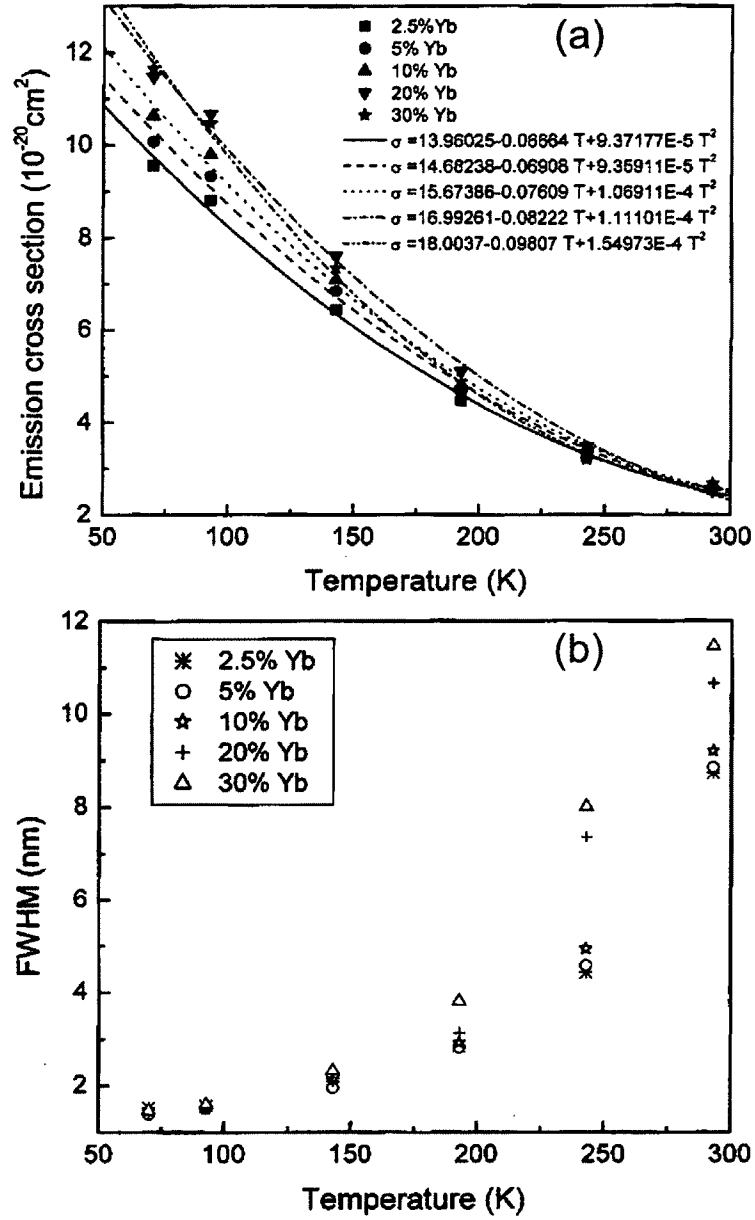


Figure 2.4: (a) Stimulated emission cross section as a function of temperature for different Yb concentrations in Yb:YAG laser crystals (b) Gain bandwidth as a function of temperature and Yb concentration (from ref. [2])

by:

$$F_{sat} = \frac{h\nu}{\sigma_{em}} \quad (2.6)$$

Here h is Planck's constant and ν the frequency of the transition, $h\nu$ being the photon energy of the transition. The saturation fluence is the fluence for which half of the stored energy is removed. Therefore it is desirable to reach the saturation fluence in a laser amplifier to efficiently extract the stored energy. In other words, it is desirable to extract the stored energy in the least number of passes through the gain material. Reducing the number of passes to a minimum is important because on the one hand it minimizes the complexity of the amplifier design and on the other hand, the larger the number of passes the higher the wavefront distortions due to imperfections in the optical components and the cumulative nonlinear phase due to nonlinear interactions between the high energy laser pulse and the optical components of the system. Since the saturation fluence is reduced to $\sim 1.7 \text{ J/cm}^2$ at liquid nitrogen temperature, it is easier to work at the saturation fluence without damaging optical components. This is more challenging at room temperature. For instance, typically the damage threshold of dielectric coatings for pulses of a few hundreds ps is in the order of 10 J/cm^2 ¹.

There is another feature of cryo-cooled Yb:YAG that can be seen from fig. 2.4, and that is the reduced gain bandwidth. This is clearly a disadvantage of cryogenic

¹The case of pulses of hundreds of ps is mentioned because it is a normal duration for amplifying chirped pulses in a CPA laser system

cooling. The reduction in one order of magnitude of the gain bandwidth sets a limit for the shortest pulse that can be generated. In the case of Yb:YAG the gain bandwidth reduces to ~ 1 nm at 77 K. And this is of course, not the bandwidth of the amplified pulses which in addition suffer from further gain narrowing during the amplification process. Nevertheless, the bandwidth is enough to support sub-10 ps pulses, which is necessary for pumping soft x-ray lasers. Moreover, when designing the amplifiers one must remember that the reduction of the bandwidth not only has its detrimental effects when trying to compress the pulses, but even before, since the duration of the stretched pulses is approximately proportional to the bandwidth [23], and therefore the reduction of the gain reduces the duration of the stretched pulses with the danger of producing nonlinear interactions with the optical components of the system and eventually optical damage.

Other properties changing with temperature as studied by Dong *et al.* are the peak wavelength and the lifetime. This is shown in fig. 2.5. The peak wavelength shifts towards the blue as the temperature decreases. The magnitude of this shift is ~ 0.6 nm for different Yb doping levels between 2.5 and 30 %. The upper level lifetime reduces as the temperature decreases. In this case the effect of Yb concentration is very significant. While the lifetime changes from 1.3 ms to 1 ms for a dopage of 2.5 %, a dramatic reduction from 1.5 ms to 0.4 ms is observed for a dopage of 30 %.

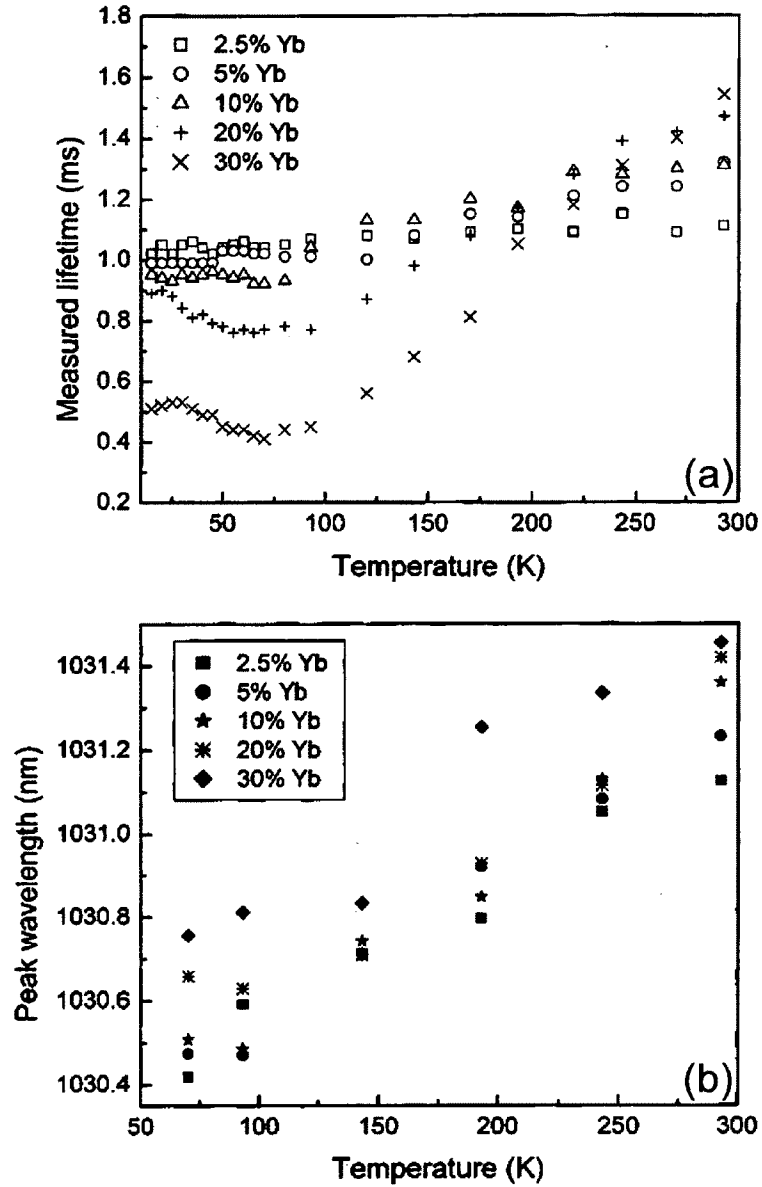


Figure 2.5: (a) Stimulated emission cross section as a function of temperature for different Yb concentrations in Yb:YAG laser crystals (b) Lifetime as a function of temperature and Yb concentration (from ref. [2])

The variation of the absorption cross section as a function of temperature was studied by Brown *et al.* in ref. [24]. Fig. 2.6 illustrates this measurements showing absorption spectra as a function of wavelength at room temperature and liquid nitrogen temperature for a sample with 9 % at. concentration of Yb. The absorption band at ~ 941 nm narrows from 18.3 nm to 12.6 nm while the absorption cross section increases just over a factor of two when the material is cooled to liquid nitrogen temperature. This is still perfectly suitable for pumping with commercially available high power InGaAs laser diodes with emission bandwidth between 3 and 5 nm. The strong absorption line at 969 nm becomes too narrow at 77 K (less than 0.2 nm) and cannot be efficiently pumped with available pump sources.

2.1.5 State of the art on Yb:YAG lasers

With the advances in semiconductor lasers capable of reliable pumping Yb:YAG laser crystals, many Yb:YAG laser systems have been developed in the last few years. Here our interest is centered around CPA systems capable of producing high energy in ps pulses. However it is worth mentioning that Yb:YAG has been successfully employed as gain material also in oscillators and Q-switch amplifiers with nanosecond pulses.

In the case of oscillators it is worth mentioning a cryogenically cooled Yb:YAG continuous wave (cw) laser delivering average powers as high as 273 W [25], another

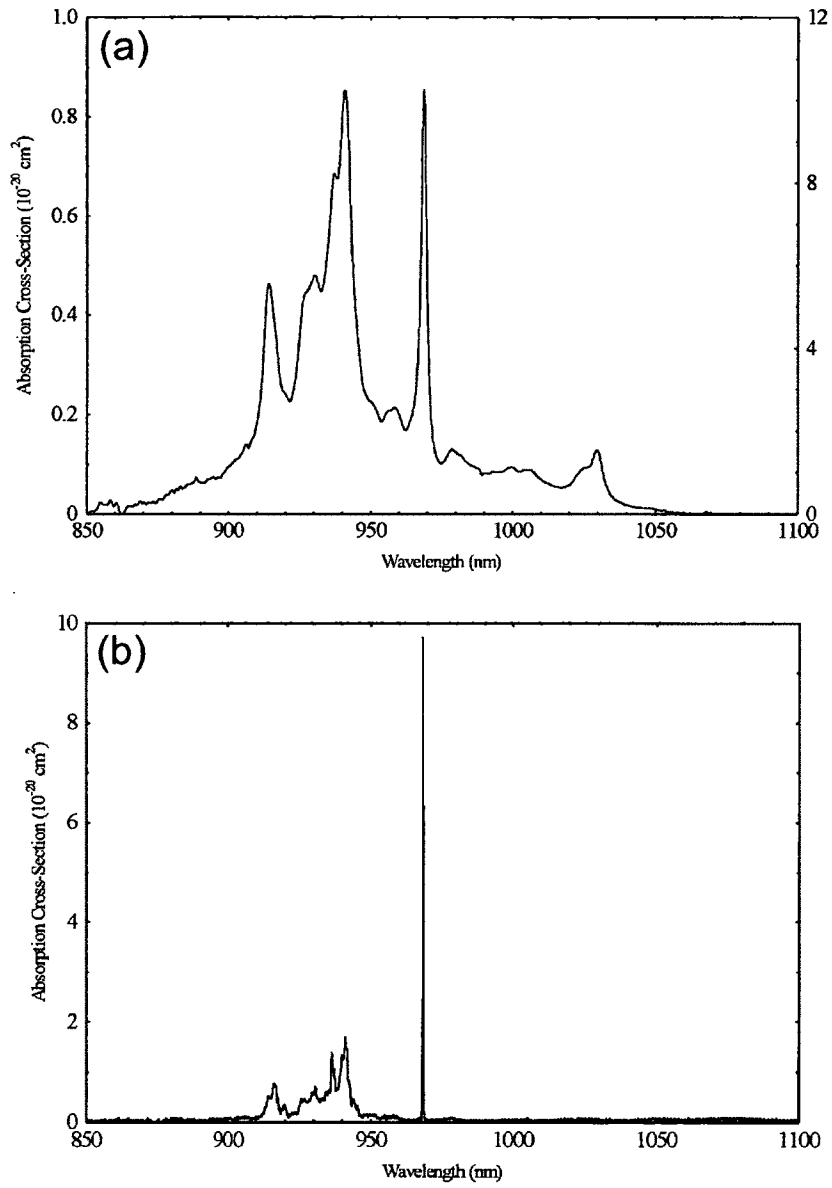


Figure 2.6: Absorption spectra of Yb 9 % at. doped YAG at (a) room temperature and (b) liquid nitrogen temperature (from ref. [24])

cryogenically cooled Yb:YAG cw laser with a maximum output power of 308 W [26] and a mode-locked oscillator based on thin disk Yb:YAG at room temperature producing femtosecond pulses with an average power of 16.2 W [27]. In fact, thin disk is already a quite mature technology with more than 15 years of development and it has been possible to generate Yb:YAG thin disk cw-lasers with 5.3 kW of average power [28]. Thin-disk technology is based on the idea that a very thin laser crystal (a few hundred microns thick) used in an active mirror configuration and cooled from the back face can overcome all thermal problems since the thermal gradient is axial and not radial, and the heat has to flow only through the thin thickness of the crystal.

For nanosecond pulses (not CPA systems) it has been possible to amplify the energy per pulse up to 200 mJ running at 100 Hz repetition rate with cryogenically cooled Yb:YAG in a MOPA (Master Oscillator Power Amplifier) configuration [29].

For the case of CPA systems we can divide the work in the literature in two cases: room temperature and cryo-cooled Yb:YAG. There are two room temperature systems of particular interest because of the similarity with the CPA system developed for this dissertation. Wandt *et al.* reported 1 J uncompressed pulses at 10 Hz from a system that combines fiber amplifiers, an Yb:glass regenerative amplifier and a multipass Yb:YAG power amplifier [30]. This system is designed for pumping an Optical Parametric Chirped Pulse Amplification (OPCPA) system

and the authors expect to upgrade the pump system to obtain 1 ps pulses with 50 J at a repetition rate of 10 Hz.

More interesting for this dissertation is the work of Tümmler *et al.* at the Max Born Institute [31]. These authors are developing an all diode-pumped CPA system for pumping soft x-ray lasers as well. Their system however, is based on thin-disk room temperature Yb:YAG amplifiers. Although thin-disk technology is very mature, it has never been used before to generate high energy (> 1 J) pulses. The reported performance of their laser system shows uncompressed 320 mJ pulses at 100 Hz. The authors claim that the amplified spectral bandwidth can support pulse durations shorter than 2 ps. The system consists of a Yb:KGW oscillator and pre-amplifier to bring the energy per pulse to 1 mJ. The seed pulses are amplified to about 165 mJ by a thin-disk Yb:YAG regenerative amplifier and after that, a multipass amplifier takes the energy per pulse to more than 300 mJ.

Although the authors envision the system to be scalable in energy just by adding more amplification stages, some problems must be solved. The thermal performance of thin-disks has been successfully demonstrated but the thin-disk geometry forces a transversal gain much higher than the gain in the direction of propagation of the amplifying beam. As the diameter of the gain region becomes much bigger than the thickness, spontaneously emitted photons in the transversal direction can stimulate a non negligible number of transitions and deplete the upper laser level. The higher the small signal gain coefficient the worse the effect

of amplified spontaneous emission (ASE). As a direct consequence of ASE, the stored energy is effectively reduced. Thin disk amplifiers are designed to have a very small signal gain coefficient, but this in turn requires a larger number of passes through the gain material that can potentially increase wavefront distortions in the beam.

All the challenges mentioned in the last two paragraphs must be overcome for the thin disk CPA system to generate energies in excess of hundreds of mJ, as required for soft x-ray amplification.

In the case of cryogenically cooled Yb:YAG, soon after some of the results presented in this dissertation were published, Hong *et al.* reported the generation of 15 ps pulses with more than 30 mJ at a repetition rate of 2 kHz [32]. In their CPA system the laser pulses are amplified in a cryo-cooled Yb:YAG regenerative amplifier followed by a multipass cryo-cooled Yb:YAG amplifier. This laser is designed to pump an OPCPA system.

In the following section our all diode-pumped CPA system developed for pumping soft x-ray lasers will be described in detail. This laser system is the first all diode-pumped CPA capable of generating sub-10 ps pulses with 1 J of energy per pulse.

2.2 Description of the all diode-pumped CPA laser system

As it was mentioned in chapter 1, in order to pump a soft x-ray laser two or more high energy pulses from an optical laser are focused into a line on a solid target. One or more pre-pulses of typically several hundred ps duration create a plasma which is subsequently heated suddenly by a short pulse (< 10 ps), creating the necessary conditions for population inversion and amplification.

In the soft x-ray laser system developed for this work, the pump pulses are generated in a Yb:YAG CPA system comprising a laser oscillator where very short pulses are created at low energy per pulse, two grating stretchers to lower the intensity, two amplification stages to reach the J-level energy and a vacuum grating pulse compressor where the pre-pulses are further stretched in time and the plasma heating pulse is recompressed to less than 10 ps. A block diagram of the CPA is shown in fig. 2.7 including also the focusing chamber and the target chamber used for the soft x-ray laser.

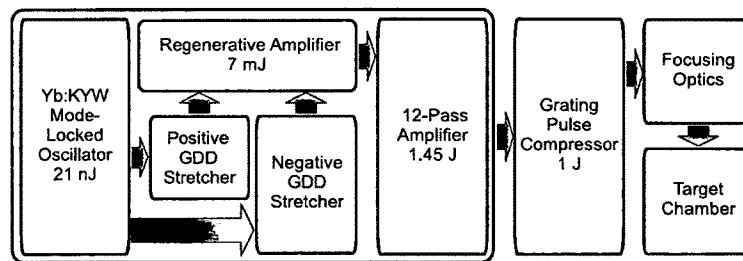


Figure 2.7: Block diagram of the CPA system and soft x-ray laser. The oscillator, stretchers and amplifiers are shown to fit on a single 12×5 ft² optical table

2.2.1 Oscillator

The oscillator creates the short pulses that are later amplified. The gain material is Yb³⁺-doped Potassium Yttrium Tungstate (Yb:KY(WO₄)₂ or Yb:KYW). Similar oscillators based on Yb:KYW have been demonstrated previously [33, 34]. The crystal has a square cross-section of 5 mm by 5 mm and a thickness of 2 mm and has antireflection coatings on both faces to minimize reflections at the pump and laser wavelengths. The lasing wavelength can be tuned from 1029 nm to 1036 nm. The material presents a strong peak of absorption at the pump wavelength of 981 nm. However this absorption band is not very broad and the temperature of the laser diode has to be carefully tuned for the emission wavelength to peak at 981 nm.

The pump laser is a 30 W fiber coupled laser diode (Jenoptik JOLD-30-FC-12-980), with a fiber of 200 μm core diameter. The characteristics of the light coming out of the fiber make it difficult to focus the pump light onto a small spot, a desirable condition to reach the saturation intensity with the pulses oscillating in the cavity. More specifically, the pump light has the numerical aperture of the fiber (0.22), and it is not possible to collimate the beam using a lens. Therefore, a combination of achromatic lenses was used to make a 1:1 image of the output of the fiber on the crystal. In this way the size of the pump beam on the crystal is $\sim 200 \mu\text{m}$ FWHM. Furthermore, this determines the size of the cavity mode in

the crystal, since a good mode matching between the cavity mode and the pump beam is necessary for efficient operation.

The laser cavity is completed by a series of mirrors that provide a collimated section where we introduced a pair of prisms and a waist ($\sim 100 \mu\text{m}$ spot size) where a semiconductor saturable absorber mirror (SESAM) is placed. The SESAM in combination with the prisms are the key elements to operate the oscillator in mode-locking regime and therefore, to generate short pulses [35–37]. The SESAM itself, a 2 % unsaturated absorption from BATOP Optoelectronics (model 340-IIa.18; A=2 %) provides the mechanism to mode-lock the laser. In fig. 2.8 the oscillator cavity is illustrated.

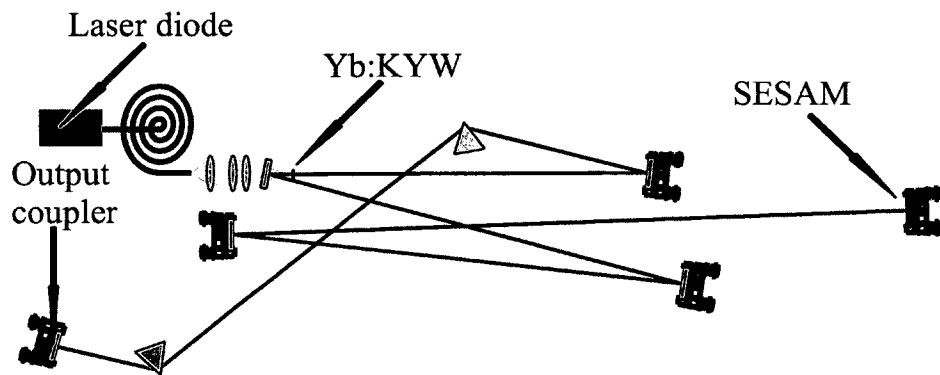


Figure 2.8: Sketch of the oscillator cavity and the fiber coupled pump laser

In order to achieve stable mode-locking with the shortest possible pulses, the intracavity group delay dispersion (GDD) must be compensated. The GDD is the second term in the polynomial expansion of the spectral phase of the pulses, as defined later in this chapter. A positive GDD component is generated in the

SESAM and in the gain material. The mirrors in the cavity, developed in-house, give a negligible contribution to the GDD since the coatings were designed to have minimum GDD around the laser wavelength. These coatings were tested using a white-light interferometer, based on the technique presented in ref. [38]. The necessary negative GDD contribution comes from a combination of two prisms located in a collimated section of the cavity. The distance between prisms and prism insertion into the beam had to be optimized to compensate the GDD of the pulses inside the cavity [35].

The output coupler of our cavity is a 94 % reflection mirror also coated in our facilities, and allows for an output power of 1 W. Although we were able to generate laser pulses with a maximum bandwidth of 5.8 nm centered around 1034 nm and a pulsewidth of 300 fs, the central wavelength is normally tuned closer to 1030 nm to match the lasing wavelength of the Yb:YAG amplifiers and the pulses get slightly longer. Nevertheless, the generated bandwidth of several nm is more than enough to seed the amplifiers. The repetition rate of the oscillator is given by the cavity length and in this case is 58 MHz. Fig. 2.9 shows the spectrum of the pulses generated in the oscillator.

Any reflection from outside the cavity coming back into the oscillator cavity can produce feedback that stops mode-locking. To avoid this problem a Faraday isolator was placed at the output of the oscillator. Also, part of the signal is sent out to a photodiode (by means of a half waveplate and a cube polarizer) to be

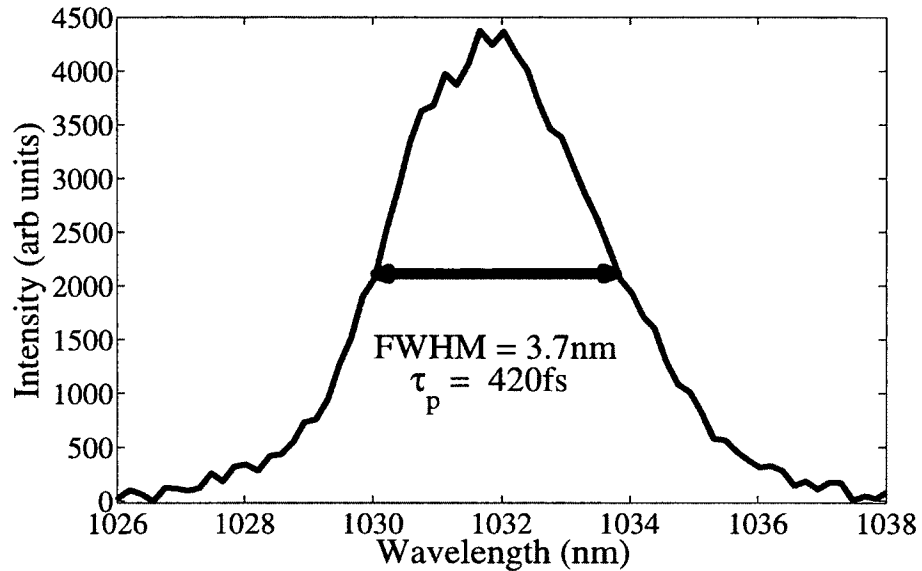


Figure 2.9: Spectrum of the oscillator pulses after blue-shifting the central wavelength. The transformed limited pulse duration for this bandwidth is 420 fs

used as the master clock signal of the whole system. The beam is collimated in a 1:1 telescope and after that, it is divided into two beams that go to two different grating stretchers. To divide the beams we used again a combination of a quarter waveplate and a cube polarizer, such that the relative intensities between these two trains of pulses can be changed continuously. Fig. 2.10 shows a picture of the oscillator, the isolator and other optical components used to direct the pulses into the stretchers and from the stretchers to the first amplification stage. The oscillator is kept in a closed plexiglass box to increase the stability of the laser, that is affected by air flows.

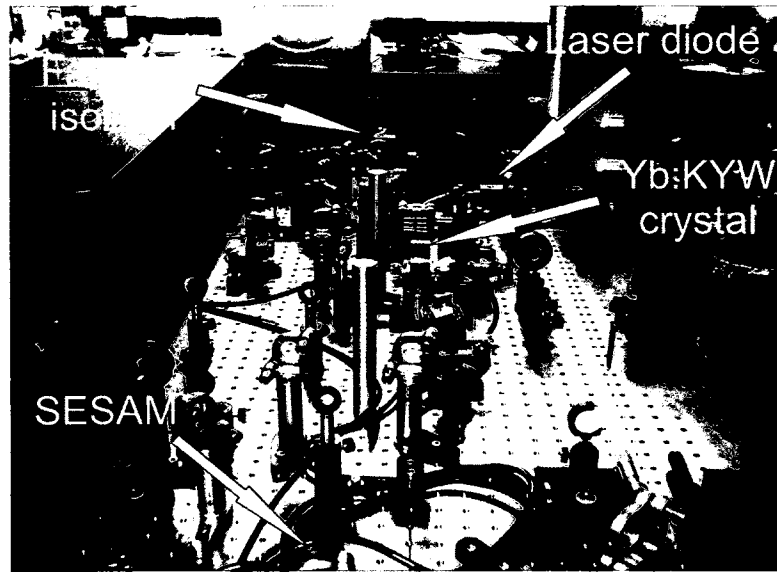


Figure 2.10: Picture of the oscillator

2.2.2 Grating stretchers

A grating stretcher introduces a controlled temporal chirp in the pulse that can be later on compensated in a grating compressor. As described in chapter 1, this is the standard and largely used configuration of a CPA system [39,40]. As previously mentioned, the stretcher introduces a spectral phase term that is quadratic in the frequency, known as GDD. This produces a stretch in the pulse duration because different frequency components travel a different path in the optical arrangement and as a result the pulse is spread out in time. There are also higher order terms that must be considered and whose compensation in the compressor is fundamental to reach the shortest possible pulse with the given bandwidth (transformed limited pulse). The stretcher designed by Martinez [40,41] allows to perfectly compensate

all the orders in the expansion of the phase (unless for mismatch arisen due to aberrations) if a compressor according to Treacy's design is used [23] and the gratings in the compressor and the stretcher have the same dispersion (number of lines per mm). In our case, the bandwidth is small enough so that orders higher than the second term (the GDD) may be safely neglected.

Mathematically this can be easily visualized assuming a Gaussian temporal profile for the pulses coming into the stretcher. In that case the complex electric field may be written as:

$$E_{in}(t) = E_0 e^{-t^2/\tau^2 - i\omega_0 t} = \frac{1}{\sqrt{2\pi}} \int_{-\infty}^{+\infty} E(\omega) e^{-i\omega t} d\omega \quad (2.7)$$

In this expression $E(\omega)$ is the frequency dependent Fourier transform of the pulses that contains the information of the spectral profile of the pulses. The pulse duration is determined by the parameter τ . Assuming that no losses are introduced in the stretcher, the pulses coming out may be written as the pulses coming in with an additional phase term that depends on the frequency:

$$E_{out}(t) = \frac{1}{\sqrt{2\pi}} \int_{-\infty}^{+\infty} E(\omega) e^{-i\omega t + i\varphi(\omega)} d\omega \quad (2.8)$$

The phase term may be written as a series in powers of $\omega - \omega_0$ with ω_0 the carrier frequency:

$$\varphi(\omega) = \varphi(\omega_0) + a(\omega - \omega_0) + b(\omega - \omega_0)^2 + \dots \quad (2.9)$$

$$a = \left. \frac{d\varphi}{d\omega} \right|_{\omega=\omega_0} \quad (2.10)$$

$$b = \left. \frac{1}{2} \frac{d^2\varphi}{d\omega^2} \right|_{\omega=\omega_0} \quad (2.11)$$

with a the Group Delay and b the Group Delay Dispersion or GDD. Now, if we expand the introduced phase only to second order and recover the temporal profile of the pulse by solving the Fourier transform we find:

$$E_{out}(t) \propto \exp \left\{ -\frac{(t-a)^2}{\tau^2(1+16b^2/\tau^4)} \right\} \quad (2.12)$$

From equation 2.12 we see how the pulse duration increases when b is different from zero. In fact, the Full Width at Half Maximum (FWHM) of the pulse increases by a factor of $\sqrt{1+16b^2/\tau^4}$. Therefore, in order to get the shortest pulses supported by the bandwidth, the GDD must be compensated, in other words, made equal to zero. This is what happens in a standard CPA system: the grating stretcher introduces a positive GDD that is compensated after amplification by a negative GDD introduced by the compressor.

At the output of the oscillator the pulses are divided into two beams, and each beam goes to a different grating stretcher. The first stretcher, shown schematically in fig. 2.11, is a regular (positive GDD) grating stretcher built with an 1800 lines/mm holographic grating from Newport Corp, and an Offner telescope. The use of an Offner telescope significantly increases the obtainable stretch without increasing the physical size of the stretcher. The pulses are stretched to 190 ps for a bandwidth of 0.23 nm when making two passes through the stretcher. This bandwidth and the resultant pulsewidth are measured after amplification in the first amplifier where most of the gain narrowing occurs.

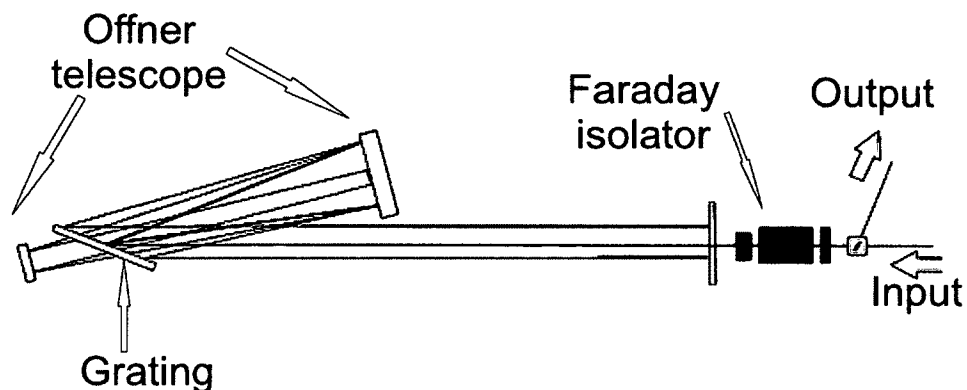


Figure 2.11: Sketch of the positive GDD stretcher

By design, the stretcher only clears part of the oscillator bandwidth and centers it around 1030 nm, the central wavelength of the Yb:YAG amplifiers. In this stretcher, the sign of the introduced GDD is positive and therefore after the compressor these pulses will be the short pulses that heat the plasma for the generation of a population inversion.

The second stretcher is very similar to a folded one-grating compressor [42]. It utilizes a blazed grating with 1714 lines/mm and introduces a smaller stretch in the pulses: the pulses are stretched to 150 ps for 0.23 nm of bandwidth. But more important, the introduced GDD is negative, and therefore, these pulses will be further stretched in the compressor. A sketch of the negative GDD stretcher is presented in fig. 2.12

Furthermore, before entering this stretcher the pulses are divided into two beams and a delay of 4 ns is placed between these two beams before recombining

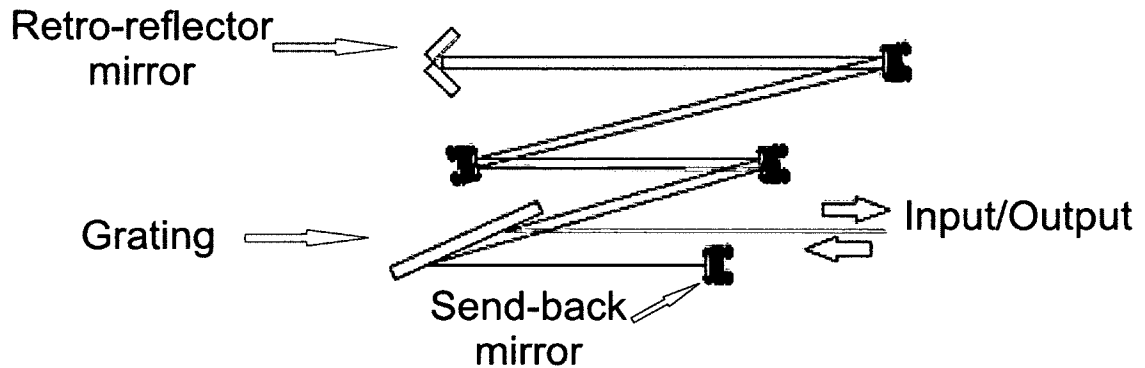


Figure 2.12: Sketch of the negative GDD stretcher. The pulses come out of the stretcher on top of the input pulses due to a tilt introduced by the send-back mirror

them. Also, the pulses coming first in time can be attenuated continuously by means of a half waveplate and a wire polarizer to change the relative intensities.

The outputs of both stretchers are then recombined and they form the seed pulses for the first amplification stage. A movable delay is placed between these two outputs so that the set of collinear pulses is as follows:

- A first pre-pulse, with negative GDD (will be stretched in the compressor) and the lowest energy.
- A main pre-pulse, also with negative GDD, coming 4 ns after the first pre-pulse.
- The plasma heating pulse, with positive GDD (will be compressed in the compressor) coming between 200 ps and 1.2 ns after the main pre-pulse. We can also change the range of this delay easily to explore other regions of

the parameter space. This is usually the most energetic pulse, although the relative energies of all the pulses can be changed.

In fig. 2.13 both stretchers are shown, together with multiple mirrors to produce the proper delay between the different seed pulses.

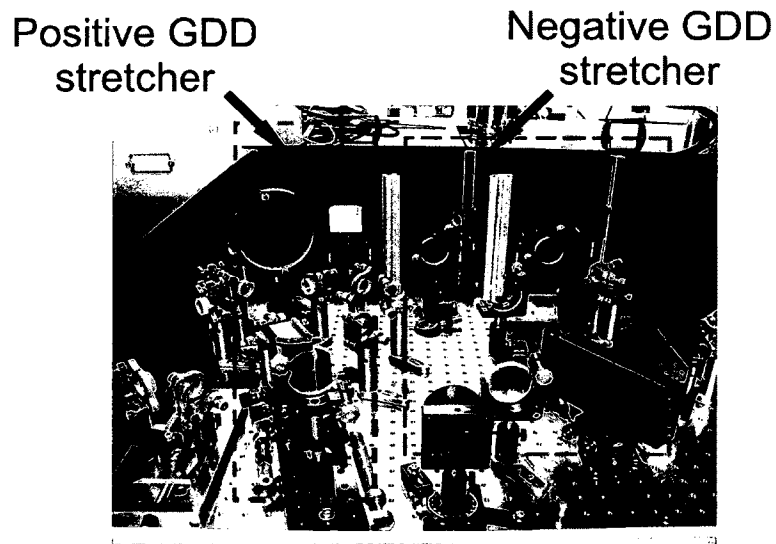


Figure 2.13: Photograph of the stretchers

One important characteristic of this configuration is that the pre-pulses and the heating pulse travel collinearly after being recombined at the output of the stretchers. Moreover, since the alignment of any beam coming out of the regenerative amplifier is given by the amplifier cavity, this ensures that the pre-pulses and the heating pulse are always aligned one with respect to the others, or to put it another way, the overlap between the pre-pulses and the main pulse is ensured and there is no shot to shot variation in the overlap. This configuration is a significant

improvement over what is currently being used in our group for the generation of laser pumped soft x-ray lasers where the pre-pulses take a different path from that of the short pulse.

2.2.3 First amplification stage: Regenerative amplifier

In the stretchers only a portion of the spectral bandwidth of the pulses is cleared and in addition there is a big loss in the grating ($\sim 20\%$ per bounce). As a consequence the energy of the seed pulses is reduced from ~ 20 nJ out of the oscillator to less than 100 pJ. A first amplification stage, a regenerative amplifier shown in fig. 2.14 is used to boost the energy per pulse from the pJ range to a few mJ.

In a regenerative amplifier the gain medium is in a laser cavity that also contains a thin film polarizer and a Pockells Cell (PC) that select the polarization of the oscillating light (see fig. 2.14). When no high voltage is applied to the PC, the crystal of the PC does not change the beam polarization. The s-polarized seed beam is introduced into the cavity by reflecting off the thin film polarizer (TFP), and it is transmitted through the PC and the quarter waveplate to the end mirror and back. Double passing the waveplate changes the polarization to p and the beam goes through the TFP and to the other end of the cavity, where the Yb:YAG crystal is located inside a vacuum chamber. When it returns, it goes through the TFP again, the PC and again twice through the waveplate, changing

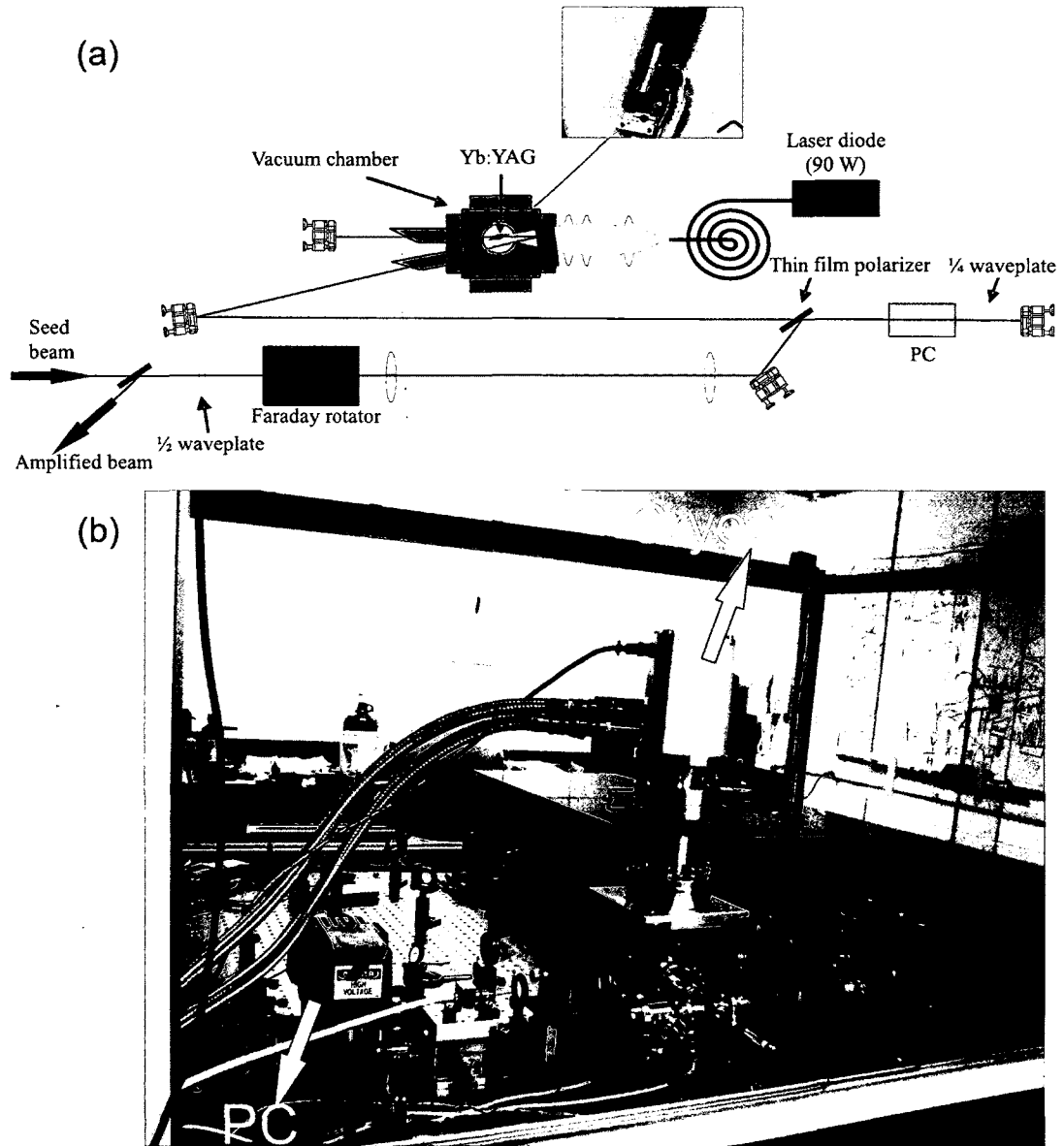


Figure 2.14: (a) Sketch of the regenerative amplifier. (b) Photograph of the amplifier

the polarization back to s, and so, reflecting off the TFP out of the cavity. At some point in time (synchronizing with the end of the pump pulse), the high voltage applied to the PC is switched on. This has to be done when there is already a pulse oscillating inside the cavity, in the section where the crystal is. For this p-polarized pulse, the effect of the PC is to introduce a quarter rotation in the polarization in a single pass. Double passing the PC and the waveplate provides a full rotation to the beam polarization, and therefore, the pulse remains p-polarized and keeps oscillating inside the cavity until all the energy stored is extracted. When this happens and the pulse energy stops growing and begins to decrease in every pass due to cavity losses, the high voltage is turned off and the amplified pulse gets out of the cavity. For the pulses that keep arriving during the time that the PC is on, the combined effect of the PC and the waveplate provides a complete rotation in the polarization and they go in and out of the cavity without passing through the gain material. Therefore, only one pulse is amplified. In our case there are actually three pulses being amplified (two pre-pulses and the plasma heating pulse), and that is made possible by selecting the proper time window in the PC.

In the regenerative amplifier the gain medium is a single crystal 5 at-% Yb:YAG disk 5 mm in diameter and 2 mm in thickness cut at Brewster's angle (Scientific Materials). The crystal is mounted on a copper cold finger which is connected to the heat exchanger of a Helium cryostat (Cryomech PT60). Also attached to the cold finger there is a diode temperature sensor (Omega CY7-ET4)

and a 70 W electrical heater (Watlow Heaters) to control the temperature of the crystal. Everything sits inside a compact vacuum chamber. As part of the cavity is one of the ports of the chamber, consisting of a dichroic mirror. This mirror works as a fold mirror for the cavity at the laser wavelength and as a window with an anti-reflection coating for the pump wavelength.

The pump laser is a 90 W laser diode from Bright Solutions (BDL90-940-F6) coupled to a 600 μm core optical fiber. The numerical aperture of this fiber is 0.22. The optical system that creates a 1:1 image of the output of the fiber in the crystal is very similar to the one used in the oscillator. It combines 2 achromatic lenses and one meniscus lens to minimize the effect of spherical aberrations. This optical arrangement produces a $\sim 700 \mu\text{m}$ diameter spot on the crystal. The pump pulse was normally selected to be 2 ms long (\sim twice the upper level lifetime of Yb:YAG). To synchronize the pump pulses with the seed pulses we combine a delay generator with the PC driver (Medox from Thales Laser) using the oscillator pulses as a master clock (electrical signal from a photodiode). The delay generator triggers the pump pulses and a trigger signal is sent to the PC driver at the end of the pump pulse. The PC driver takes the trigger signal from the delay generator, but it doesn't trigger until it receives the next clock pulse. At that moment it fires the PC and the time that it stays open (high voltage on) is proportional to the number of oscillator cycles selected in the driver. These two events (switching on

and off the high voltage) serve as trigger signals for other events in the experiment (triggering cameras, a shutter, etc).

This amplifier was tested at different repetition rates up to 100 Hz. A maximum output pulse energy higher than 7 mJ was obtained when operating at 106 K to mitigate the excessive bandwidth narrowing. Even when the seed pulses have a bandwidth of ~ 1 nm, gain narrowing during amplification dramatically reduces this bandwidth, setting a limit to the shortest pulse that can be obtained after compression. Moreover, bandwidth reduction decreases the duration of stretched pulses [23], and therefore increases the intensity of the pulses being amplified. This is a very delicate matter when working very close to the damage threshold of the optical components. Although gain narrowing takes place in both amplifiers, the contribution to gain narrowing in the second amplifier is negligible compared to the effect occurring in the first amplification stage. The reason is simple: in the regenerative amplifier the energy per pulse is increased more than 10^8 while the overall gain in the second stage is less than 10^3 . We studied the gain narrowing effect in the regenerative amplifier at different temperatures by taking autocorrelations of the amplified pulses and also measuring the bandwidth with a monochromator. For the selected operating temperature of 106 K the measured bandwidth is 0.23 nm.

After amplification the pulses go back to the Faraday rotator keeping the s-polarization as they are ejected out of the amplifier. This is also true for the non-

amplified pulses and whatever leak may occur due to imperfections in the TFP or the degree of rotation in the PC (extra pulses that may have some degree of amplification). To avoid amplifying unwanted pulses in the second stage, a second PC in combination with a TFP was placed in the path of the beam (Impact 13 from Cleveland Crystals). In this case the PC provides a half-wave rotation (this is accomplished by changing the voltage on the cell) and only during the selected time window the polarization is rotated from s to p and can go through the TFP.

Another important issue when amplifying high energy pulses is the beam shape and quality. Before sending the beam to the second stage we correct the astigmatism with a pair of cylindrical lenses and clean the beam using a serrated aperture and a spatial filter. The serrated aperture converts a Gaussian beam into a flat top, or a super Gaussian [43]. This must be done in combination with a spatial filter (Newtonian telescope with a pinhole at the focal plane) to clean out all the frequency components that don't contribute to the desired beam shape. A beam profile that is approximately Gaussian but with sharper edges is obtained. This beam shape allows for more efficient energy extraction in the second amplifier. About 15 % of the output energy from the regenerative amplifier is lost reshaping the beam.

2.2.4 Second amplification stage: Multipass amplifier

The second amplification stage is a multipass amplifier. The gain material is 2 at-% doped Yb:YAG and it is divided into two 5 mm thick crystals mounted on opposite faces of a copper cold finger cooled by liquid nitrogen, in an active mirror configuration. In this way the crystals are cooled from the back face minimizing radial thermal gradients, which are responsible for thermal lensing. An indium layer of 250 μm is placed between the copper cold finger and the crystals to improve the thermal contact. A sketch of the copper cold finger with the crystals and the liquid nitrogen dewar-crystal holder assembly is shown in fig. 2.15. The front faces of the crystal have antireflection coatings for the pump and laser wavelengths and the back faces have high reflector coatings for both wavelengths too. On the side faces the crystals have a Cr^{4+} :YAG cladding to absorb off axis spontaneous emission that otherwise could start oscillating inside the crystal depleting the upper laser level by amplifying the spontaneous emission. The crystals are pressed against the copper using annular copper lids. The cold finger is attached to the heat exchanger of a dewar filled with liquid nitrogen to cryogenically cool the material. The temperature of the cold finger is monitored with a diode sensor (same model as in the regenerative amplifier).

Each crystal is pumped by a laser diode array (GLG Power System from Nuvonyx Incorporated) that provides up to 3.5 kW of output power in 2 ms pulses. The array consists of a stack of 250 diodes arranged in 25 bars of 10 diodes each,

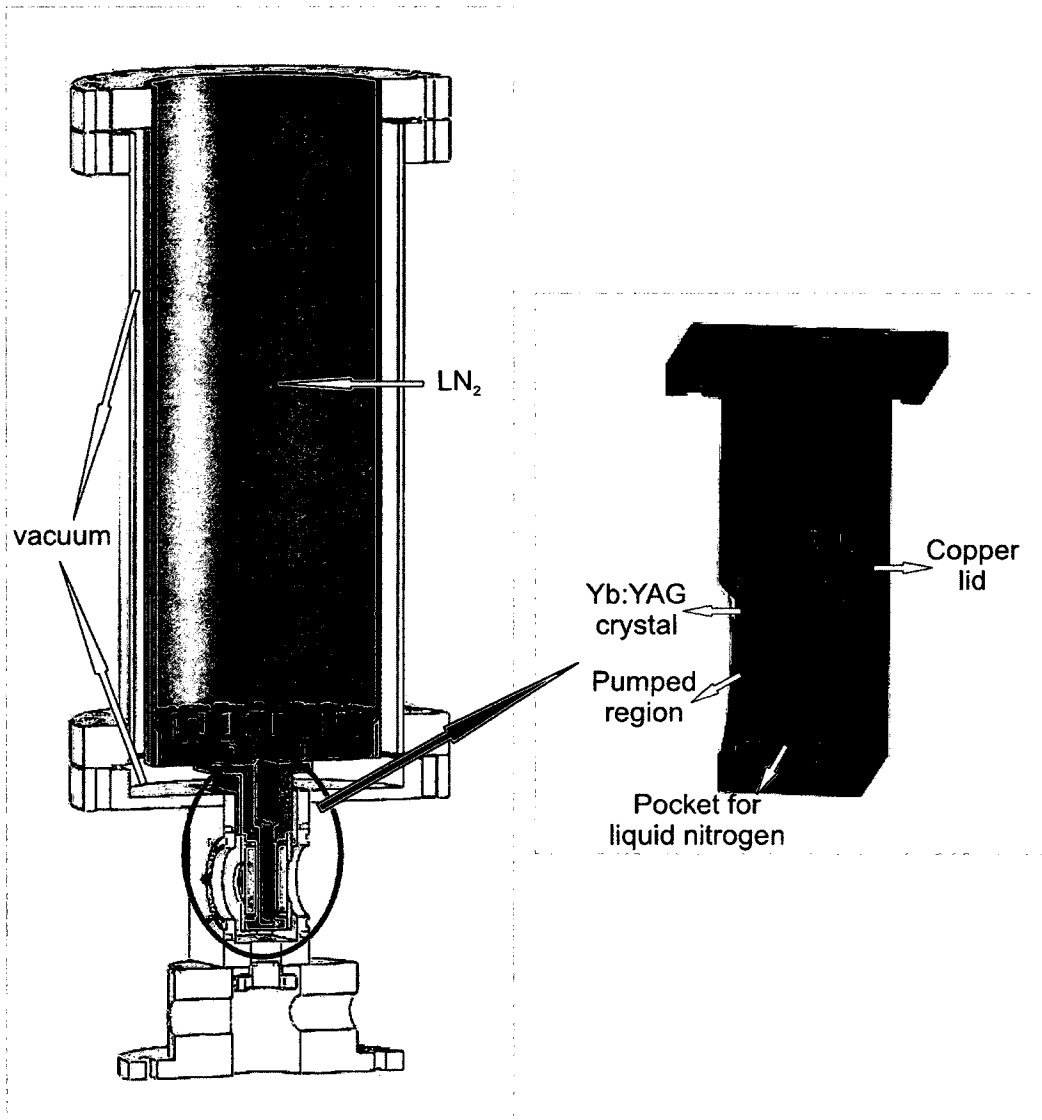


Figure 2.15: Cut of the liquid nitrogen dewar and crystal holder assembly and cut of the copper holder with two Yb:YAG crystals. The region of the crystals pumped by the laser diodes is illustrated in red. The cold finger is filled with liquid nitrogen

placed vertically to form a source with an area of 50 mm by 10 mm. In front of each bar there is a microlens that collimates the fast axis of the diodes. As a result, the output of these lasers is an astigmatic rectangular beam that recreates the structure of the stack. In other words, the beam is a set of lines, not all of them necessarily perfectly straight.

Each pump beam is homogenized by means of a glass rod of 14 inches in length and 4 mm in diameter (fig. 2.16). This is a waveguide and takes the same role

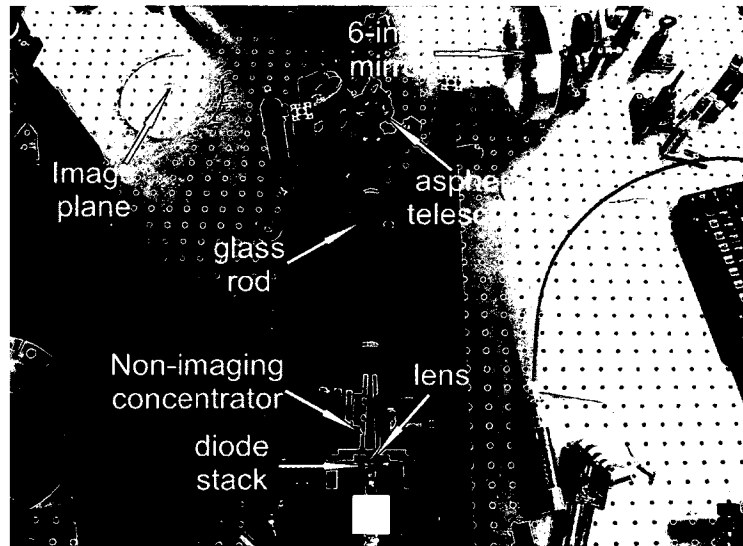


Figure 2.16: Photograph of the optical arrangement used to shape the output of the high power laser diode stacks

as the optical fiber in the other two pump lasers (oscillator and first amplifier). To efficiently couple the light into the rod we combined a short focal length lens ($f = 100$ mm) with a non-imaging concentrator consisting of two flat mirrors at an angle. The high reflector coating for these mirrors as well as the anti-reflection

coatings for the rods have to be effective for a large range of angles, which in practice means that they have to be broadband coatings.

An additional problem with the pump beam is the divergence of the light coming out of the rods. As in the case of the other two pump lasers (oscillator and first stage), this radiation doesn't behave like a beam, in the sense that it can't be collimated, but in this case there is another problem: The divergence of the light coming out of the diodes changes with the current supplied to the diodes, and this in turn changes the beam divergence. At the maximum operational current of the diodes, we measured a full angle divergence of 45 deg defined in such a way that 90 % of the power is contained in the diverging beam.

All these effects have to be taken into account in the design of the optical pump system. To image the output of the rod into the crystals with a 4:1 magnification, a combination of a telescope made with two aspheric lenses and a 6-inch diameter, gold coated, spherical mirror was implemented. The back face of each crystal then, sits on the image plane of each pump arm, where a ~ 16 mm diameter round beam is formed. Fig. 2.17 shows an image of the pump beam at the image plane. The overall efficiency of the optical pump system is ~ 75 % depending on the alignment. This means that each crystal can be pumped with 2 ms pulses of more than 2.5 kW.

To bring the energy to the J-level the pulses are sent through the gain region twelve times by means of a multipass amplifier configuration. A simplified

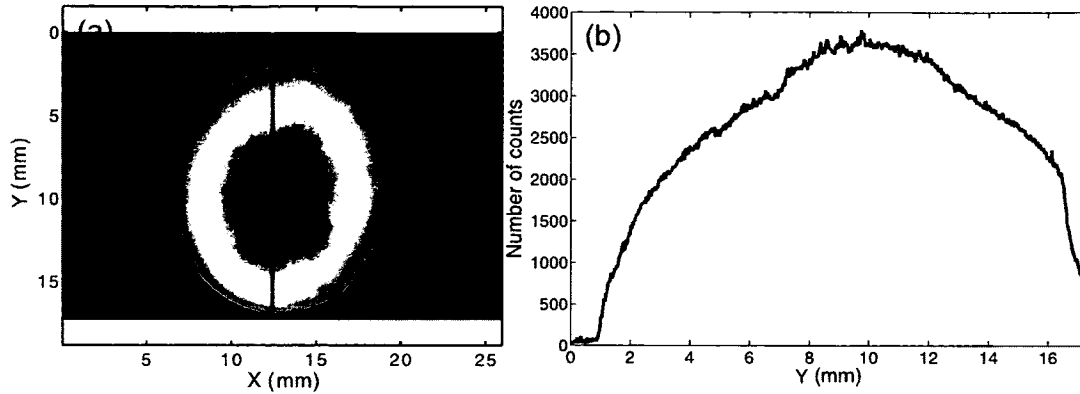


Figure 2.17: (a) Image of one of the pump beams on the crystal position at full pump power. (b) Vertical cut of the pump beam profile

schematic layout of the amplifier is presented in fig. 2.18. The beam diameter is increased to ~ 8 mm in between the two amplification stages to make the initial four passes through the amplifier (two on each crystal) passing through small holes (0.5 inch diameter) in the large mirrors used to focus the pump beams onto the crystals. To make four passes the polarization is changed after the second pass from p to s by double-passing a quarter waveplate ($1/4$ WP in fig. 2.18). Then, the send-back mirror sends the beam back on itself making two additional passes and reflecting off the input thin film polarizer (TFP). A 1:1 telescope and a vacuum tube are placed between the first and the second passes (and hence between the third and fourth passes) to keep a good beam quality.

After these initial four passes the amplified pulses reach ~ 100 mJ, partially saturating the gain in the center. This helps to keep the peak fluence relatively low

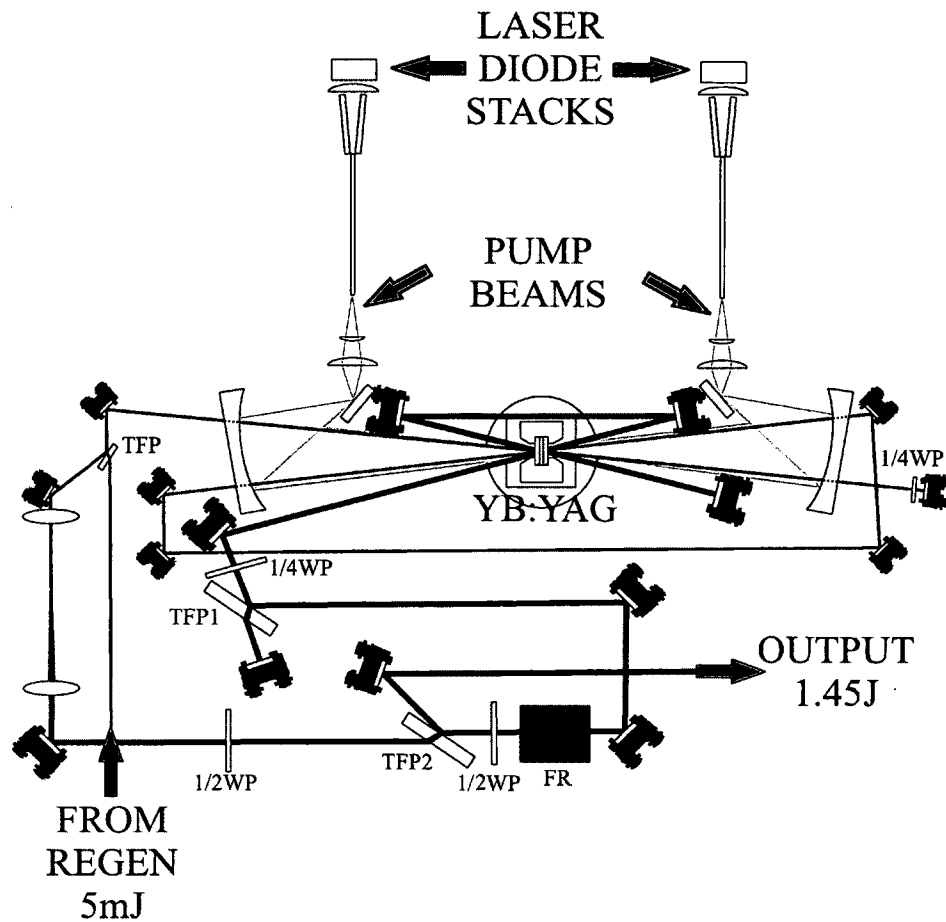


Figure 2.18: Schematic layout of the multipass amplifier

during the amplification process. Subsequently, the beam is expanded to match the size of the pump beams and the pulses are sent eight additional times through the gain medium in the following way: After expansion in the magnifying telescope the pulses are sent through the Faraday rotator (FR), and further amplified in additional four passes. Subsequently the polarization changes from s to p, again by double-passing a quarter waveplate, and the pulses go through TFP1 and are

then sent back on the same path to make four more passes. Finally the pulses switch polarization back to s, and are ejected by TFP2. With this configuration a maximum energy per pulse of 1.45 J was obtained at 10 Hz repetition rate.

Some details are not shown in fig. 2.18. Owing to the low damage threshold of the Faraday Rotator ($\sim 0.3 \text{ J/cm}^2$ for 200 ps pulses), the beam had to be expanded to $\sim 32 \text{ mm}$ on the rotator. This is accomplished in the following way: The telescope after the first four passes has a magnification $M = 4$. Then, after the beam goes through the rotator, a Galilean telescope is used (to avoid adding another vacuum tube) to reduce the beam size to 16 mm. The amplified beam coming out then, goes through the Galilean telescope and gets magnified a factor of 2 before going again through the rotator. In addition to that, two cylindrical lenses were placed after TFP1, between the 9th and the 10th passes, to correct for astigmatism introduced by the crystals. The second amplification stage can be seen in a photograph in fig 2.19.

2.2.5 Compressor chamber

The grating compressor utilizes two 20 cm width by 15 cm height gratings of 1740 lines/mm with dielectric coatings. Dielectric coatings have a higher efficiency and lower absorption than gold coatings typically used in gratings due to their relatively flat response over a broad range of wavelengths. For high average power applications, the absorption of light in gold produces thermal deformation on the

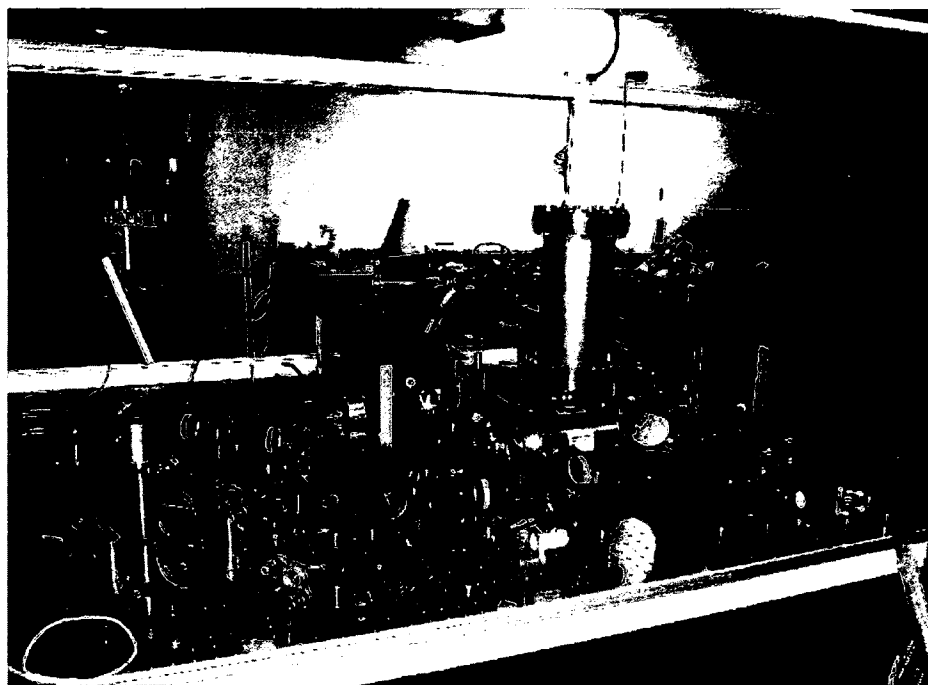


Figure 2.19: Photograph of the multipass amplifier. The picture was taken before placing the vacuum tubes for the Newtonian telescopes in the system

substrate that in turn, deforms the beam. The efficiency of the compressor is 70%. A sketch of the compressor chamber is shown in figure 2.20.

Due to the big stretch factor (~ 800 ps/nm) introduced in the positive GDD stretcher because of the small spectral bandwidth, the required path between the gratings is 2.53 m and therefore, the compressor needs to be folded twice to make it fit in a reasonable sized vacuum chamber. Because of this large path between the gratings, adjusting the position of one of the gratings along the beam path doesn't have a big effect in the pulsewidth of the compressed pulses and makes the angle of the gratings a much more critical parameter when trying to compress to the

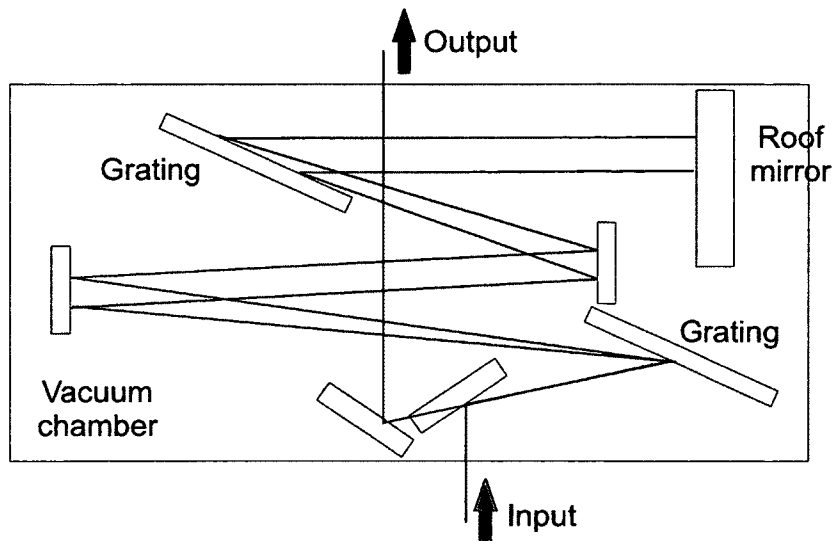


Figure 2.20: Sketch of the compressor chamber

shortest possible pulse. The incident angle on the gratings is -55 degrees from the normal to the plane of the grating, which is ~ 8.7 degrees smaller than the Littrow angle, for which the efficiency of the -1 order of the grating is maximum. The output beam comes out at -77 degrees with respect to the normal (13.3 bigger than Littrow). Of course, for the beam coming back after reflection by the roof mirror, the incident angle on the gratings is 77 degrees. The measured efficiencies for both gratings at these angles are 92% and 95% for 55 and 77 degrees respectively. With these values the theoretical throughput in the compressor is $\sim 76\%$, 6% larger than the measured throughput. Although there is still the efficiency of all the mirrors (8 surfaces with high reflector coatings) and windows (4 surfaces with anti-reflection coatings) that have to be taken into account, the mismatch with the

measured 70 % efficiency probably has to do with a small angle misalignment in the gratings, since the efficiency drops very fast for angles below 56 degrees. In practice the GDD compensation is done by fine-tuning the angle of the grating in the stretcher, since this can be done without changing the alignment. On the other hand, every small adjustment in angles of the compressor gratings requires difficult and time consuming realignment of the whole compressor optical arrangement.

To illustrate the compactness of the system, fig. 2.21 shows a photograph of the all diode-pumped CPA system and the focusing and target chambers used for soft x-ray laser generation.

2.3 CPA laser system output characteristics

The cryogenically cooled Yb:YAG regenerative amplifier described in section 2.2.3 amplifies pulses from an energy of hundreds of pJ to a few mJ. To test the amplifier the seed pulses coming from the negative GDD stretcher were blocked and only the plasma heating pulse, that is the pulse with positive GDD was amplified. Fig. 2.22 shows the variation of the energy per pulse as a function of pump peak power for different repetition rates.

The regenerative amplifier boosts the pulse energy to more than 7 mJ. The measurements in fig. 2.22 were taken pumping with 2 ms pump pulses from the 90 W fiber coupled laser diode. The output energy and beam quality were observed



Figure 2.21: Photograph of the all diode-pumped CPA system and soft x-ray laser. At the front the oscillator can be observed. Right behind, the head of the cryostat for the first amplification stage and the dewar for the second stage can be seen, and on the back, the vacuum chambers for the compressor, the focusing optics and the target assembly

to remain practically unchanged as the repetition rate was increased up to 100 Hz. The shot to shot energy variation was measured to be less than 1 %. However, it can be seen from fig. 2.22 that the output energy is slightly higher for higher repetition rates. At higher repetition rates the temperature of the laser diode increases slightly and the emission wavelength moves closer to the peak of absorption of Yb:YAG. This is due to the fact that the temperature of the water used to

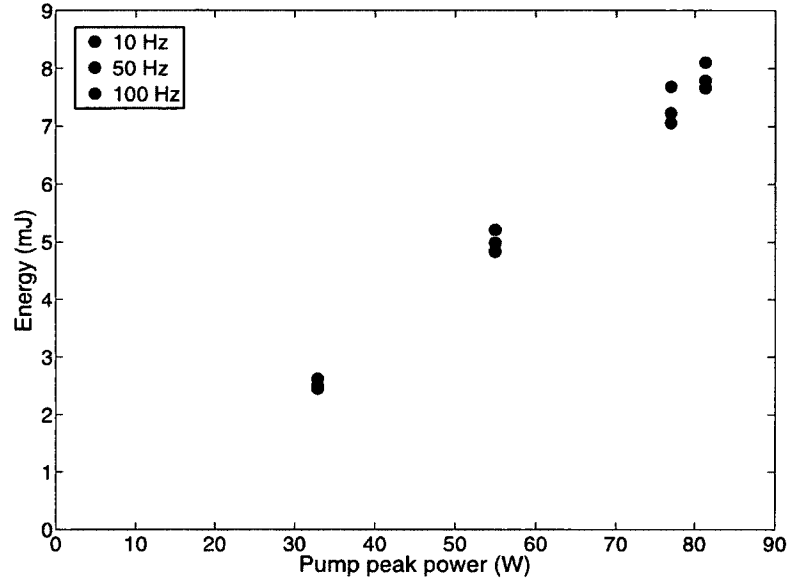


Figure 2.22: Output pulse energy of the first amplification stage for different repetition rates between 10 Hz and 100 Hz

cool down the diode is not tuned to control the emission wavelength and, at low repetition rate, the diode does not emit at 941 nm, but at a shorter wavelength (~ 938 nm). At higher repetition rate the temperature of the diode increases and the emission wavelength shifts closer to the absorption peak of Yb:YAG. Nevertheless, the absorption bandwidth is so broad, even at cryogenic temperatures, that this effect is not very significant (see for instance ref. [44]).

The amplified beam coming out of the regenerative amplifier is shown in fig. 2.23. This image was taken after the beam went through a 2.5 magnification telescope, a serrated aperture of 8 mm nominal diameter and a spatial filter,

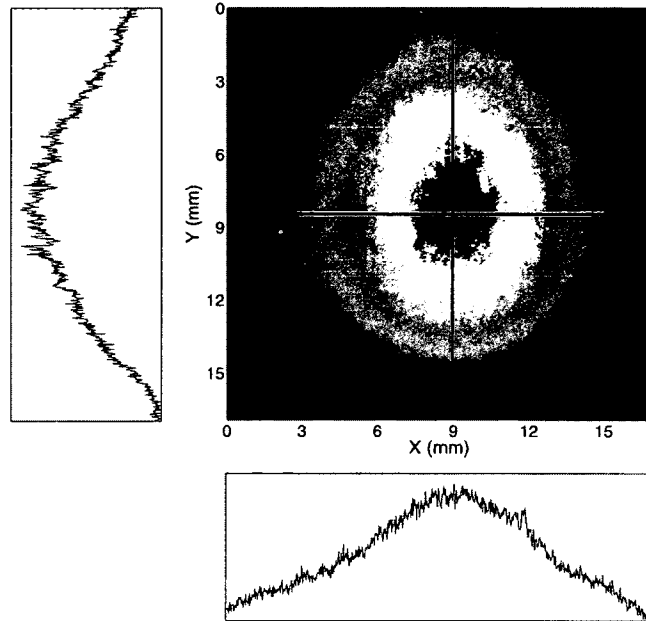


Figure 2.23: Image of the beam amplified in the regenerative amplifier after a serrated aperture, spatial filter, magnification and propagation

another telescope with a magnification $M = 2$ and several meters of propagation. The beam profile has sharper edges than a Gaussian, as discussed previously.

The temporal profile is cleaned from residual pulses coming before and after the set of pulses to be amplified in the second amplification stage (also described previously in this chapter). The combined pulse energy of the pulses entering the second amplification stage after cleaning up the temporal profile and reshaping the spatial profile is ~ 5 mJ.

In the first four passes through the second amplification stage the amplifying beam diameter is shaped to be ~ 8 mm and the beam propagates through 0.5 inch holes in the 6-inch diameter pump mirrors. In this first four passes the unsaturated single pass gain in each crystal at the maximum pump power is slightly bigger than 3. Fig. 2.24 illustrates the single pass gain as a function of pump power for the 8 mm beam, when pumping with a 16 mm beam. Also in the same plot, single

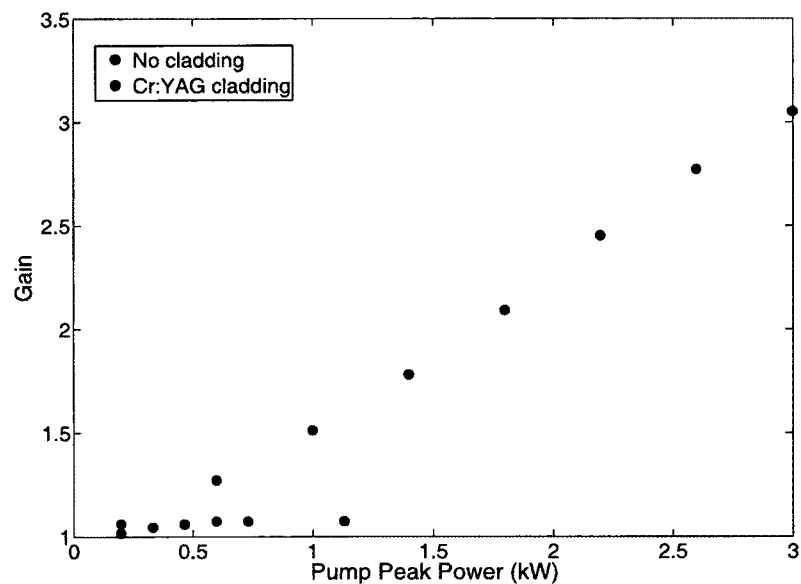


Figure 2.24: Single pass gain with the small beam. The figure also shows the gain when the crystal does not have a Cr:YAG cladding

pass gain measurements in the same configuration but using an Yb:YAG crystal without the Cr:YAG cladding can be seen. In this case the effects of Amplified Spontaneous Emission (ASE) are devastating. The gain does not go over 1.05 since

all the energy is extracted by photons being emitted in the transversal direction. In fact, it is possible to observe parasitic lasing in this configuration since the transversal radiation can oscillate within the crystal due to total internal reflection in the side walls of the Yb:YAG. The Cr:YAG cladding then, is a crucial element of the amplifier. A cladding of any material absorbing the transversal radiation would do the work in principle. However, Cr:YAG has the double advantage of automatically matching the index of refraction of the gain material and also the thermo-mechanical properties. If the cladding had a different coefficient of thermal expansion than Yb:YAG, the bonding would fail when the crystal assembly is cryogenically cooled. A picture of the crystal assembly is shown in fig. 2.25.

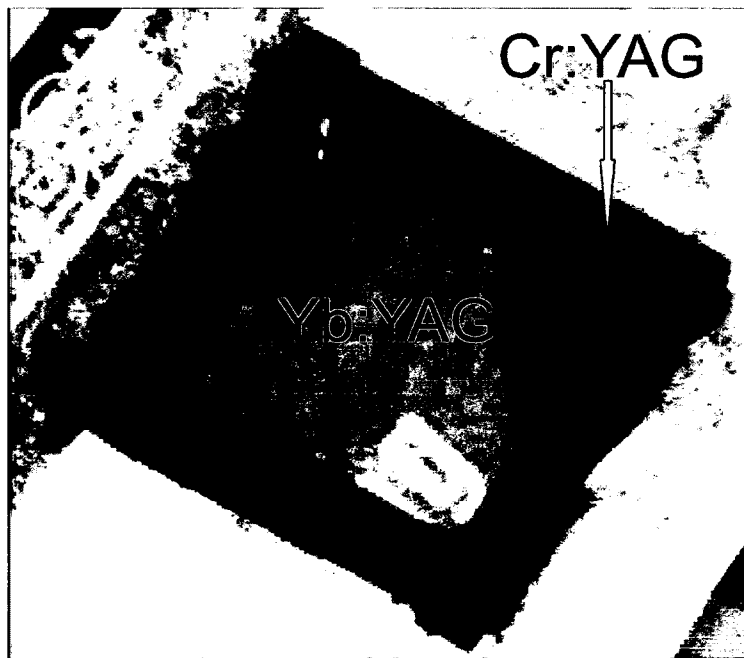


Figure 2.25: Picture of the Yb:YAG crystal with the Cr:YAG cladding

The cladding counteracts the effects of feedback, but the effects of ASE are still present in this amplifier. After all, the transversal gain is always higher because in the pumped volume the dimension in the direction of propagation of the amplified beam is smaller than the transversal dimension. As a consequence the gain has to be kept relatively small, otherwise the transverse gain could be high enough to deplete considerably the upper laser level by one pass of spontaneously emitted photons through the gain medium. This is extremely important in the case in which the gain material is pumped during a time comparable to the upper level lifetime, as it is the case in diode-pumping. In ref. [45] the case of ASE in high gain Yb:YAG slabs is analyzed. Although a different geometry is studied, this work is insightful because the conclusions are qualitatively the same as for our amplifier: the small signal gain coefficient has to be kept relatively small in order for gL not to become too large in the transversal direction, in which case a strong depopulation of the upper laser level may occur. In the case of the crystals used in the second amplifier, the transversal dimension is 16 mm and the amplifying beam travels ~ 11 mm through the gain in each pass (the crystals are 5.5 mm thick and are used in an active mirror configuration as described in section 2.2.4). For these dimensions, when the single pass gain for the amplifying beam is about 3, the single pass gain for the photons emitted in the transverse direction is close to 5 if a flat-top profile is assumed for the pump beam. Above this value, the single

pass gain stops growing linearly with pump power as predicted by simulations and confirmed experimentally.

Going back to the amplification of the pulses coming from the regenerative amplifier, the energy is increased to about 100 mJ in the first four passes with an 8 mm beam. Then the beam is expanded to 16 mm to match the size of the pump beams and in eight additional passes the energy per pulse is increased to the Joule-level, as can be observed in fig. 2.26. For the maximum pump power the shot to shot variation in energy was in the order of 5 %. The instabilities arise mostly from a redistribution of the energy on the beam profile caused by air flow in the path of the beam affecting the wavefront, and this in turn, affects the way the energy is extracted. Another significant contribution to a change in the output energy comes from the fact that when the nitrogen starts boiling, it cools down the upper part of the dewar, inducing thermo-mechanical deformations in the chamber that affect the alignment of the crystals, and therefore of the whole amplification stage. This does not affect the shot to shot stability, but introduces a drift in time in the output energy.

The repetition rate in these measurements was 10 Hz. Although no thermal lensing or thermally induced depolarization were observed at repetition rates as high as 50 Hz, the output energy of the amplifier is significantly reduced. The cause of this effect is an overall heating of the gain material and therefore a drop in the stimulated emission cross section that has a strong dependence upon tem-

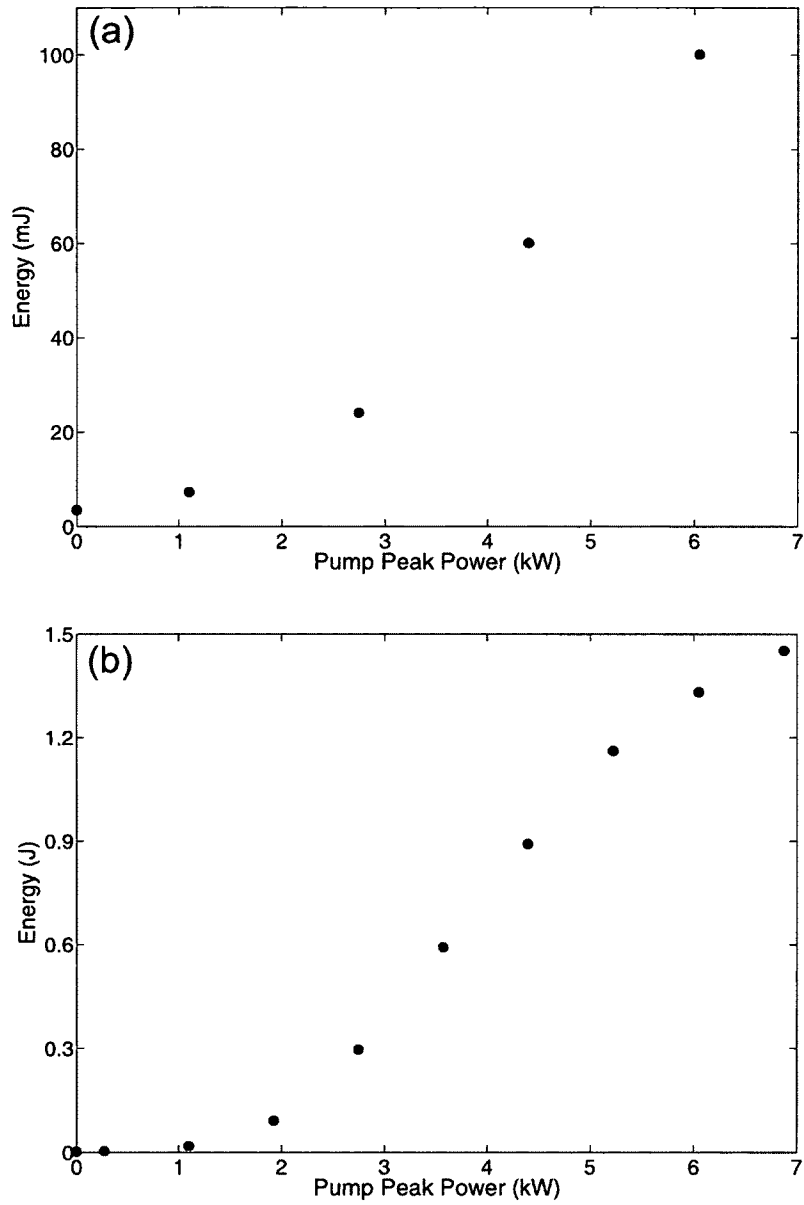


Figure 2.26: (a) Energy as a function of peak pump power for the 4-pass configuration with a small beam. (b) Energy for the 12-pass configuration

perature around liquid nitrogen temperature. As a consequence the single pass gain is reduced and the extracted energy is lower. Thermal simulations show only a slight temperature increase in the gain region at 50 Hz (~ 10 K). However, these simulations assume a perfect thermal contact between the copper and the Yb:YAG crystals.

As it was mentioned in section 2.2.4 the thermal contact between the copper and the laser crystals is enhanced by a malleable layer of indium. However, in order to maximize the contact, a considerably high pressure has to be applied on the crystal. If the applied pressure on the crystals is excessive, the induced mechanical stress can deform the wavefront of the amplified beam and introduce depolarization losses. Fig. 2.27 illustrates the wavefront distortions in the beam coming out of the second amplification stage.

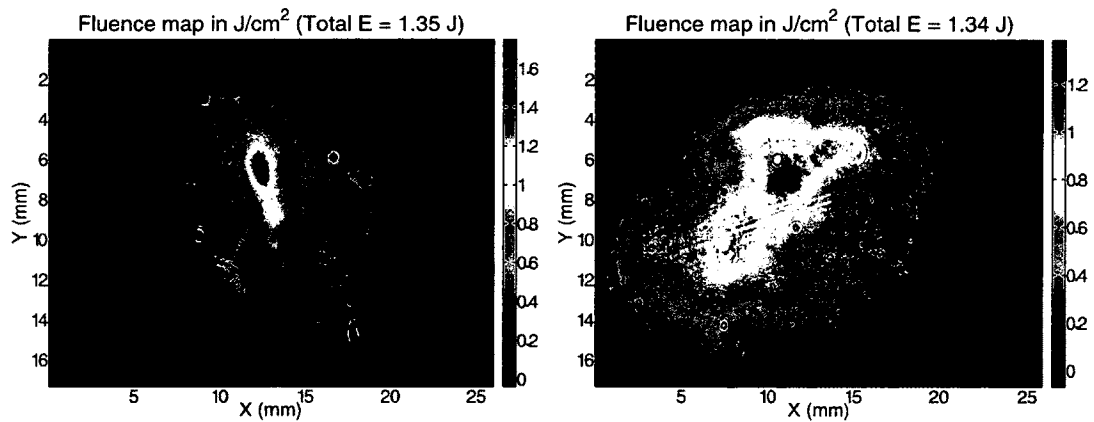


Figure 2.27: Fluence maps for two beams with more than 1.3 J of energy and slightly different alignment through the amplifier. (a) All the energy is in the plasma heating pulse. (b) About 40 % of the energy is in the main pre-pulse

The wavefront distortions degrade the beam quality affecting the way the beam propagates and focuses, which in turn affects the quality of the line focus for the soft x-ray laser (see fig. 3.2 in section 3.1). Distortions in the wavefront can also create regions of higher fluence in the beam as this propagates. In particular, regions with higher fluence extract energy more efficiently from the amplification medium and amplify at a faster rate. In principle, these hot spots should saturate the gain material, stop extracting energy and at the most, create an inhomogeneous beam profile. However, since we are working close to the threshold for nonlinear effects (an estimation of the B -integral yields a value of 2.3), other effects such as self focusing may arise. Nevertheless, splitting of the total energy between the pre-pulses and the plasma heating pulse reduced the nonlinear effects to an acceptable level (see fig. 2.27 (b)). The beam quality was closely monitored at all times with cameras located in different parts of the second amplification stage.

The B -integral can be reduced by reducing the intensity of the pulses, reducing the amount of material in the amplifier, or both. One way to reduce the amount of material is to pump harder, increase the single pass gain and saturate the amplifier in less passes. In particular, for our multi-pass amplifier, the 12-passes could be reduced to an 8-pass configuration. The other approach to minimize the nonlinear effects is to reduce the intensity of the amplifying beam. In principle this could be done by increasing the beam size in the amplifier. The drawback of this is that the gain per pass would be reduced and more passes through the amplifier would

be needed, going in the opposite direction of the first mentioned idea. However, the intensity can still be reduced without affecting the beam size by stretching the pulse duration. Since the duration of stretched pulses is directly proportional to the spectral bandwidth of the pulses [23], increasing the bandwidth would reduce the intensity and hence the B -integral. The main source of bandwidth reduction in the CPA system is the gain narrowing process taking place in the regenerative amplifier. A possible solution is to increase the operating temperature in this amplifier to increase the gain bandwidth and reduce the gain narrowing. In fact, by measuring the bandwidth of the amplified pulses coming out of the regenerative amplifier as a function of the operating temperature, it was observed that the bandwidth increases a factor of 1.5 when the temperature is increased from 106 K to 180 K. Assuming that the stretched pulse width is increased by the same factor, a new calculation of the B -integral for the 12-pass amplifier yields a value of 1.5 with 300 ps stretched pulses, compared to 2.3 with 200 ps pulses. Moreover, combining 300 ps stretched pulses with an 8-pass amplifier design, the B -integral could be reduced down to ~ 0.8 , when the output energy is 1.8 J (these numbers are based on preliminary results with a new amplifier design).

In spite of these limitations the quality of the beam was reasonably good to make a line focus on the target chamber and try to observe for the first time, amplification of soft x-ray photons with an all diode-pumped laser driver. Operating at a repetition rate of 10 Hz and with an efficiency of 70 % in the compressor

as described before, the combined pulse energy incident on the target chamber reached 1 J. The pulses with negative GDD were further stretched to 350 ps. The bandwidth of the amplified pulses can support sub-10 ps pulse durations. The pulses with positive GDD were compressed down to (8.5 ± 0.5) ps as can be seen from the autocorrelation trace of fig. 2.28. By blocking the seed pulses going to the

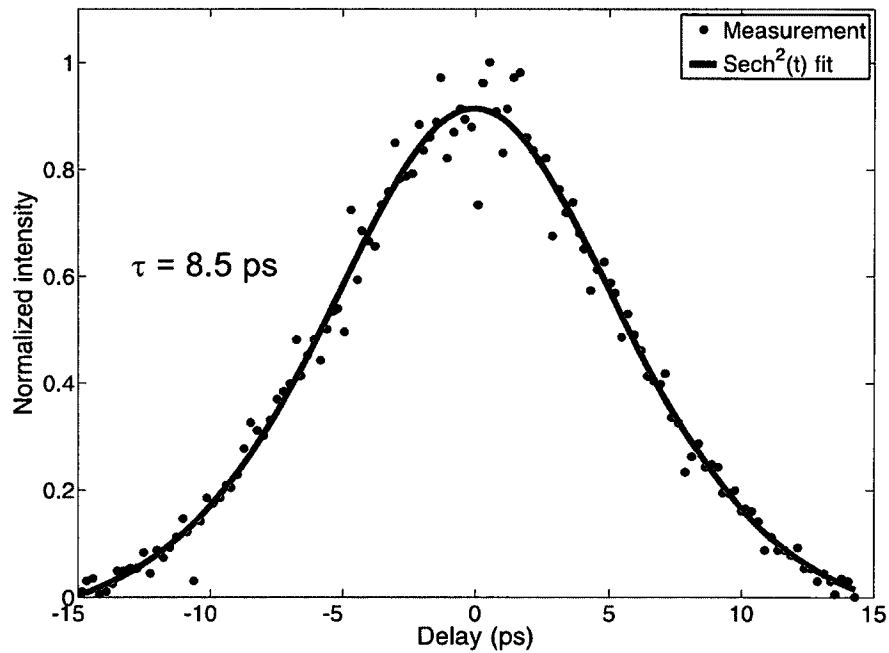


Figure 2.28: Hyperbolic secant square fit of the autocorrelation data corresponding to a pulse duration of 8.5 ps FWHM

negative GDD stretcher all the energy was sent to the short pulse and therefore we were able to generate, after the compressor, pulses with 1 J of energy and 8.5

ps duration, which is the highest energy reported to date for sub-10 ps pulses from an all diode-pumped system.

Bibliography

- [1] T. Y. Fan, D. J. Ripin, R. L. Aggarwal, J. R. Ochoa, B. Chann, M. Tillerman, and J. Spitzberz. Cryogenic Yb³⁺-doped solid state lasers. *IEEE Journal of Selected Topics in Quantum Electronics*, 13(3):448–459, 2007.
- [2] Jun Dong, Michael Bass, Yanli Mao, Peizhen Deng, and Fuxi Gan. Dependence of the Yb³⁺ emission cross section and lifetime on temperature and concentration in yttrium aluminum garnet. *J. Opt. Soc. Am. B*, 20(9):1975–1979, 2003.
- [3] Shinji Ito, Terunobu Nakajyo, Tatsuya Yanagida, Fumio Sakai, Akira Endo, and Kenji Torizuka. Diode-pumped, chirped-pulse Yb:S-FAP regenerative amplifier for laser-compton x-ray generation. *Optics Communications*, 259(2):812 – 815, 2006.
- [4] Frédéric Druon, Francois Balembois, Patrick Georges, Alain Brun, Seung-Whan Bahk, John Nees, Gérard Mourou, Gilles Chériaux, Jean-Paul Chambaret, Gérard Aka, and Daniel Vivien. 12-mJ, 350-fs Yb:GdCOB regenerative amplifier. *Optics Communications*, 199(1-4):181 – 187, 2001.

- [5] K. Ogawa, Y. Akahane, M. Aoyama, K. Tsuji, S. Tokita, J. Kawanaka, H. Nishioka, and K. Yamakawa. Multi-millijoule, diode-pumped, cryogenically-cooled Yb:KY(WO₄)₂ chirped-pulse regenerative amplifier. *Opt. Express*, 15(14):8598–8602, 2007.
- [6] H. Liu, J. Nees, G. Mourou, S. Biswal, G. J. Spühler, U. Keller, and N. V. Kuleshov. Yb:KGd(WO₄)₂ chirped-pulse regenerative amplifiers. *Optics Communications*, 203(3-6):315 – 321, 2002.
- [7] Junji Kawanaka, Koichi Yamakawa, Hajime Nishioka, and Ken ichi Ueda. 30-mJ, diode-pumped, chirped-pulse Yb:YLF regenerative amplifier. *Opt. Lett.*, 28(21):2121–2123, 2003.
- [8] N. V. Kuleshov, A. A. Lagatsky, A. V. Podlipensky, V. P. Mikhailov, and G. Huber. Pulsed laser operation of Yb-doped KY(WO₄)₂ and KGd(WO₄)₂. *Opt. Lett.*, 22(17):1317–1319, 1997.
- [9] Sébastien Chénais, Frédéric Druon, Sébastien Forget, Francois Balembois, and Patrick Georges. On thermal effects in solid-state lasers: The case of ytterbium-doped materials. *Progress in Quantum Electronics*, 30(4):89 – 153, 2006.
- [10] C. Bowness. Liquid cooled solid state lasers, 1967. US patent 3339150.
- [11] D. H. McMahon. Colling system for laser media, 1972. US patent 3676798.

- [12] P. A. Schulz and S. R. Henion. Liquid-nitrogen-cooled Ti:Al₂O₃ laser. *IEEE Journal of Quantum Electronics*, 27(4):1039–1047, 1991.
- [13] P. F. Moulton. Spectroscopic and laser characteristics of Ti:Al₂O₃. *J. Opt. Soc. Am. B*, 3(1):125–133, 1986.
- [14] Sterling Backus, Charles G. Durfee III, Gérard Mourou, Henry C. Kapteyn, and Margaret M. Murnane. 0.2-TW laser system at 1 kHz. *Opt. Lett.*, 22(16):1256–1258, 1997.
- [15] Sterling Backus, Randy Bartels, Sarah Thompson, Robert Dollinger, Henry C. Kapteyn, and Margaret M. Murnane. High-efficiency, single-stage 7-kHz high-average-power ultrafast laser system. *Opt. Lett.*, 26(7):465–467, 2001.
- [16] Rosalind Wynne, John L. Daneu, and Tso Yee Fan. Thermal coefficients of the expansion and refractive index in YAG. *Appl. Opt.*, 38(15):3282–3284, 1999.
- [17] Tso Yee Fan and John L. Daneu. Thermal coefficients of the optical path length and refractive index in YAG. *Appl. Opt.*, 37(9):1635–1637, 1998.
- [18] D. C. Brown. The promise of cryogenic solid state lasers. *IEEE Journal of Selected Topics in Quantum Electronics*, 11(3):587–599, 2005.
- [19] D. C. Brown. Nonlinear thermal distortion in YAG rod amplifiers. *IEEE Journal of Quantum Electronics*, 34(12):2383–2392, 1998.

- [20] D. C. Brown. Ultrahigh-average-power diode-pumped Nd:YAG and Yb:YAG lasers. *IEEE Journal of Quantum Electronics*, 33(5):861–873, 1997.
- [21] Glen A. Slack and D. W. Oliver. Thermal conductivity of garnets and phonon scattering by rare-earth ions. *Phys. Rev. B*, 4(2):592–609, Jul 1971.
- [22] Walter Koechner. *Solid-state laser engineering*. Springer, 2006.
- [23] E. B. Treacy. Optical pulse compression with diffraction gratings. *Quantum Electronics, IEEE Journal of*, 5(9):454–458, 1969.
- [24] D. C. Brown, R. L. Cone, Y. Sun, and R. W. Equall. Yb:YAG absorption at ambient and cryogenic temperatures. *IEEE Journal of Selected Topics in Quantum Electronics*, 11(3):604–612, 2005.
- [25] Hiroaki Furuse, Junji Kawanaka, Kenji Takeshita, Noriaki Miyanaga, Taku Saiki, Kazuo Imasaki, Masayuki Fujita, and Shinya Ishii. Total-reflection active-mirror laser with cryogenic Yb:YAG ceramics. *Opt. Lett.*, 34(21):3439–3441, 2009.
- [26] D. J. Ripin, J. R. Ochoa, R. L. Aggarwal, and T. Y. Fan. 300-W Cryogenically Cooled Yb:YAG Laser. *IEEE Journal of Quantum Electronics*, 41(10):1274–1277, 2005.
- [27] J. Aus der Au, G. J. Spühler, T. Südmeyer, R. Paschotta, R. Hövel, M. Moser, S. Erhard, M. Karszewski, A. Giesen, and U. Keller. 16.2-W average power

- from a diode-pumped femtosecond Yb:YAG thin disk laser. *Opt. Lett.*, 25(11):859–861, 2000.
- [28] A. Giesen and J. Speiser. Fifteen years of work on thin-disk lasers: results and scaling laws. *IEEE Journal of Selected Topics in Quantum Electronics*, 13(3):598–609, 2007.
- [29] Stuart Pearce, Ryo Yasuhara, Akira Yoshida, Junji Kawanaka, Toshiyuki Kawashima, and Hirofumi Kan. Efficient generation of 200mJ nanosecond pulses at 100Hz repetition rate from a cryogenic cooled Yb:YAG MOPA system. *Optics Communications*, 282(11):2199 – 2203, 2009.
- [30] C. Wandt, S. Klingebiel, R. Hrlein, I. Ahmad, T. Wang, S. Trushin, Z. Major, M. Siebold, J. Hein, F. Krausz, and S. Karsch. High-energy, diode-pumped CPA to the Joule-level based on Yb-doped materials. In *Advanced in Solid State Photonics 2009*, page WA4, 2009.
- [31] J. Tümmler, R. Jung, H. Stiel, P. V. Nickles, and W. Sandner. High-repetition-rate chirped-pulse-amplification thin-disk laser system with joule-level pulse energy. *Opt. Lett.*, 34(9):1378–1380, 2009.
- [32] Kyung-Han Hong, Juliet Gopinath, Darren Rand, Aleem Siddiqui, Shu-Wei Huang, Enbang Li, Benjamin Eggleton, John Hybl, Tso Yee Fan, and Franz X. Krtner. Generation of 2-kHz, 40-mJ picosecond pulses from a cryogenic

Yb:YAG chirped-pulse amplifier for OPCPA pumping. In *Advanced in Solid State Photonics 2010*, page APDP1, 2010.

- [33] Simon Rivier, Valentin Petrov, Andreas Gross, Sophie Vernay, Volker Wesemann, Daniel Rytz, and Uwe Griebner. Segmented grown Yb:KY(WO₄)₂/KY(WO₄)₂ for use in continuous-wave and mode-locked lasers. *Opt. Express*, 15(24):16279–16284, 2007.
- [34] Peter Klopp, Valentin Petrov, Uwe Griebner, and Goetz Erbert. Passively mode-locked Yb:KYW laser pumped by a tapered diode laser. *Opt. Express*, 10(2):108–113, 2002.
- [35] R. L. Fork, O. E. Martinez, and J. P. Gordon. Negative dispersion using pairs of prisms. *Opt. Lett.*, 9(5):150–152, 1984.
- [36] F. X. Kärtner and U. Keller. Stabilization of solitonlike pulses with a slow saturable absorber. *Opt. Lett.*, 20(1):16–18, 1995.
- [37] Franz X. Kärtner, Luigi R. Brovelli, Daniel Kopf, Markus Kamp, Irio G. Calasso, and Ursula Keller. Control of solid state laser dynamics by semiconductor devices. *Optical Engineering*, 34(7):2024–2036, 1995.
- [38] A. P. Kovács, K. Osvay, Zs. Bor, and R. Szipöcs. Group-delay measurement on laser mirrors by spectrally resolved white-light interferometry. *Opt. Lett.*, 20(7):788–790, 1995.

- [39] D. Strickland and G. Mourou. Compression of amplified chirped optical pulses. *Optics Communications*, 55:447–449, 1985.
- [40] O. Martinez. Design of high-power ultrashort pulse amplifiers by expansion and recompression. *IEEE Journal of Quantum Electronics*, 23(8):1385–1387, Aug 1987.
- [41] O. Martinez. 3000 times grating compressor with positive group velocity dispersion: application to fiber compensation in 1.3-1.6 μm region. *IEEE Journal of Quantum Electronics*, 23(1):59–64, 1987.
- [42] Ming Lai, Shui T. Lai, and Casimir Swinger. Single-grating laser pulse stretcher and compressor. *Appl. Opt.*, 33(30):6985–6987, 1994.
- [43] A. E. Siegman. *Lasers*. Springer, 1990. Chapter 10.
- [44] D. C. Brown, R. L. Cone, Y. Sun, and R. W. Equall. Yb:YAG absorption at ambient and cryogenic temperatures. *IEEE Journal of Selected Topics in Quantum Electronics*, 11(3):604–612, 2005.
- [45] D. Albach, J.-C. Chanteloup, and G. le. Touzé. Influence of ASE on the gain distribution in large size, high gain Yb³⁺:YAG slabs. *Opt. Express*, 17(5):3792–3801, 2009.

Chapter 3

**DEMONSTRATION OF AN ALL
DIODE-PUMPED SOFT X-RAY LASER**

In this chapter the experimental set up for the soft x-ray laser is described. The all diode-pumped CPA laser system described in chapter 2 is the pump laser for the soft x-ray laser. This system was successfully employed to demonstrate lasing in the 18.9 nm line of Ni-like molybdenum, constituting the first demonstration of an all diode-pumped soft x-ray laser. These results are presented in section 3.3.

3.1 Set up for soft x-ray laser: Focusing chamber and target chamber

The output of the CPA system (output of the compressor chamber) is connected to the input of the focusing chamber. The focusing chamber and the target chamber are dedicated exclusively to the generation of the soft x-ray laser. In the focusing chamber the amplified beam is reshaped using an optical arrangement comprising a cylindrical lens and five mirrors, one cylindrical mirror and four fold mirrors. This optical system is designed to make a line focus of 30 μm width by 3-5 mm long when incident on the target at ~ 29 degrees with respect to the plane of the target. Fig. 3.1 shows a sketch of the focusing chamber. The cylindrical lens has a focal length of 2 m and focuses the beam horizontally such that the length of the line formed on the target is ~ 4 mm. This length can be changed by moving the lens along the path of the beam. The cylindrical mirror, with a radius of 940 mm focuses the beam vertically. The beam angle of incidence on the mirror is the same as the angle of incidence on the target. In that way the beam is focused along

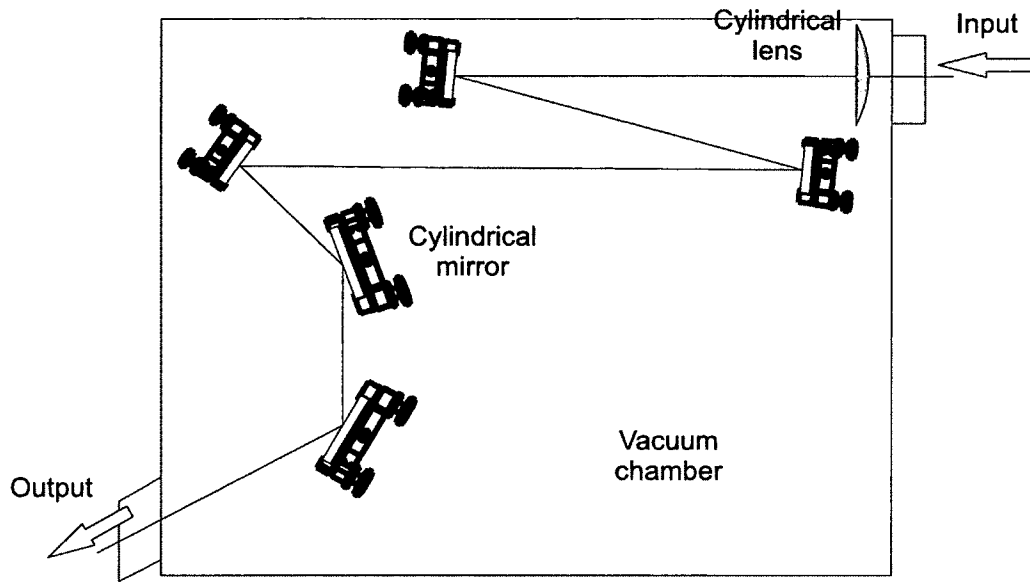


Figure 3.1: Schematic of the focusing chamber

the plane of the target, creating a line with uniform width on the target. With a diffraction limited beam the optical arrangement is design to focus down to a FWHM of $30 \mu\text{m}$. However, the wavefront distortions introduced by imperfections in the optics make the width of the line slightly wider. As a consequence of this the intensity of the driver laser on the target is lower and the required energy per pulse to create the proper plasma conditions increases. Also, the line can be further degraded after amplification in the second amplification stage. These wavefront degradations may introduce other unwanted effects such as line bending which, effectively reduces the length of the soft x-ray gain medium. Fig. 3.2 shows two images of the line focus taken by placing a camera in the position of the target. The image on fig. 3.2 (a) was taken replacing the laser crystals by flat mirrors ($\lambda/4$

at 633 nm) in the second amplification stage. The image on fig. 3.2 (b) illustrates the degradation introduced by the laser crystals on the wavefront and the effect on the line focus.

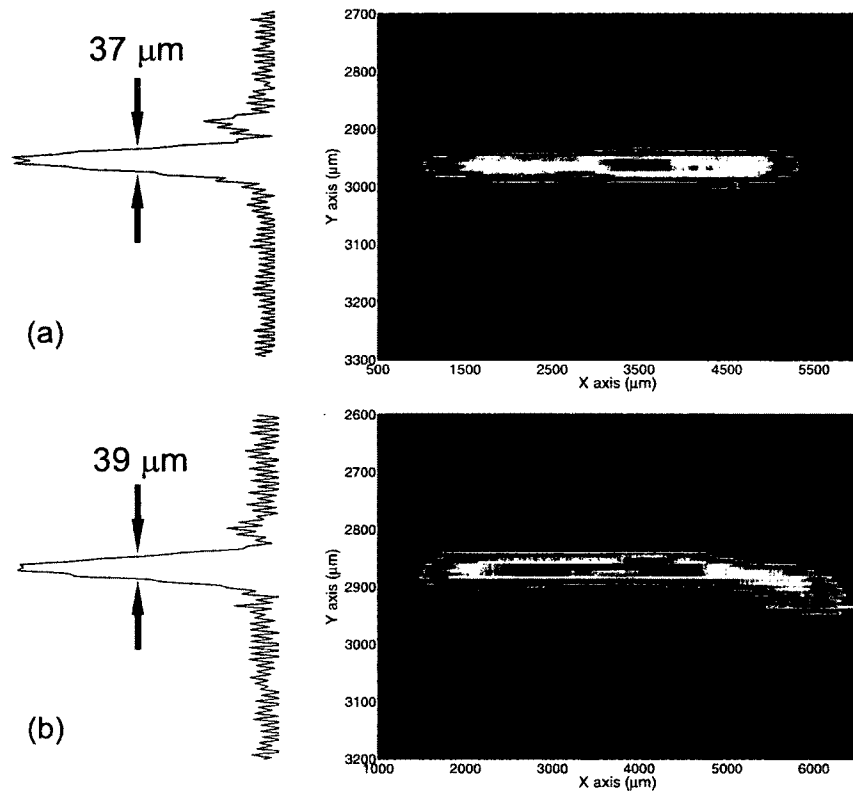


Figure 3.2: (a) Image of the line focus replacing the laser crystals in the second amplification stage by flat mirrors. (b) Line focus after propagating the beam through the actual system

In the target chamber the set of collinear pulses (pre-pulses and plasma heating pulse) is focused into a line at a grazing incidence angle of 29 degrees on a 4 mm wide polished target. The target material can be changed according to which

laser transition one wants to excite. For instance, with a molybdenum target it is possible to generate a soft x-ray laser at 18.9 nm, and using a silver target, a lasing wavelength of 13.9 nm can be generated. The axial soft x-ray plasma emission is analyzed using a spectrometer made with a 1200 lines/mm variable space grating (Hitachi 011-0437) and a back-thinned CCD (ANDOR Technology Model No: DO436-BN) placed on the image plane. Fig. 3.3 shows a sketch of the target chamber and a picture of a molybdenum stripe target.

Aluminum or zirconium filters are placed in between the target and the grating to block the visible light emitted by the plasma and to protect the grating and the CCD from plasma debris. Stainless steel shields are also placed inside the chamber to block the plasma debris. The target assembly is mounted on motorized stages that can be controlled from the exterior of the vacuum chamber. This allows to control the position of the target with respect to the pump beam during the experiment.

To align the target and the spectrometer two He-Ne laser beams are used. One beam is sent along a line parallel to the plane of the optical table and perpendicular to the supposed direction of the soft x-ray laser beam. This He-Ne laser beam reflects off the target surface and by sending the reflection back on itself, the normal of the target is placed perpendicular to the expected direction of the soft x-ray laser beam (neglecting refraction effects in the plasma). The second beam is sent parallel to the plane of the table and to the plane of the target. This

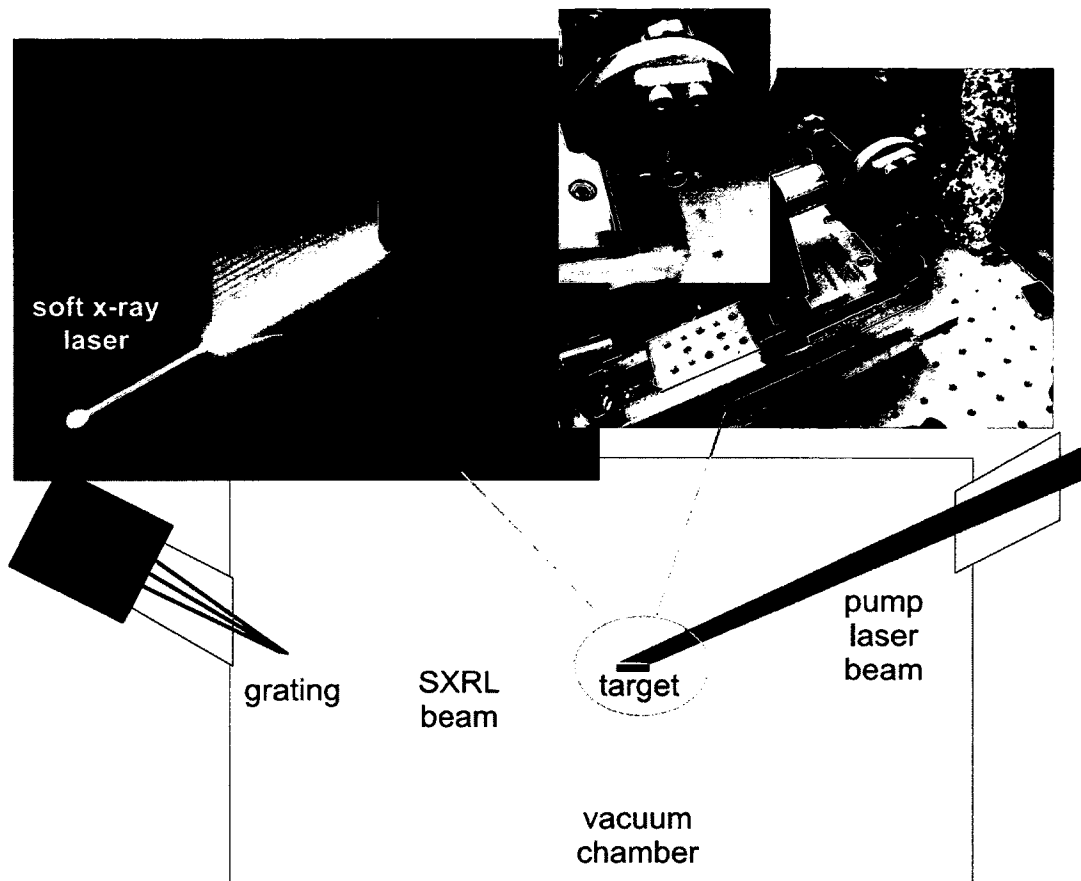


Figure 3.3: Schematic of the target chamber including an artistic illustration of the soft x-ray laser and photographs of a slab target

beam emulates the propagation of the soft x-ray laser beam (again, neglecting refraction effects in the plasma) and it is used to align the spectrometer. Working at a grazing incidence angle of ~ 3 degrees on the substrate of the grating it is possible to make an image with a magnification very close to 1 in the horizontal direction. The distances to the object and to the image plane are ~ 25 cm and ~ 23 cm respectively. Using the zero order of the grating to reflect the reference

beam, the path of the zero order soft x-ray beam can be determined. Using that and the grating equation, the path of the first diffraction order for the required laser wavelength can be estimated, and the CCD can be placed in order to capture the first diffraction order. Additionally, the zero order of the grating is blocked. The CCD is mounted on an X-Y stage and it is connected to the vacuum chamber through a bellow, so that the position of the detector can be adjusted to find the image plane and the optimum position with respect to the plasma spectral lines.

A slab target is very useful to analyze the performance of the soft x-ray laser and find the optimum set of lasing parameters. However, in order to make the laser more practical in high repetition rate applications a helicoidal target was built that can provide hours of operation at high repetition rates (> 10 Hz). The

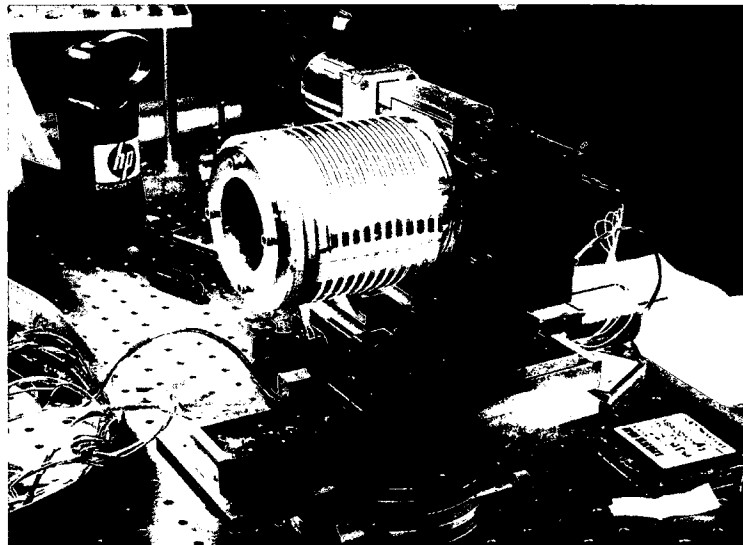


Figure 3.4: Picture of a helicoidal target

helical target is shown in fig. 3.4. The target advances and the helicoid moves so that the driver laser always hits a new target area.

3.2 Simulations

The characteristics of the line focus, pulse duration and energy per pulse described previously were used as feed parameters for a 1.5-D Hydrodynamical plasma model developed by Mark Berril at Colorado State University [1] to predict the temporal evolution of the plasma and gain formation. The simulations only take into account the existence of one pre-pulse and the short, or plasma heating pulse. As it was mentioned before, the pulse durations were fixed, being 350 ps FWHM for the pre-pulse and 8.5 ps FWHM for the short pulse. The experiment described in section 3.3 was run under the same conditions, and only the energy distribution between the set of pulses and the delay between them could be changed.

The characteristics of the line focus were incorporated into the simulations. The model needs as input parameters the length and width of the line focus. For this, the measured values from the images presented in section 3.1 were used. An effective length of 3.5 mm and a representative width of 39 μm were used to describe the line focus. The 1.5-D model assumes a perfectly straight line focus. However, it was estimated that because of the bending of the line on the plane of

the target (see fig 3.2 (b)) about 10 % of the energy is wasted. Therefore, only 90 % of the total measured energy in the infrared laser pulses was used as the input total energy for the simulations. In the experiments and simulations the target material was molybdenum. The Ni-like Mo $J = 0 \rightarrow 1$, $4p - 4d$ laser transition has a wavelength of 18.9 nm.

The output of the simulations is a set of data describing the plasma dynamics and the populations of the Ni-like levels from which the population inversion and small signal gain coefficient can be calculated as a function of distance from the target and time. Analyzing this information for different excitation conditions allows us to estimate the best experimental conditions for soft x-ray amplification. Fig. 3.5 shows maps of the small signal gain coefficient as a function of time and distance from the target for different delays between the pre-pulse and the short or plasma heating pulse. The delay is calculated from the peak of the pre-pulse to the peak of the short pulse. $t = 0$ corresponds to the arrival of the peak of the pre-pulse to the target. The total energy on target for these simulations was 900 mJ divided in 300 mJ in the pre-pulse and 600 mJ in the short pulse.

According to the simulations the maximum gain coefficient is achieved for a delay of 600 ps. However, the maximum single pass gain (gL product) and therefore the maximum output laser energy, may not be obtained for the conditions of maximum gain coefficient. It is important to remember here that the refraction effects are stronger closer to the target, where the electron density is higher, and

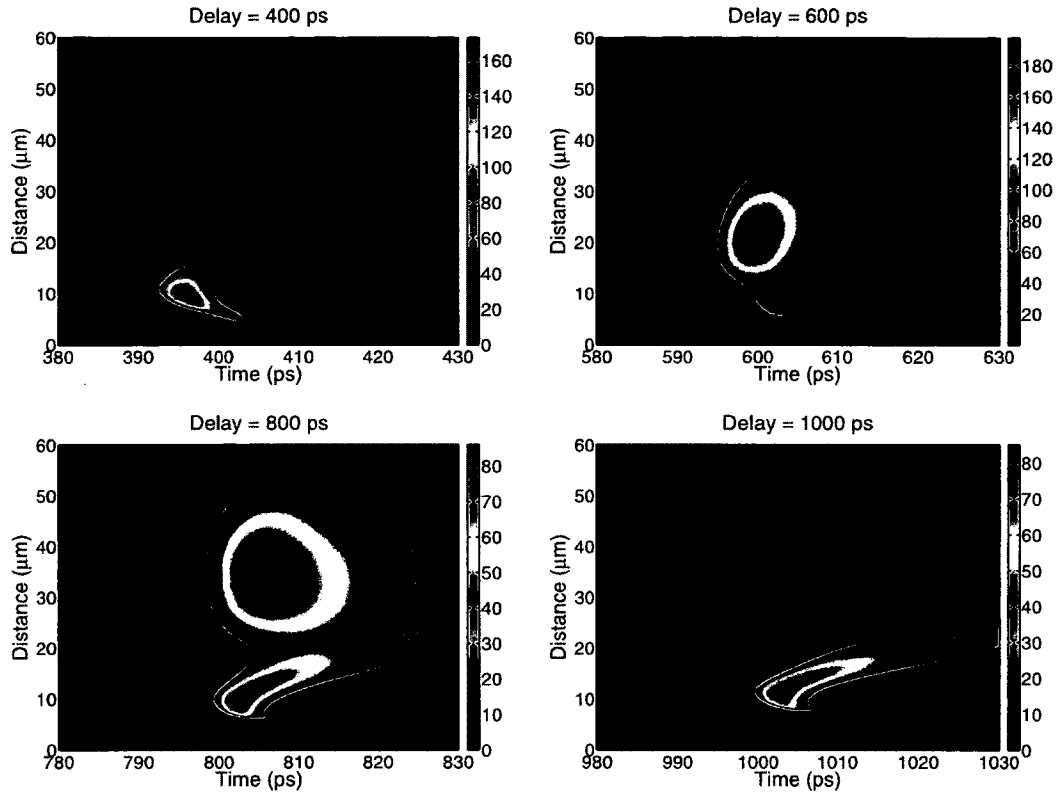


Figure 3.5: Maps of the small signal gain coefficient (cm^{-1}) as a function of time and distance from the target for different delays between the excitation pulses. The delay is calculated from the peak of the pre-pulse to the peak of the short pulse. $t = 0$ corresponds to the arrival of the pre-pulse to the target

the electron density gradients are stronger. In addition, the output energy of the soft x-ray laser depends also on the size and duration of the gain. This additional information is shown in fig. 3.6. Fig. 3.6 (a) shows the peak of the small signal gain coefficient as a function of the delay between the excitation pulses. In fig. 3.6 (b) the distance from the location of the maximum of the gain to the surface of the target is plotted for different delays and fig. 3.6 (c) shows the value of the electron

density at that position. Finally, fig. 3.6 (d) shows the duration of the gain for each case.

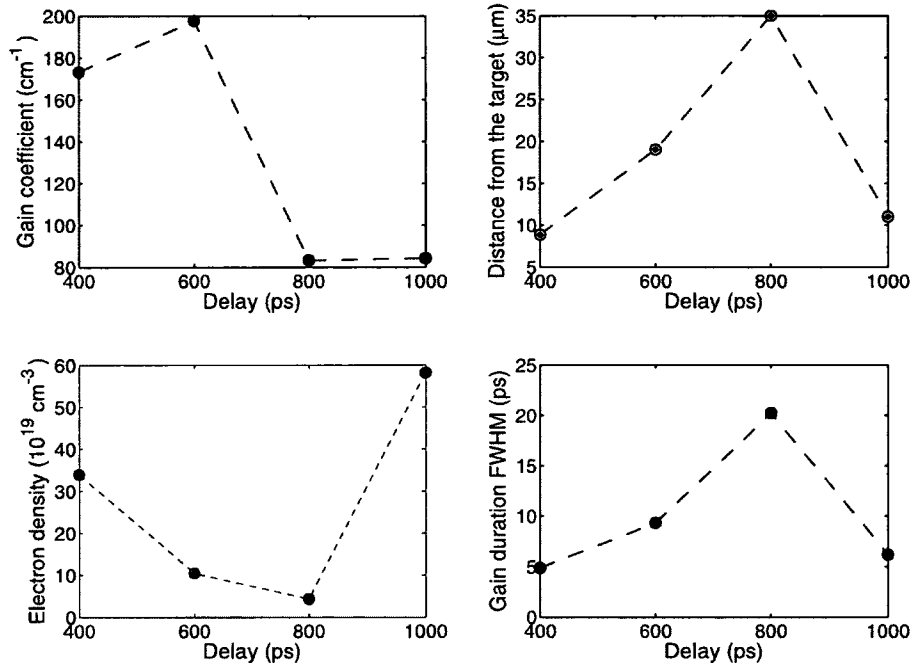


Figure 3.6: Different gain conditions created by changing the delay between the pre-pulse and the plasma heating pulse. (a) Maximum of the small signal gain coefficient. (b) Distance from the target to the position of the maximum. (c) Electron density at the position and time of the maximum gain coefficient. (d) FWHM duration of the gain

The results in fig. 3.5 and 3.6 show that for a delay of 800 ps the distance from the target to the maximum of the gain region is maximized. The size and duration of the gain region are maximized as well for this delay. The peak of the small signal gain coefficient is higher than 80 cm^{-1} , which for a gain medium length of 3.5 mm is sufficiently high to saturate the gain ($gL \sim 28$).

Qualitatively a delay of 800 ps between the pulses seems the most promising option. The same analysis may be carried out keeping the delay between the pulses fixed at 800 ps and changing the amount of energy in the pre-pulse. Again, the total energy is kept constant at 900 mJ. Maps of the small signal gain coefficient for different energy distributions between the excitation pulses are shown in fig. 3.7 and

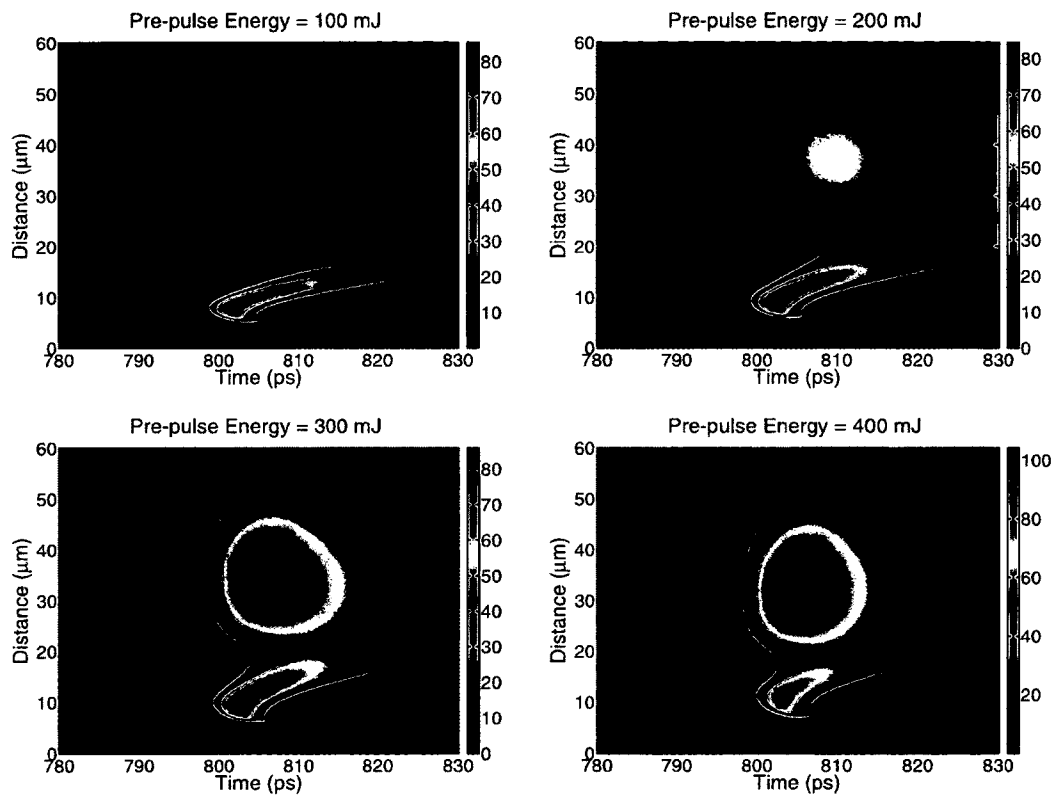


Figure 3.7: Maps of the small signal gain coefficient (cm^{-1}) as a function of time and distance from the target for different pre-pulse energies. In all cases the total energy incident on target was 900 mJ

fig 3.8 shows graphs of the maximum of the small signal gain coefficient, distance

from this maximum to the surface of the target, the electron density at this position and the duration of the gain, all as a function of energy in the pre-pulse.

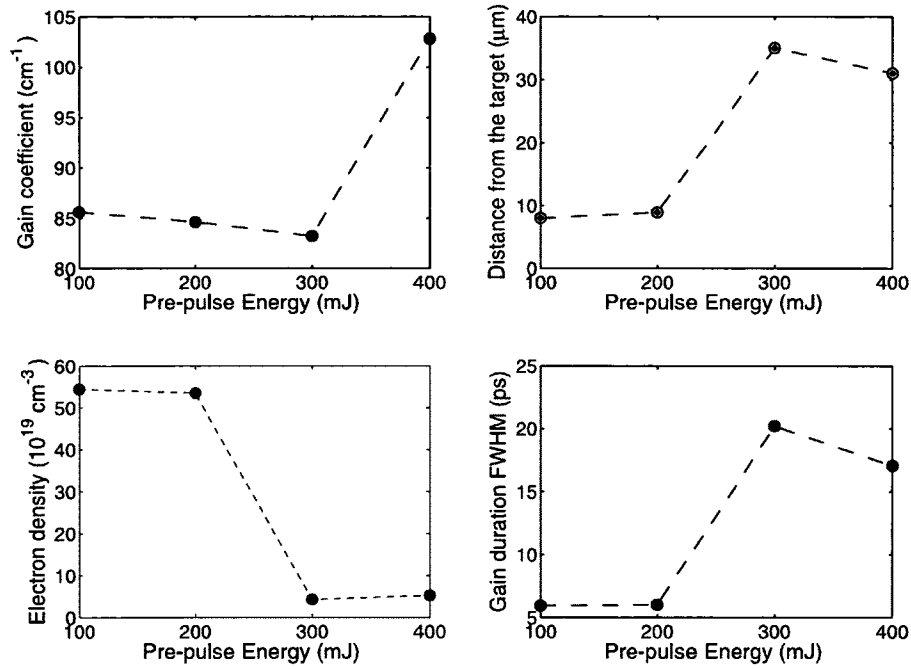


Figure 3.8: Different gain conditions created by changing the energy in the pre-pulse. (a) Maximum of the small signal gain coefficient. (b) Distance from the target to the position of the maximum. (c) Electron density at the position and time of the maximum gain coefficient. (d) FWHM duration of the gain. In all cases the total energy incident on target was 900 mJ

The maximum small signal gain coefficient is achieved if the energy is divided between 400 mJ in the pre-pulse and 500 mJ in the plasma heating pulse. The distance from the peak of the gain to the target is however, slightly smaller for the case with maximum gain coefficient than for the case where 300 mJ are sent to the pre-pulse. The gain region is slightly bigger for a pre-pulse energy of 300 mJ.

Nevertheless, at this point it is hard to say under which conditions the output energy of the soft x-ray laser would be higher. A more detailed analysis involving ray tracing to simulate the amplification process within the plasma is necessary. However, qualitatively we expect that, for the characteristics of our all diode-pumped optical driver laser, a time delay around 800 ps between the pulses and a pre-pulse energy between 300 mJ and 400 mJ are the optimum conditions for amplification in the 18.9 nm line of Ni-like Mo. For a pre-pulse energy of 300 mJ, a delay of 800 ps and a gain medium with a length of 3.5 mm, results of the post-processor ray tracing model developed by Mark Berrill [1] predict that a maximum output energy close to 1 μ J should be obtained (see fig. 3.9).

3.3 Demonstration of soft x-ray amplification with an all diode-pumped system

The experimental conditions under which amplification was observed were in good agreement with the simulated data of the previous subsection. The delay was varied between \sim 500 ps and 1.3 ns and the energy of the pre-pulse was changed between \sim 250 mJ and 400 mJ. The total energy on target was kept approximately constant between 900 mJ and 1 J, unless for measurements exploring the minimum amount of pump energy on target needed for amplification. The grazing incidence angle was kept constant at 29 deg. For this angle and a gain medium length of 3.5 mm the mismatch between the photon and the traveling excitation wave transit

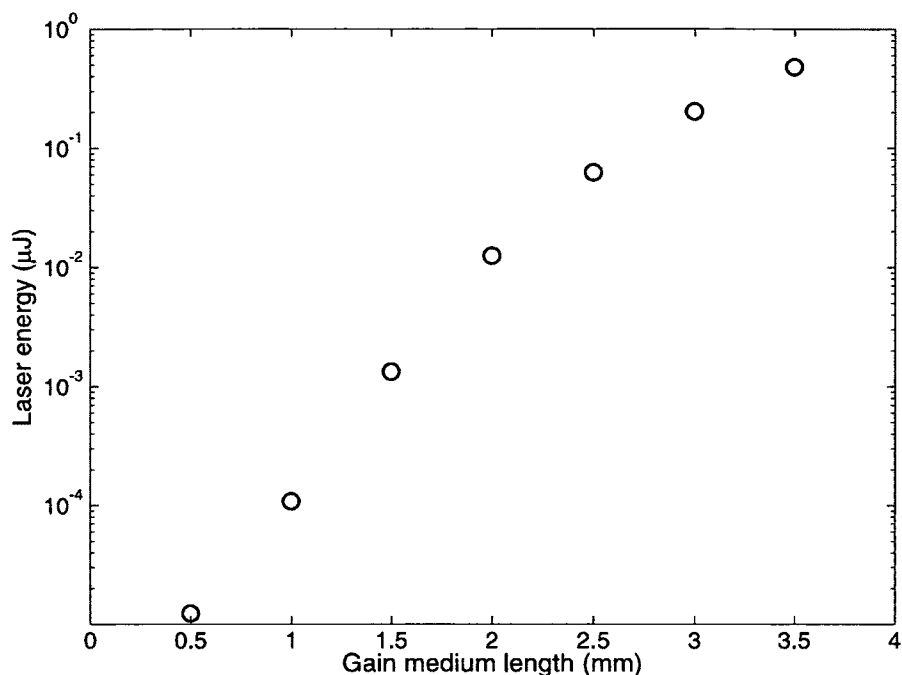


Figure 3.9: Simulated soft x-ray laser output energy as a function of the gain medium length for a delay of 800 ps between the excitation pulses and an energy of 300 mJ in the pre-pulse

times (see section 1.2.5 of Chapter 1) is on the order of 1 ps, much shorter than the duration of the gain calculated in the previous section and therefore negligible.

It was observed that a total energy on target higher than 700 mJ was necessary to observe amplification of the laser line. Fig. 3.10 shows a set of laser shots taken under the same conditions (delays and relative energies) as a function of total pump energy. In particular, these shots were taken with a delay of 850 ps between the main pre-pulse and the plasma heating pulse and 4 ns between the two pre-pulses. The first pre-pulse had $\sim 2\%$ of the total energy and the main pre-pulse had \sim

37 % of the total energy incident on target. From fig. 3.10 it can be seen how the number of counts on the laser line increases as a function of pump energy.

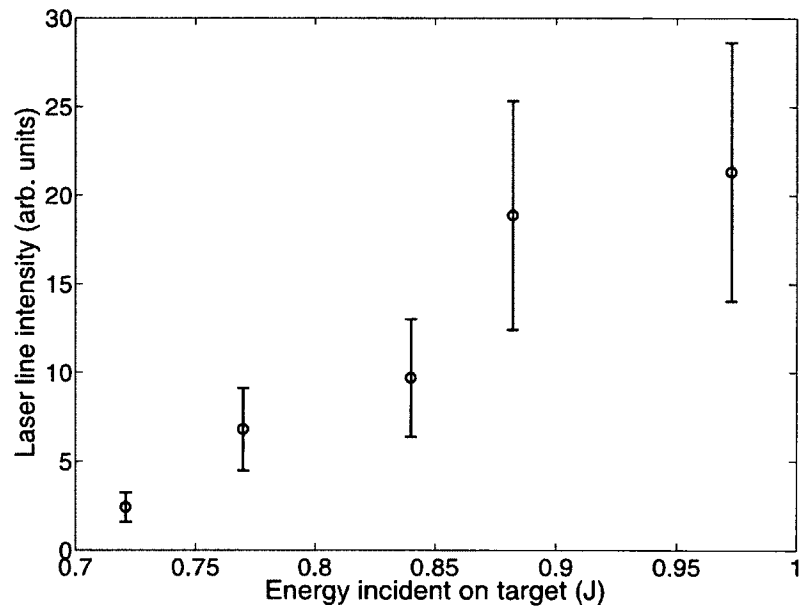


Figure 3.10: Integrated number of counts on the laser line as a function of pump energy incident on target. The error bars were estimated based on the shot to shot variation of the output of the soft x-ray laser

Fig. 3.11 shows two spectra taken with the x-ray CCD in which the total energy on target changes from 700 mJ to 940 mJ. In the case in which lasing is observed, the energy distribution and delays between the pulses were as follows: the first pre-pulse with 10 mJ of energy hit the target 4 ns before the main pre-pulse, which hit the target with 310 mJ. The rest of the energy, 620 mJ, was in the short pulse that hit the target 800 ps after the main pre-pulse. In this measurement

two $0.3 \mu\text{m}$ thick aluminum filters were used to block the visible light emitted by the plasma.

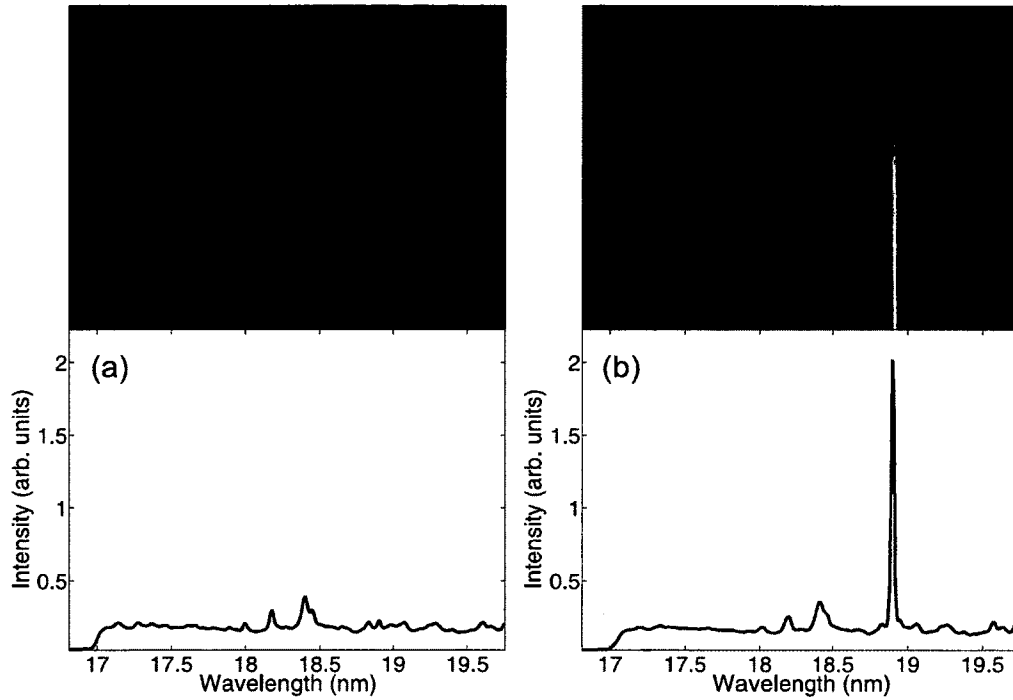


Figure 3.11: (a) On-axis soft x-ray spectrum taken with a total pump energy on target of 0.7 J. (b) The same spectrum taken with 0.94 J of pump energy, showing lasing in the 18.9 nm line of Ni-like Molybdenum

From fig. 3.11 the nonlinear growth of the 18.9 nm line of Ni-like Molybdenum with respect to the rest of the spectrum emitted by the plasma is clearly appreciated. Not only this dramatic growth in the intensity of the line is a clear proof of strong amplification, but also the fact that the divergence of the laser line is smaller than the divergence of the rest of the spectrum, as can be appreciated from fig. 3.11 (b). For this particular shot the output energy of the laser was

estimated to be 50 nJ and the divergence 15 mrad. To estimate the energy, the number of counts in the line read by the CCD were integrated over the whole line and then converted to number of incident photons, taking into account the filters transmittance and the CCD response.

The region in the parameter space where lasing was observed is in good agreement with the simulations of the previous section. The output energy observed experimentally is significantly smaller than the energy predicted by the model. A more careful description of the line focus combined with a 2-D model are necessary to better match the experimental conditions and the model.

The results presented in this section constitute the first demonstration of an all diode-pumped soft x-ray laser. Based on previous results in Ni-like molybdenum lasers [2,3] we expect that an optimization of the system (increased pump energy, quality of line focus, optimization of delays and relative energies and optimization of the grazing incidence angle) will lead to saturation of the laser line and to an increase of the output energy to 1-2 μJ and a decrease of the divergence to less than 10 mrad. Moreover, an improved thermal management in the CPA system will allow for higher repetition rate operation (50-100 Hz) and therefore to soft x-ray lasers with unsurpassed repetition rates.

Bibliography

- [1] M. Berrill. A computer model to simulate laser created plasmas used for the generation of extreme ultraviolet lasers. Master's thesis, Colorado State University, 2006.
- [2] B. M. Luther, Y. Wang, M. A. Larotonda, D. Alessi, M. Berrill, M. C. Marconi, J. J. Rocca, and V. N. Shlyaptsev. Saturated high-repetition-rate 18.9-nm tabletop laser in nickellike molybdenum. *Opt. Lett.*, 30(2):165–167, 2005.
- [3] M. A. Larotonda, B. M. Luther, Y. Wang, Y. Liu, D. Alessi, M. Berrill, A. Dummer, F. Brizuela, C. S. Menoni, M. C. Marconi, V. N. Shlyaptsev, J. Dunn, and J. J. Rocca. Characteristics of a saturated 18.9 nm tabletop laser operating at 5-hz repetition rate. *IEEE J. Sel. Topics Quantum Electron.*, 10(6):1363–1367, 2004.

Chapter 4

**PHOTOELECTRON SPECTROSCOPY FOR
DIELECTRIC THIN FILM
CHARACTERIZATION: A PROPOSED
EXPERIMENT**

Once the all diode-pumped soft x-ray laser is operating at its full potential many applications will benefit from its output characteristics. The increased repetition rate compared to currently operating soft x-ray lasers will offer higher average power and therefore better illumination conditions for soft x-ray imaging experiments. A great number of interesting nano-fabrication applications can be foreseen already. For instance, typically nano-fabrication with Talbot imaging [1] requires exposure times on the order of 5 minutes when the laser source is a 46.9 nm laser with an energy per pulse of $\sim 100 \mu\text{J}$ operating at 1 Hz. Extrapolating this to 50 Hz operation and $2 \mu\text{J}$ per pulse at 18.9 nm, the estimated exposure time is about the same. However the spatial resolution could be greatly improved.

In this chapter an idea for a new experiment is presented: the study of dielectric thin films using photoelectron spectroscopy. The soft x-ray laser is the source of photons for the photoelectric effect.

4.1 Motivations for photoelectron spectroscopy

Multilayer dielectric coatings are key components in any laser system. They are used for anti-reflection coatings in windows and lenses, high reflector coatings in mirrors, thin film polarizers, etc. The ability to control the coating performance with high accuracy is essential to improve laser performance by means of minimizing losses or controlling the optimum amount of light coupled out of a laser

cavity. For high peak power laser systems it is also extremely important to control the damage threshold and the stress on the substrate. Damage threshold of optical components limits the fluence at which an amplifier can operate. Let's recall from chapter 2 that the higher the fluence of an amplifying laser pulse, the higher the extraction efficiency from the gain medium. Deformations on the substrates induced by stress on the other hand, may deteriorate the wavefront quality. It is also important to minimize scattering and absorption losses in the the multilayer stack.

A typical multilayer coating combines a material with high index of refraction and one with low index [2]. SiO_2 is the most widely used low index material. For a high index material common choices are Ta_2O_5 , HfO_2 , TiO_2 and ZrO_2 . The characteristics of the coatings (damage threshold, stress, losses) change with deposition conditions and post deposition treatments such as annealing and also, for equal deposition conditions, the characteristics change from material to material.

In order to improve the performance of coatings it is necessary to optimize the deposition and post deposition conditions. A reasonable approach to do this is to study damage threshold, stress and losses for different deposition conditions on different materials. However, more insightful information, complementary to the mentioned studies, could be obtained from a structural analysis of the deposited material. In particular, damage threshold is influenced by surface processes and

therefore it would be very interesting to study the surface characteristics of the thin films in detail.

A wide spread method for surface characterization is photoelectron spectroscopy. This technique, based on the photoelectric effect, can provide information about the atomic species present and also the chemical bonding to their neighbors. The basic idea is that light characterized by photons with energy $\hbar\omega$ is incident on a sample, typically a gas or the surface of a solid and the free electrons emitted due to ionization of the sample (single photon ionization) are analyzed. From the kinetic energy of the electrons and their momentum, structural information of the sample may be obtained. Of course, the energy of the incident photons has to be higher than the binding energy of the electrons. The kinetic energy of the free electrons is then:

$$KE = \hbar\omega - \phi - |E_B| \quad (4.1)$$

where E_B is the binding energy and ϕ is the work function characteristic of the material. The binding energy is usually referred to the Fermi level in solids and to the vacuum level in free atoms or molecules [3]. Fig. 4.1 shows a schematic of the relation between the energy levels in a solid and the photoelectron kinetic energy distribution. Since the mean free path of electrons in solids in the kinetic energy range between 10 and 2000 eV is on the order of a few Å, any study of photoelectron emission will sample only electrons from a very thin layer close to

the surface [3]. Therefore, photoelectron spectroscopy is particularly suited for surface characterization.

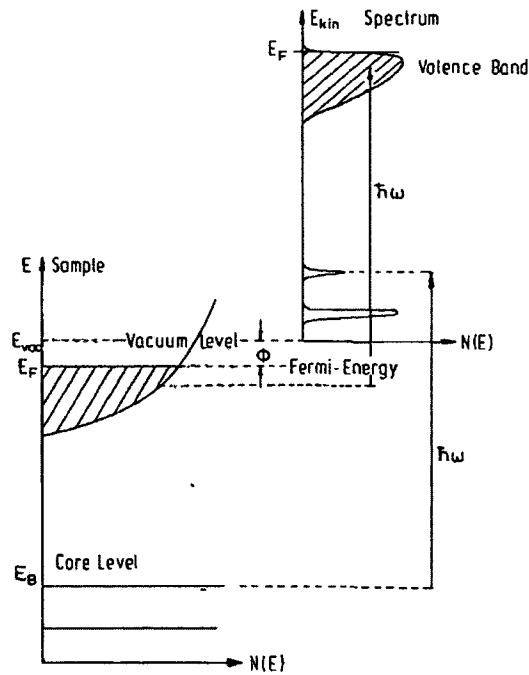


Figure 4.1: Schematics of the energy levels in a solid and their relation with the measured photoelectron kinetic energy. From ref. [3]

Photoelectron spectroscopy is then a very attractive technique to analyze structural information of dielectric thin films under different deposition conditions. It would be very interesting to investigate the correlation between the structural information and the damage threshold of the film. In addition, it would be interesting to analyze the presence of contamination and impurities on the sample and the relation between these and damage threshold. Also, it is noticed that

the damage threshold values for single shot experiments is higher than for multi-shot exposure experiments. Therefore it would be really interesting to analyze the structural information of the film before and after exposure of the sample to a high peak power laser pulse with a fluence very close to the single shot damage threshold. In fact, it is possible to think of time resolved experiments where a soft x-ray pulse (which generates the photoelectron effect) is incident on the sample at the same time as a high peak power infrared laser pulse does and study the photoelectron spectrum for different delays between the pulses. In this case, on top of the structural information of the film, the photoelectron spectrum would present additional peaks due to laser assisted photoelectric effect [4–6].

4.2 Experimental considerations

Several experimental requirements must be considered in order to estimate the feasibility of the proposed study. The most important in connection with this work are the soft x-ray source requirements, which we can divide in photon energy requirements and photon flux requirements.

The photon energy requirement is imposed by the binding energies of the materials to be studied. Most of the studies involving x-ray photoelectron spectroscopy have been carried out employing photon energies of a few keV given by K- α transitions such as Al K- α (1486.6 eV) or Mg K- α (1253.6 eV) [7]. However

this level of photon energies is only necessary to study deep core electrons in the atomic structure, which is not the intended purpose of this experiment. To obtain information about the composition and chemical bonds of the thin films a photon energy on the order of 100 eV is usually sufficient. This type of experiments has been done before utilizing synchrotron radiation with photon energies on the order of 130 eV (see for instance [8–10]). In particular, in ref. [9], structural properties of HfO₂ films deposited on Si substrates by atomic layer deposition were studied analyzing among other things, soft x-ray photoelectron spectra. The measured binding energies for Hf 4f electrons was on the order of 20 eV, while typical values for work functions are on the order of a few eV [3]. From these results it seems that the light produced by a Ni-like Cd soft x-ray laser emitting at 13.2 nm, with a photon energy of 93.9 eV is perfectly suited to study the composition of single layers of HfO₂ or TaO₂. Nevertheless, a higher photon energy would provide more flexibility in the experiment. For instance, some experiments studying SiO₂ deposited on Si substrates pay much attention to Si 2p electrons which according to ref. [10] have a binding energy of 99.3 eV for Si(111) and 103.7 eV for SiO₂. In that case, a Te target could be used in the soft x-ray laser to generate a lasing wavelength of 10.9 nm, or a photon energy of 113.8 eV. Table 4.1 gives some values for binding energies. Carbon is included since it is a common contaminant.

For binding energies of a few tens of eV the detected signal would be a convolution of peaks from different components (including information of valence band

Material	Energy level	Binding energy (eV)
Ta	4f	21.8
Ta in Ta ₂ O ₅	4f	26.8
Si	2p	99.3
Si on SiO ₂	2p	103.7
C	2s	19.39
O	2s	32.31
Hf	4f _{5/2}	15.9
Hf	4f _{7/2}	14.2
Hf in HfO ₂	4f _{5/2}	19.1
Hf in HfO ₂	4f _{7/2}	17.3
Ti	3s	58.7

Table 4.1: Binding energies for several elements/compounds (from ref. [9–13])

electrons). In principle however, it should be possible to deconvolute the individual signals and recover the information of the elements present on the sample.

The other major requirement to perform the proposed experiment is for the soft x-ray source to provide enough photon flux. The number of photons and the cross section of the process determine the number of photoelectrons generated and therefore, the signal level. The photon flux of the source is basically going to determine the exposure time of the experiment. A comparison with other experiments tells us that the photon flux of the soft x-ray laser should be sufficiently high to perform the experiments. In ref. [6], a high harmonic generation source is utilized to study laser assisted photoelectron effect on surfaces. This particular source, with a photon energy of 42 eV irradiates the sample with $\sim 10^6$ photons per pulse at a repetition rate of 2 kHz in a spot size in the order of 100 μm . This means a photon flux of 2×10^9 photons per second on the illuminated area. On

the other hand, the photon flux in a 13.2 nm Ni-like Cd laser operating at 50 Hz, with an energy per pulse of 1 μ J is approximately 6×10^{10} photons per pulse or 3×10^{12} photons per second. Assuming that ~ 50 % of the total radiation makes it to the sample due to losses in two Mo/Si multilayer mirrors, this photon flux still represents an improvement of about three orders of magnitude over the high harmonic generation source, and with a photon energy more than two times higher. However, for angle resolved measurements it is desirable to control the polarization of the soft x-ray source [14]. In that case, a soft x-ray polarized beam can be obtained by introducing 45 degrees mirrors that are polarization selective. It is worth mentioning that the photoionization cross section usually decreases about a factor of 10 for many atoms in the range from 50 eV to 100 eV [13].

From the previous estimations it seems reasonable to think that exposure times in photoelectron spectroscopy experiments could be reduced significantly by implementing a soft x-ray laser as the photon source. This opens the possibility to carry out scans over sample surfaces while keeping the duration of the experiment reasonably short. In that case the homogeneity of the thin films could also be studied for the particular application being proposed here. In fact, single shot experiments utilizing a Ni-like Pd soft x-ray laser at 14.7 nm have been realized [15, 16]. The photon flux incident on the sample in these experiments was on the order of 10^9 photons per pulse yielding about 10^4 photoelectrons per pulse on

the detector. The repetition rate of this soft x-ray laser was one shot every four minutes.

In addition, the bandwidth of the soft x-ray laser pulses is narrower than that of the high harmonics pulses. This implies an improvement on the resolution, since a well defined photon energy translates into a smaller uncertainty in the binding energy (see equation 4.1). For instance, in photoelectron spectroscopy experiments driven by high harmonic generation sources for which $\Delta\nu/\nu \sim 10^{-2}$, the resolution of the experiment is limited to ~ 100 meV. Typically for soft x-ray lasers $\Delta\nu/\nu \sim 10^{-4}$. If the photon energy is on the order of 100 eV the broadening in the kinetic energy of the photoelectrons due to the finite bandwidth of the photon source is in the order of 10 meV.

However, the resolution is also limited by space-charge effects. The Coulomb interaction between the electrons while they travel from the sample towards the detector broadens the width of the photoelectron spectrum and introduces a shift in the measured kinetic energy. The space charge effect depends on the number of electrons generated per pulse, the pulse duration, the size and shape of the excitation area and the energy distribution of the electrons [17]. Hellmann *et al* [18] simulated the space charge effect for a broad range of values of the number of electrons generated, the duration of the excitation pulse, the spot size and the mean value of the kinetic energy of the photoelectrons. The results of these simulations are in good agreement with reported experimental values and show

that the resolution is approximately proportional to N/d , with N the number of photoelectrons per pulse and d the FWHM diameter of the spot illuminated by the photon source. The energy shift has a similar behavior. Hellmann *et al* conclude that to keep the energy broadening below 50 meV, the number of photoelectrons per pulse divided by the spot size diameter has to be limited to $\sim 10^4$ electrons per pulse, per mm. Therefore, assuming a conversion efficiency like the one reported in ref. [16], it is reasonable to expect a resolution of ~ 50 meV when utilizing the all diode-pumped soft x-ray laser with a spot size on the sample with a diameter of 1 mm ¹.

The detection system for the proposed experiment could be a Time of Flight spectrometer (TOF), like the one utilized in ref. [4] for laser assisted photoelectron emission experiments. Fig. 4.2 shows the experimental setup of reference [4]. TOF spectrometers with resolutions in the meV range have been reported [19]. The detection system could be also a hemispherical electron energy analyzer. This is the type of device usually employed in angle resolved photoelectron spectroscopy (ARPES) experiments. For example, in ref. [20] a hemispherical energy analyzer combined with two micro-channel plates, a phosphor plate and CCD is employed to acquire information of the kinetic energy and momentum of the photoelectrons

¹Although the conversion efficiency depends upon material parameters such as the cross section and on the acceptance angle of the detection system, the numbers reported in ref. [16] give an idea of the order of magnitude that can be expected

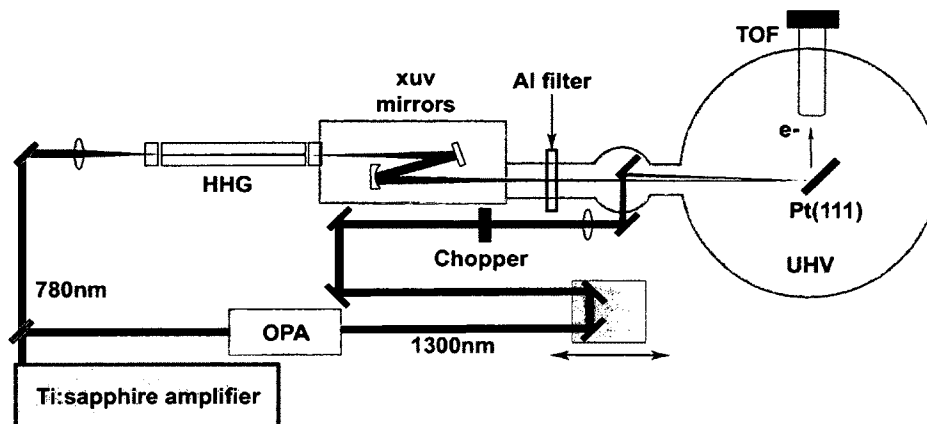


Figure 4.2: Experimental setup for laser assisted photoelectron spectroscopy. HHG stands for high harmonic generation, UHV for ultra high vacuum, OPA for optical parametric amplifier and TOF for time of flight spectrometer. From ref. [4]

simultaneously. These devices can operate with energy resolution of a few meV and angle resolution of 0.2 degrees.

As it was mentioned before, the resolution of the experiment would be determined by the photon flux through space charge effects and the bandwidth of the illumination source, although in the case of soft x-ray lasers the space-charge effect would be dominant. If higher resolution was needed, the photon flux could be reduced by attenuating the soft x-ray laser beam. In that case it might not be possible to carry out single shot experiments but the high repetition rate of the laser (compared to ref. [15, 16] for instance) would allow to measure during reasonable exposure times.

A final remark about the experimental requirements must be done. Typical photoelectron spectroscopy experiments are carried out under extremely careful

vacuum conditions, reaching vacuum levels in the order of 10^{-10} to 10^{-11} Torr. This is done mostly to avoid surface contamination of the sample to be studied, since as it was pointed out before, the photoelectron spectrum provides information about the surface of the sample. However, it is not clear the role played by these contaminants in the damage threshold performance of the thin films. Therefore, it would be ideal to perform the experiments at different vacuum levels, not only the exposure of the sample to the soft x-ray beam, but also the damage threshold experiments.

4.3 Proposed experiment

After analyzing basic experimental requirements and based on the extrapolation of the performance of current soft x-ray lasers to 50 Hz operation, it seems perfectly feasible to carry out photoelectron spectroscopy measurements to study dielectric thin films. These studies could help to improve the performance of multilayer coatings used in high power laser systems.

In this section an experiment to provide a better understanding of damage of thin films by high intensity optical laser pulses is proposed. A few words have to be said about damage threshold of dielectric materials by short laser pulses. It is generally accepted that for laser pulse durations longer than a few tens of ps, damage is produced by heating of conduction-band electrons by the incident

radiation, transfer of this energy to the lattice through inelastic scattering with phonons and subsequent damage through melting, boiling or fracture of the dielectric material. The damage threshold in this case scales with the square root of the pulse duration. For pulses shorter than ~ 10 ps on the other hand, the breakdown threshold mechanism is believed to be quite different: short intense laser pulses produce initial conduction-band electrons by multiphoton ionization. In this picture, collisional heating of the electrons occurs before there is a significant amount of energy transferred to the lattice. The heating and energy diffusion combined with electron impact ionization results in an electron avalanche. According to this model, damage threshold is indicated by a high electron density in the conduction band reaching the critical density for the laser wavelength [21]. Experimental results reported by Stuart *et al* [21] show that in the short pulse limit (400 fs in their experiment) the damage is deterministic, with about 2 % difference in fluence between damage and no damage conditions irradiating the pulse with thousand of pulses in different locations over the sample. On the other hand, they observed that in the long pulse limit (900 ps was the maximum pulse duration in the experiment) there was a 15 % range in the damage threshold depending on position on the sample. This seems to indicate that structural information of the surface (contaminants, defects) is more relevant in the long pulse limit. With these concepts in mind, several experiments are proposed.

The correlation between the presence of contaminants on the film and damage threshold could be studied for long (longer than 20 ps) pulses. In principle this can be done with standard methods of photoelectron spectroscopy such as X-ray photoelectron spectroscopy (XPS) with commercially available devices. However, the soft x-ray laser together with the high power optical laser offer the unique possibility of studying the damage threshold and the photoelectron emission while keeping the sample under the same exact conditions. To be more specific, it would be possible to place the sample under UHV conditions and clean it *in situ* to minimize the presence of contaminants on the surface. Next the photoelectron spectrum could be acquired and finally the sample could be exposed to high intensity optical laser pulses to study the damage threshold. The soft x-ray laser and the optical laser beams could be aligned previously to ensure good spatial overlap on the sample, therefore relating the damage threshold value and the structural information to a particular position on the sample. Scanning over the sample could provide information about the presence of different impurities and contaminants and their relation to the damage threshold value. Also, the experiment could be repeated allowing the presence of more contaminants on the sample (maybe reducing the vacuum level). This could be quantified by following the levels of carbon present on the sample.

As it was stated before, it could be interesting to study the effect of a laser pulse with a fluence right below the damage threshold. In this case the photo-

electron spectrum should be taken before and after the high intensity laser pulse interacts with the sample. The spectra then could be compared looking for differences. Since the damage threshold value changes significantly over different positions on the sample, the experiment should be repeated scanning the sample.

If there should be any detectable structural change on the sample close to the damage value, it would be interesting to carry out time-resolved measurements to see if it is possible to detect at which point during the interaction between the optical pulse and the sample the structure of the material gets significantly affected. In particular it would be interesting to study the pulse width range between 10 to 20 ps approximately, where the transition between different models of damage mechanisms occurs. Ideally this experiment could be done taking single shot measurements with different delays between the optical pulse and the soft x-ray laser pulse, and for a particular delay many sites on the sample should be explored to have a good statistics. But if the resolution gets significantly affected by space charge effects and the results are compromised by the lack of resolution, the experiment could be done integrating in time the results of multiple shots at a fixed delay.

An additional experiment could be done to explore the effects of conditioning of the sample through exposure to radiation. It is often mentioned in the literature that conditioning of the sample increases the damage threshold (see for instance [22]). Therefore it would be interesting to increase gradually the energy per pulse

of the optical laser incident on the sample and take photoelectron spectra before and after each exposure. Then carry out the damage threshold experiment. This could be repeated for a different wavelength of the conditioning radiation, frequency doubling the optical laser for instance.

In summary, the combination of the chirped pulse amplification optical laser system and the soft x-ray laser offers a unique platform for surface characterization of thin films. The envisioned high repetition rate performance of the laser system and the high energy per pulse of the soft x-ray laser should allow to operate in single mode or time integrating many laser shots. The choice of the operating mode would be driven by resolution requirements.

Bibliography

- [1] A. Isoyan, F. Jiang, Y. C. Cheng, F. Cerrina, P. Wachulak, L. Urbanski, J. Rocca, C. Menoni, and M. Marconi. Talbot lithography: Self-imaging of complex structures. *J. Vac. Sci. Technol. B*, 27(6):2931–2937, 2009.
- [2] H. Angus Macleod. *Thin-film optical filters*. Institute of Physics Publishing, 2001.
- [3] Stefan Hüfner. *Photoelectron Spectroscopy: Principles and Applications*. Springer, 2003.
- [4] L. Miaja-Avila, J. Yin, S. Backus, G. Saathoff, M. Aeschlimann, M. M. Murnane, and H. C. Kapteyn. Ultrafast studies of electronic processes at surfaces using the laser-assisted photoelectric effect with long-wavelength dressing light. *Phys. Rev. A*, 79(3):030901, Mar 2009.
- [5] L. Miaja-Avila, C. Lei, M. Aeschlimann, J. L. Gland, M. M. Murnane, H. C. Kapteyn, and G. Saathoff. Laser-assisted photoelectric effect from surfaces. *Phys. Rev. Lett.*, 97(11):113604, Sep 2006.

- [6] G. Saathoff, L. Miaja-Avila, M. Aeschlimann, M. M. Murnane, and H. C. Kapteyn. Laser-assisted photoemission from surfaces. *Phys. Rev. A*, 77(2):022903, Feb 2008.
- [7] Beamson, S. R. Haines, N. Moslemzadeh, P. Tsakirooulos, P. Weightman, and J. F. Watts. High-energy monochromated Cu $K\alpha$ x-ray source for electron spectroscopy of materials: initial results. *Surface and interface analysis*, 36(3):275–279, 2004.
- [8] Prodyut Majumder, Rajesh Katamreddy, and Christos G. Takoudis. Characterization of atomic layer deposited ultrathin HfO_2 film as a diffusion barrier in Cu metalization. In *Mater. Res. Soc. Symp. Proc.*, volume 990, pages B09–03, 2007.
- [9] Kaupo Kukli, Jaan Aarik, Teet Uustare, Jun Lu, Mikko Ritala, Aleks Aidla, Lembit Pung, Anders Hrsta, Markku Leskel, Arvo Kikas, and Vino Sammelselg. Engineering structure and properties of hafnium oxide films by atomic layer deposition temperature. *Thin Solid Films*, 479(1-2):1 – 11, 2005.
- [10] J. W. Keister, J. E. Rowe, J. J. Kolodziej, H. Niimi, H. S. Tao, T. E. Madey, and G. Lucovsky. Structure of ultrathin $\text{SiO}_2/\text{Si}(111)$ interfaces studied by photoelectron spectroscopy. *J. Vac. Sci. Tech. A*, 17(4):1250–1257, Jul/Aug 1999.

- [11] G. E. McGuire, G. K. Schweitzer, and T. A. Carlson. Study of core electron binding energies in some group IIIa, Vb, and VIb compounds. *Inorganic Chemistry*, 12(10):2450–2453, 1973.
- [12] D. A. Shirley, R. L. Martin, S. P. Kowalczyk, F. R. McFeely, and L. Ley. Core-electron binding energies of the first thirty elements. *Phys. Rev. B*, 15(2):544–552, Jan 1977.
- [13] David Attwood. *Soft x-rays and extreme ultraviolet radiation*. Cambridge University Press, 2000.
- [14] J. D. Koralek, J. F. Douglas, N. C. Plumb, J. D. Griffith, S. T. Cundiff, H. C. Kapteyn, M. M. Murnane, and D. S. Dessau. Experimental setup for low-energy laser-based angle resolved photoemission spectroscopy. *Rev. of Sci. Inst*, 78:053905, 2007.
- [15] A. J. Nelson, J. Dunn, T. van Buuren, and J. Hunter. X-ray laser-induced photoelectron spectroscopy for single-state measurements. *Appl. Phys. Lett.*, 85(25):6290–6290, 2004.
- [16] A. J. Nelson, J. Dunn, J. Hunter, and K. Widmann. Time-resolved x-ray laser induced photoelectron spectroscopy of isochoric heated copper. *Appl. Phys. Lett.*, 87:154102, 2005.

- [17] X. J. Zhou, B. Wannberg, W. L. Yang, V. Brouet, Z. Sun, J. F. Douglas, D. Dessau, Z. Hussain, and Z. X. Shen. Space charge effect and mirror charge effect in photoemission spectroscopy. *J. of Electron Spectroscopy and Related Phenomena*, 142:27–38, 2005.
- [18] S. Hellmann, K. Rossnagel, M. Marczynski-Bühlow, and L. Kipp. Vacuum space-charge effects in solid-state photoemission. *Phys. Rev. B*, 79(3):035402, Jan 2009.
- [19] Yoichi Uehara, Tadamasa Ushiroku, Sukekatsu Ushioda, and Yoshitada Murata. High resolution time-of-flight electron spectrometer. *Japanese Journal of Applied Physics*, 29(Part 1, No. 12):2858–2863, 1990.
- [20] Andrea Damascelli. Probing the electronic structure of complex systems by ARPES. *Physica Scripta.*, T109:61–74, 2004.
- [21] B. C. Stuart, M. D. Feit, S. Herman, A. M. Rubenchik, B. W. Shore, and M. D. Perry. Nanosecond-to-femtosecond laser-induced breakdown in dielectrics. *Phys. Rev. B*, 53(4):1749–1761, Jan 1996.
- [22] Ming Zhou, Jianda Shao, Zhengxiu Fan, Yuan-An Zhao, and Dawei Li. Effect of multiple wavelengths combination on laser-induced damage in multilayer mirrors. *Opt. Express*, 17(22):20313–20320, 2009.

[23] Very insightful discussions and comments from the following people were key for the realization of this chapter: Prof. J. Rocca, Prof. Mario Marconi, Prof. Carmen Menoni, Dr. D. Patel and Dr. Patrick McCurdy.

Chapter 5

SUMMARY

The field of laser-driven collisional soft x-ray lasers has evolved from facility-type devices operating at a few shots per day to table-top laser systems capable of operating at several shots per second and enabling multiple applications. In this work, the historical evolution of the field was presented pointing out the concepts and developments that signified a key contribution to the field. It was also stated that currently the limitation towards more compact devices with increased average power is set by thermal effects intrinsic to flash lamp pumping of the amplifiers in the driver laser. The realization of high average power in a more compact footprint is crucial to improve applications such as nano-scale imaging or nano-patterning. It is also expected that an improved source will enable yet unforeseen applications.

The aim of the project described by this dissertation was to develop a novel chirped pulse amplification laser system to pump soft x-ray lasers. The specifications taken into account during the design phase of the project were guided towards overcoming the limitations of current table-top systems. With this in mind, an all diode-pumped chirped pulse amplification system was developed, in which the laser material in the amplification stages is cryogenically cooled Yb:YAG. The advantages of diode pumping small quantum defect materials such as Yb:YAG were analyzed and in addition it was pointed out that operating this material at cryogenic temperatures presents several advantages over room temperature operation for the development of high repetition rate, high energy per pulse laser systems.

A general description of the chirped pulse amplification system and soft x-ray laser developed was presented. The system is very compact when compared to previous table-top soft x-ray laser systems. The chirped pulse amplification system with the exception of the pulse compressor fits in a standard optical table of $5 \times 12 \text{ ft}^2$. The system presents other improvements in the design over previous table-top soft x-ray lasers, such as the two-stretcher configuration that allows to generate a set of collinear pulses, ensuring the spatial overlap between pre-pulses and the plasma heating pulse.

The results presented in this dissertation represent the first demonstration of a soft x-ray laser driven by an all diode-pumped chirped pulse amplification laser system. Although the increased repetition rate performance was not achieved yet, this novel laser system has the potential to operate at unsurpassed repetition rates. When the system is further developed to reach its full potential many applications will benefit from its improved output characteristics. In particular, an experiment was proposed to study the damage threshold performance of thin film dielectric coatings, in which the soft x-ray laser is the source for photoelectron spectroscopy experiments.

The all diode-pumped chirped pulse amplification system by itself is also a novelty in the field of solid state lasers. Currently this laser system provides, to the best of our knowledge, the highest energy per pulse for sub-10 ps pulses from an all diode-pumped system.

In summary, we have demonstrated the first soft x-ray laser driven by a solid-state laser system entirely pumped by laser diodes. Lasing in the 18.9 nm line of Ni-like molybdenum was observed using a compact Yb:YAG system that generates compressed pulses of 8.5 ps duration with up to 1 J energy, the highest energy per pulse for sub-10 ps pulses from an all diode-pumped chirped pulse amplification laser system. Future work can be expected to lead to the development of very compact soft x-ray lasers that will operate at unsurpassed repetition rates.